Title
Galaxies and Dark Matter in Groups

Author
George, Matthew Richard

Publication Date
2014

Peer reviewed|Thesis/dissertation

Galaxies and Dark Matter in Groups

By

Matthew Richard George

A dissertation submitted in partial satisfaction of the

requirements for the degree of

Doctor of Philosophy

in

Astrophysics

in the

Graduate Division

of the

University of California, Berkeley

Committee in charge:
David Schlegel, Co-chair
Uros Seljak, Co-chair
Marc Davis
Saul Perlmutter

Fall 2014

Galaxies and Dark Matter in Groups

Abstract

Galaxies and Dark Matter in Groups

by

Matthew Richard George

Doctor of Philosophy in Astrophysics

University of California, Berkeley

David Schlegel, Co-chair
Uros Seljak, Co-chair

This thesis presents a systematic study of the relationships between galaxy properties and their environments. Multi-wavelength imaging and spectroscopic data are used to construct a large sample of galaxy groups spanning nearly half the age of the Universe. Weak gravitational lensing measurements enable a census of baryonic and dark matter in these groups, and in particular, identification of halo centers. With empirically determined centers of mass, trends in galaxy colors and morphologies with groupcentric distance are studied to test models of galaxy evolution.

Contents

Acknowledgments

Marc Davis once told me that *"a thesis is not supposed to be your best work; it's just practice."* I hope he's right.

Still, I wish to thank a small portion of the many people who have shaped my progress to this point. I am thankful to have had a wonderful array of research collaborators. Alexie Leauthaud has been an amazing mentor, guiding me through my early projects and sharing her expertise. Kevin Bundy, Jeremy Tinker, and Alexis Finoguenov have generously offered their hours and insights.

Thanks to my advisor, David Schlegel, for his guidance and enthusiasm, for introducing me to endurance cycling, and for instilling an ethic that it is better to ask forgiveness than permission. Thanks to Uros Seljak for keeping me on my toes and exposing me to shellfish. Thanks to the other members of my committee, Chung-Pei Ma, Marc Davis, and Saul Perlmutter for sharing their advice, experience, and tough questions.

Thanks especially to Andrew Wetzel and Eric Huff for organizing a cosmology discussion group and for many thoughtful conversations. Thanks to the many other grad students and postdocs who have helped with kicking around ideas, sharing their wisdom, and getting outdoors, particularly Jessica Kirkpatrick, Jon Blazek, Nicholas McConnell, Nic Ross, Beth Reid, and Ami Choi. Thanks to all the denizens of Del Mar, and specifically Peter Williams for introducing me to the house, to git, and to his ucastrothesis LaTeX template. Thanks also to Katie Aspell for support and patience while finishing up this year.

There are some other groups of people I would like to acknowledge that played important roles in my time at Berkeley. First, the creators and maintainers of the East Bay Regional Park District, where I have spent many hours contemplating (and sometimes escaping) the contents of this document. Another large and largely unknown group to thank are the developers of open source software tools used in my research. A third important community to which I owe gratitude are the data collectors and survey architects behind the COSMOS collaboration and the Sloan Digital Sky Survey.

Finally, my deepest thanks to my family for all their support and encouragement that helped me get here.

Chapter 1

Introduction

A multitude of observations of our Universe, from the anisotropies of the cosmic microwave background to the clustering of galaxies and the expansion history derived from supernovae, can be described by a simple yet befuddling cosmological model. In this model the familiar baryonic component of the Universe, which can be detected through electromagnetic interactions, is dwarfed by two dark constituents that dominate the energy density. Dark matter is effectively collisionless and nonrelativistic, seeding structure growth and hosting galaxies in deep gravitational potentials called halos. Perturbations in the density of baryons and dark matter, initialized after a period of rapid inflation, eventually collapsed under gravitational instability to form these galaxies and halos which merge and grow hierarchically. Dark energy exerts a uniform negative pressure, accelerating expansion and suppressing structure growth at late times. The existence of these dark components implies that extensions are necessary to our standard models of particle physics, gravity, or both.

Testing the validity of this cosmological model and constraining its parameters is the focus of much observational and theoretical effort. What is dark matter and how is it distributed in space? Does it couple with baryons or self-interact in detectable ways? Does the dark energy density vary with space or time? Does general relativity accurately describe gravity on large and small scales? These are the questions we ultimately aim to address to further our understanding of the dark side of our Universe.

On large scales, the distribution of matter is accurately described by the linear evolution of density perturbations from inflation under gravitational instability. On smaller scales, density fluctuations become nonlinear and collapse into halos. Halos are densest near their centers and may host a central galaxy, and more massive halos can host additional satellite galaxies that sample the dark matter density as a stochastic tracer. Numerical simulations reveal a wide variety of halo shapes and density profiles for these halos, but on average they are spherical and can be described with a simple model the depends on their mass and concentration. A halo model with these assumptions can remarkably reproduce many observations of nonlinear structure.

There is still much to be learned from constraining the parameters of this cosmological model and determining where the simplifying description of halos breaks down. The growth of structure can be measured from the distribution of halo masses and its evolution over time. This offers a test of dark energy that is complementary to measurements of the expansion history. The detailed density profiles in halos and abundance of substructure are sensitive to the mass and interaction cross section of dark matter, which ultimately tell us about the physics of its formation.

Complications arise when constraining these quantities from observations. Galaxy surveys have served as the workhorse for large-scale structure measurements. Wide area imaging taken at Lick Observatory in the 1950s provided the first systematic probe of the large-scale spatial distribution of galaxies. Later the CfA Redshift Survey added a third dimension to such maps, and opened the field for a proliferation of modern experiments including the Sloan Digital Sky Survey and DEEP2, pushing boundaries in volume and depth of coverage. Multi-wavelength imaging and spectroscopic surveys such as COSMOS have supplemented these optical studies with observations from radio to X-ray bands, providing new insight into the interplay of stars and gas with dark matter.

Dark matter halo masses and density profiles can only be measured from these data indirectly. Galaxies are visible tracers of the dark matter density field, but the details of how galaxies populate dark matter halos can be complicated. From two- or three-dimensional maps, groups and clusters of galaxies can be identified based on their proximity. Many estimators have been employed to extract halo masses from observables. Galaxy counts, luminosities, and stellar masses can be derived relatively inexpensively, while it is generally more costly to measure galaxy dynamics or the temperature and luminosity profiles of the hot gas in massive halos. Gravitational lensing offers another probe of the projected matter distribution that is in principle independent of the baryonic tracers used in other estimators. In general, these methods have been shown to correlate with one another and produce a coherent picture of halo masses and density profiles. But for precision cosmology, it is essential to probe these small nonlinear scales and to improve our understanding of the biases in techniques for extracting the matter distribution from observations.

The mission to understand how galaxies trace dark matter plays in important role in cosmological studies, but also raises interesting questions in its own right. Galaxy properties are broadly bimodal, with a population of more massive and luminous red galaxies that tend to have older stellar populations, more spheroidal morphologies, and concentrated light profiles than a distinct population of younger, blue star-forming galaxies. Why do galaxies look the way they do, and what processes led to the menagerie we observe?

This thesis presents a systematic study of the relationships between galaxy properties and their environment, to both address the basic questions about galaxy evolution and to support further cosmological study with a better understanding of how galaxies inhabit dark matter halos. I have connected measurements of X-ray emission and weak lensing for a large sample of galaxy groups spanning nearly half the age of the Universe (George et al. 2011). This sample consists of the most massive halos in the largest contiguous area mapped by the Hubble Space Telescope, and and includes new optical spectroscopy of group members. This group sample has been exploited with the high-resolution imaging and multi-wavelength photometry from the COSMOS survey to constrain dark matter halo properties of this group sample with weak lensing (Leauthaud et al. 2010; George et al. 2012; Schmidt et al. 2012; Ford et al. 2012; Taylor et al. 2012) and also for studying the masses, colors, and morphologies of galaxies residing in these halos (George et al. 2011, 2013; Leauthaud et al. 2012b). Miscentering is a dominant systematic uncertainty in measuring halo masses (Rozo et al. 2011), so identifying correct centers and modeling offsets is crucial. To address this issue, I developed a new approach to find halo centers based on the stacked weak lensing signal (George et al. 2012). The models I developed can readily be extended to measure substructure around satellites and the stellar mass to light ratio in galaxies with lensing and dynamical measurements.

The properties of galaxies are linked to their environment, and quantifying these correlations is important to understand the coevolution of baryonic and dark matter. While it has long been known that dense environments host galaxies with greater masses, lower star-formation rates, and more bulge-dominated morphologies (see Blanton & Moustakas 2009, for a review), the processes that produce these correlations remain unclear, in part due to the many interrelated variables at play. Large data sets from recent and upcoming surveys are finally enabling us to isolate trends in specific properties with others fixed. This study of group member galaxies quantifies the separate dependences of galaxy color and morphology on group-centric distance (at effectively fixed stellar mass, halo mass, and redshift), which constrains models of galaxy evolution involving gas stripping, feedback, and mergers (George et al. 2013).

The work in this thesis has been published in three separate papers, each of which is translated into a chapter here. Chapter 2 (George et al. 2011) describes the construction of the group catalog and detailed tests of group membership assignment using simulations. Chapter 3 (George et al. 2012) presents a weak lensing study to test different tracers of halo centers and their impact on halo mass estimates. Chapter 4 (George et al. 2013) employs those halo centers to measure the dependence of galaxy properties on groupcentric distance, illustrating how star-formation rates and structural parameters in galaxies are related to the dark matter halos they inhabit.

Chapter 2

Robust Membership Assignment and the Impact of Group Environments on Quenching

Understanding the mechanisms that lead dense environments to host galaxies with redder colors, more spheroidal morphologies, and lower star formation rates than field populations remains an important problem. As most candidate processes ultimately depend on host halo mass, accurate characterizations of the local environment, ideally tied to halo mass estimates and spanning a range in halo mass and redshift are needed. In this work, we present and test a rigorous, probabalistic method for assigning galaxies to groups based on precise photometric redshifts and X-ray selected groups drawn from the COSMOS field. The groups have masses in the range $10^{13} \lesssim M_{200c}/M_{\odot} \lesssim 10^{14}$ and span redshifts $0 < z < 1$. We characterize our selection algorithm via tests on spectroscopic subsamples, including new data obtained at the VLT, and by applying our method to detailed mock catalogs. We find that our group member galaxy sample has a purity of 84% and completeness of 92% within $0.5R_{200c}$. We measure the impact of uncertainties in redshifts and group centering on the quality of the member selection with simulations based on current data as well as future imaging and spectroscopic surveys. As a first application of our new group member catalog which will be made publicly available, we show that member galaxies exhibit a higher quenched fraction compared to the field at fixed stellar mass out to $z \sim 1$, indicating a significant relationship between star formation and environment at group scales. We also address the suggestion that dusty star forming galaxies in such groups may impact the high-ℓ power spectrum of the cosmic microwave background and find that such a population cannot explain the low power seen in recent SZ measurements.

2.1 Introduction

Galaxies in dense cluster regions have long been known to have different characteristics than counterparts in the field, with redder colors, a greater tendency for spheroidal morphologies, and suppressed star formation rates. Dense clusters are also the sites of the most massive and luminous galaxies. Much effort has been made to find the redshift, halo mass, and cluster-centric distance at which these distinctions between galaxy populations are imprinted and the process by which these transformations occur (e.g., Oemler 1974; Dressler 1980; Butcher & Oemler 1984; Dressler et al. 1997; Poggianti et al. 1999; Lewis et al. 2002; Goto et al. 2003; Balogh et al. 2004; De Propris et al. 2004; Kauffmann et al. 2004; Lin et al. 2004; Blanton et al. 2005; Cucciati et al. 2006; Cooper et al. 2006; Weinmann et al. 2006; Capak et al. 2007a; Gerke et al. 2007; Blanton & Moustakas 2009; Hansen et al. 2009; Mei et al. 2009; Feruglio et al. 2010). While massive clusters present clear examples of galaxy transformations due to gas stripping, merger activity, and tidal disruption (e.g., Kenney et al. 1995; Gavazzi et al. 2001; Cortese et al. 2007), the extent to which these processes affect the majority of galaxies which live in less dense environments is uncertain. Extending cluster samples to groups with lower halo masses and higher redshifts is challenging because it requires significant observational expenditures and careful analysis to isolate such environments from the field.

Recent analyses at low redshift have confirmed the existence of an environmental dependence of galactic structure and colors across a range of environments (e.g., Kauffmann et al. 2004; Baldry et al. 2006; Bamford et al. 2009). The corresponding picture at $z \sim 1$ has been less clear. With pointed observations around high-redshift galaxy clusters, several studies have found significant trends in morphology, color, and star-formation rate with local galaxy density (e.g., Postman et al. 2005; Smith et al. 2005b; Tanaka et al. 2005; Poggianti et al. 2008). However, some find that the relations disappear in stellar mass-selected samples, arguing that environmental trends are due to differences in the stellar mass distribution between environments rather than physical processes acting in dense regions (e.g., Poggianti et al. 2008).

In field surveys reaching $z \sim 1$, results from the VIRMOS-VLT Deep Survey (VVDS; Scodeggio et al. 2009) and zCOSMOS (Tasca et al. 2009; Cucciati et al. 2010; Iovino et al. 2010; Kovač et al. 2010) show little or no environmental influence on morphology and color especially at high stellar masses ($\log(M_\star/M_\odot) \gtrsim 10.7$), while results from DEEP2 (Cooper et al. 2010) and others from zCOSMOS (Peng et al. 2010) show a clear relationship between color and environment. These papers generally find weakening environmental trends with increasing redshift, but differ in the redshift at which the trends disappear. Cooper et al. (2007) and Cooper et al. (2010) discuss the discrepancies in environmental trends seen in high-redshift field surveys and suggest that the non-detection by some studies could be due to the use of less confident spectroscopic redshifts and lower sampling rates, as well as increased difficulty with determining environmental densities using optical spectroscopy at high redshift, while Peng et al. (2010) attributes the differences to the definitions used to characterize environments.

The aim of this work is to define a clean sample of galaxies in dense group environments out to redshift $z = 1$ to address these issues. We study groups from the COSMOS survey that have been identified as sources of extended X-ray emission (Finoguenov et al. 2007, and in prep.), which is a strong indication that they are virialized structures and not chance associations of galaxies. The groups have halo masses in the range $10^{13} \lesssim M_{200c}/M_{\odot} \lesssim 10^{14}$ as determined by weak lensing (Leauthaud et al. 2010). In Chapter 3 (George et al. 2012). We select member galaxies based on photometric redshifts derived from extensive multi-wavelength imaging, which provides a much greater sampling density than existing spectroscopic surveys. Using a spectroscopic subsample and mock catalogs, we carefully evaluate our member selection for potential biases or contamination, and account for photometric redshift uncertainties. This robust sample of group members can be used to address unsettled questions about the link between galaxies and their environments.

A key challenge is to disentangle the intrinsic and extrinsic factors that may play a role in shaping galaxy properties. For instance, galaxies in dense regions have a higher characteristic stellar mass than in less dense environments (e.g., Baldry et al. 2006), so a morphology-mass relation could be conflated with a morphology-density relation. Since stellar mass plays an important role in determining galaxy properties, and mass-to-light ratios are strongly affected by star formation activity, recent environmental studies have stressed the use of stellar mass-selected samples rather than luminosity-selected samples to make a fair comparison across environments (e.g., van der Wel et al. 2007; Scodeggio et al. 2009; Cooper et al. 2010).

In addition to controlling for intrinsic galaxy properties in these studies, defining and measuring the "environment" presents another problem. The distance to the Nth nearest neighbor or the mean density of galaxies inside a fixed radius are commonly used as environmental indicators (e.g., Dressler 1980). Kauffmann et al. (2004) show that galaxy properties correlate most tightly with local density on scales below ~ 1 Mpc and are uncorrelated with the density on larger scales once the small-scale density is fixed. Several studies have shown evidence that galaxy properties correlate most tightly with density within their halo, and have emphasized that the aperture used for comparing equivalent regions must scale with halo mass to avoid confusion between local and global densities (Hansen et al. 2005; Weinmann et al. 2006; Blanton & Berlind 2007; Haas et al. 2011). Instead of using the galaxy density field to define environment, one can define a catalog of galaxy groups and clusters and study their properties as a function of halo mass and group-centric distance. We use the term "group" to denote a set of galaxies with a common dark matter halo and to emphasize the low mass range studied, making no formal distinction between groups and clusters.

Catalogs of galaxy groups have been constructed from both optical surveys identifying galaxy overdensities and X-ray surveys detecting the hot gas trapped by deep gravitational potentials. Optical catalogs often employ matched filters (e.g., Postman et al. 1996) and tesselations (e.g., Marinoni et al. 2002; Gerke et al. 2005) to isolate groups from the background field, and red sequence methods have proven efficient at identifying groups over large volumes (e.g., Gladders & Yee 2005; Koester et al. 2007a). These catalogs typically assign the brightest member galaxy as the center of each group, and use the richness determined by the number of members as a proxy for the total mass. X-ray detections can reduce the likelihood of projection effects, improve mass estimates, help with the determination of group centers, and shed light on the interplay between the hot gas and stellar content of groups (e.g., Mulchaey et al. 2003; Lin et al. 2004; Finoguenov et al. 2007; Sun et al. 2009).

Our understanding of group properties has benefited from small, well-studied samples at low redshift (e.g., Mulchaey & Zabludoff 1998; Zabludoff & Mulchaey 1998; Tran et al. 2001; Sun et al. 2009) along with larger statistical samples taken over wide areas or to high redshifts (e.g., Eke et al. 2004; Gerke et al. 2005; Gladders & Yee 2005; Miller et al. 2005; Yang et al. 2005; Berlind et al. 2006; Hansen et al. 2009). These studies have established many similarities between groups and more massive clusters, including their extended dark matter halos and elevated fractions of quenched early type galaxies relative to the field. Groups show some differences from clusters including gas mass fractions that are typically lower in less massive systems, and the differences between physical processes acting on galaxies in groups and those in clusters are still being explored. Recent and ongoing surveys are pushing to greater sample sizes and higher redshifts with multi-wavelength observations and spectroscopic campaigns (e.g., Osmond & Ponman 2004; Driver et al. 2009; Milkeraitis et al. 2010; Adami et al. 2010). Several large imaging surveys in development plan to study the growth of structure without significant spectroscopic observations initially (Dark Energy Survey[1], Hyper Suprime-Cam[2], Large Synoptic Survey Telescope[3], EUCLID[4]), so photometric redshifts will be important for identifying member galaxies using techniques such as those outlined here.

We study groups in the COSMOS field where a unique data set has been compiled for studying the interplay between galaxies, intragroup gas, and dark matter in galaxy groups out to $z \sim 1$. The COSMOS survey has obtained X-ray observations for group detections, deep imaging data spanning ultraviolet (UV), optical, and infrared (IR) wavelengths for precise photometric redshifts and stellar masses, extensive spectroscopic coverage, and high resolution imaging from the *Hubble Space Telescope* (HST) for measuring morphologies and weak lensing. Group catalogs have been constructed in this field from X-ray data (Finoguenov et al. 2007, and in prep.), zCOSMOS spectroscopy (Knobel et al. 2009), photometric redshifts (Gillis & Hudson 2011), CFHTLS-Deep photometry (Olsen et al. 2007; Grove et al. 2009), and with a combination of weak lensing and matched filters (Bellagamba et al. 2011). Additionally, Scoville et al. (2007) studied large-scale structures in this field using photometric redshifts, and Kovač et al. (2010) measured the galaxy density field using zCOSMOS redshifts to probe a large dynamic range of environments. Here we focus on the X-ray selected group catalog to ensure a pure sample of virialized structures whose masses have been characterized with weak lensing (Leauthaud et al. 2010). Giodini et al. (2009) have studied the stellar mass content of these X-ray groups; we expand upon their work with a thorough characterization of a new member selection algorithm and develop a group member catalog for a variety of applications.

[1]http://www.darkenergysurvey.org
[2]http://sumire.ipmu.jp/en
[3]http://www.lsst.org
[4]http://sci.esa.int/euclid

The data used in making our group catalog are described in § 2.2. In § 2.3, we present the sample selection and sensitivity limits, along with tests of the quality of the photometric redshifts constructed from the imaging data. Our selection algorithm for the member catalog is described in § 2.4, where we associate member galaxies with groups based on their proximity to the X-ray center and their photometric redshifts. In § 2.5, we characterize the reliability of our selection with mock catalogs from simulations and by comparing our photometric redshift selection to the subsample of sources with spectroscopic redshifts. We make the catalog of group membership assignments and galaxy properties publicly available, describing the format and release in § 2.6. We discuss in § 2.7 some of our initial findings from the catalog, including the influence of the group environment on galaxy colors out to $z \sim 1$. We find evidence of suppressed star formation in galaxies in group environments over the entire redshift range studied, and briefly discuss how the low incidence of star forming galaxies in groups cannot play a significant role in explaining recent observations of a deficit of power from the Sunyaev-Zel'dovich effect (SZ; Sunyaev & Zeldovich 1972) in the angular spectrum of the cosmic microwave background (CMB; e.g., Lueker et al. 2010; Fowler et al. 2010).

We adopt a WMAP5 ΛCDM cosmology to determine distances and halo masses with $\Omega_{\rm m} = 0.258$, $\Omega_\Lambda = 0.742$, $H_0 = 72$ km s^{-1} Mpc^{-1} (Dunkley et al. 2009), the same values used by Leauthaud et al. (2010) to calibrate the masses of this group sample. Distances are expressed in physical units of Mpc, magnitudes are given on the AB system, X-ray luminosities are expressed in the rest-frame 0.1-2.4 keV band, and logarithmic quantities use base 10. Group masses are estimated from their X-ray luminosity using the $L_X - M$ relation derived in Leauthaud et al. (2010) and concentrations are then derived from the mass-concentration relation of Zhao et al. (2009) assuming an NFW density profile (Navarro, Frenk, & White 1996). We estimate the virial radius of groups as $R_{\rm 200c}$, the radius within which the mean density is 200 times the critical density of the Universe at the redshift of the group, $\rho_{\rm c}(z_{\rm G})$, and use the corresponding halo masses defined as $M_{\rm 200c} \equiv (200\rho_{\rm c}(z_{\rm G}))(4\pi/3){R_{\rm 200c}}^3$. We also make use of the NFW scale radius, defined as $R_{\rm s} = R_{\rm 200c}/c_{\rm 200c}$, where $c_{\rm 200c}$ is the concentration parameter.

2.2 COSMOS Data

The COSMOS field has been observed in a broad range of wavelengths, with imaging data from X-ray to radio and a large spectroscopic follow-up program (zCOSMOS) with the Very Large Telescope (VLT) (Scoville et al. 2007; Koekemoer et al. 2007; Lilly et al. 2007). We have added to the spectroscopic sample in groups with a recent campaign using the Focal Reducer and low dispersion Spectrograph 2 (FORS2) at the VLT (Program ID 084.B-0523; PI: Mei). X-ray imaging has been taken with the *XMM-Newton* (1.5 Ms covering 2.13 deg^2; Hasinger et al. 2007; Cappelluti et al. 2009) and *Chandra* observatories (1.8 Ms covering 0.9 deg^2; Elvis et al. 2009). Imaging obtained through the F814W filter of the Wide Field Channel (WFC) of the Advanced Camera for Surveys (ACS) on HST adds accurate shape measurements for morphologies and weak lensing (Scarlata et al. 2007; Leauthaud et al. 2007). Observations of over thirty photometric bands covering the ultraviolet, optical, and infrared ranges have enabled the determination of precise photometric redshifts (Capak et al. 2007b; Ilbert et al. 2009), with typical redshift uncertainty $\sigma_{\mathcal{P}} \lesssim 0.01$ for galaxies with F814W < 22.5, and $\sigma_{\mathcal{P}} = 0.03$ for F814W=24, at $z < 1.2$ (see §§ 2.2.3 and 2.3.2 for details and tests of the photometric redshifts).

2.2.1 X-ray Catalog

The entire COSMOS region has been mapped through 54 overlapping *XMM-Newton* pointings and additional *Chandra* observations covering the central region (0.9 deg^2) with higher spatial resolution. A mosaic combining these two data sets has been used to find and measure the fluxes of groups using a wavelet transform method described in Vikhlinin et al. (1998). The data reduction process including the combination of X-ray data sets and identification of optical counterparts follows that of Finoguenov et al. (2009, 2010). An initial group catalog from the COSMOS field is presented in Finoguenov et al. (2007).

Briefly, extended objects are detected in the mosaic when the sum of the flux on scales of 32″ and 64″ is greater than the flux on small scales by a given threshold. Detections on smaller scales tend to be contaminated by point sources, which are cleaned from *XMM* and *Chandra* data separately to allow for variability. The flux is calculated using a scaling relation that incorporates a β-model fit to the surface brightness within 32″, resulting in a 4σ detection limit of the group sample of 1.0×10^{-15} erg cm^{-2} s^{-1} over 96% of the ACS field. Once extended X-ray sources are detected, a red sequence finder is employed on galaxies with a projected distance less than 0.5 Mpc from the centers to identify an optical counterpart and determine the redshift of the group, which is then refined with spectroscopic redshifts when available. The red sequence finder only requires an overdensity of red galaxies and not a deficiency of blue galaxies, meaning that it does not specifically require an enhanced red fraction to identify groups.

A quality flag (hereafter XFLAG) is assigned to the reliability of the optical counterpart, with flags 1 and 2 indicating a secure association, and higher flags indicating potential problems due to projections with other sources or bad photometry due to bright stars in the foreground. We run our membership algorithm on all detections in the catalog with $z_{\mathrm{G}} < 1$ but in later analyses limit the sample to groups with XFLAG $= 1$ and 2, which have reliable spectroscopically confirmed optical counterparts. The difference in these two flags reflects the uncertainty in the X-ray position; for XFLAG $= 2$ the uncertainty in each coordinate is assumed equal to the wavelet scale of 32″, and for XFLAG $= 1$ sources, which have more certain centers, the uncertainty is 32″ divided by the significance of the flux measurement. The mean uncertainty in right ascension and declination for sources with flags 1 and 2 is 23″ (120 kpc at $z = 0.4$ and 170 kpc at $z = 0.8$ for our adopted cosmology).

The main changes from the catalog described in Finoguenov et al. (2007) are the detection of fainter groups thanks to deeper *XMM* coverage, a more conservative point-source removal procedure, increased redshift accuracy due to the availability of more spectroscopic data and improved photometric redshifts, and some changes in quality flags after visual inspection of optical counterparts. In total, the catalog contains 211 extended X-ray sources over 1.64 deg^2, spanning the redshift range $0 < z < 1$ and with a rest-frame 0.1–2.4 keV luminosity range of $41.3 < \log(L_X/\mathrm{erg\ s}^{-1}) < 44.1$, and 165 of these groups and clusters have secure optical counterparts with XFLAG = 1 or 2. X-ray detections without clear optical counterparts are likely a mix of unresolved active galactic nuclei (AGN), projections of multiple systems, and background fluctuations.

2.2.2 Spectroscopic Data

The COSMOS field has been targeted by a number of spectroscopic campaigns. We use spectra from the zCOSMOS "20K sample" (Lilly et al., in prep.) which targeted galaxies in the ACS area to a magnitude limit of $i^+ = 22.5$, along with other spectroscopic data sets from Keck, MMT, SDSS, and VLT (Prescott et al. 2006; Capak et al. 2010). We include a new sample from our program with FORS2/VLT (see § 2.2.2). Each redshift has an associated confidence flag; we use only those of class 3 or 4 meaning that the redshift is secure or very secure. In repeat observations, zCOSMOS targets with these confidence classes have a verification rate of > 99% (Lilly et al. 2007). For galaxies in the ACS field with F814W < 24.2 and any redshift passing this quality cut, the spectroscopic sample has 529 galaxies from FORS2, 11619 from zCOSMOS, and 1527 from other sources. These spectra are distributed throughout the redshift range studied, with 1931 at $0.05 < z \leq 0.25$, 4257 at $0.25 < z \leq 0.50$, 4184 at $0.50 < z \leq 0.75$, and 1980 at $0.75 < z \leq 1.00$.

A spectroscopically-selected group catalog has been constructed by Knobel et al. (2009). We defer a detailed comparison between the galaxy content of spectroscopically-selected groups and X-ray selected groups to future work (Finoguenov et al., in prep.). Kovač et al. (2010) showed that there is good general correspondence between the overdense regions in the galaxy density field, the spectroscopically-selected groups with $N_{\mathrm{mem}} \geq 4$, and the X-ray detected groups.

Our primary use of the spectra is to obtain precise group redshifts and to verify the accuracy of photometric redshifts, which are critical for both the membership selection and the weak lensing analysis. Roughly 20% of group members have spectroscopic redshifts in addition to the photometric redshifts used for member selection.

FORS2 Spectra

We have recently obtained additional spectra of galaxies in the COSMOS field with the FORS2 spectrograph at the VLT. Targets were selected for a number of scientific goals including velocity dispersion measurements of massive central galaxies and a comparison sample of field ellipticals, a study of merger rates within groups based on the abundance of close pairs, and refined redshift determinations for group members. Data were taken on four clear nights with excellent conditions and 0.8″ typical seeing from 2010 February 14-18. The FORS2 instrument was used in MXU mode with the 600RI grism and GG435 order separation filter, providing a wavelength range of roughly $4500 - 9000$Å. There were 27 masks each observed in 4 exposures of 650 seconds. Each mask had roughly 50 slits of width $0.6''$ for bright targets and $1''$ for fainter ones, and a typical slit length of $8''$.

These data have been reduced using the standard ESOREX reduction pipeline[5]. In short, for each mask and detector we performed bias subtraction and overscan removal, determined a wavelength solution from He, HgCd, Ar, and Ne arc lamps, and found slit extraction regions using a pattern recognition algorithm on the arc and flat lamp exposures. Science exposures were bias subtracted and flat fielded before a median combination. The flat fields were first normalized by dividing out a smooth component calculated using a 10×10 pixel median filter to account for the intrinsic shape of the flat lamp spectrum. A local sky subtraction was performed on each CCD column prior to rectification, then cosmic rays were removed and object spectra were optimally extracted.

For the extracted objects, we measured redshifts with a modified version of the ZSPEC software used for the DEEP2 survey (Cooper et al., in prep.). Each one-dimensional spectrum was fit by a linear combination of galaxy eigenspectra and also compared with stellar and quasar templates over a range of redshifts to find possible redshift values. Spectral features important for fitting in this range of wavelengths and redshifts include [O II], CaK, CaH, G-Band, Hβ, [O III], Mgb, and NaD. Each spectrum was visually inspected by at least two co-authors alongside the two-dimensional spectral image to choose the best redshift and assign a quality flag according to the zCOSMOS system (Lilly et al. 2007). In cases where the first two inspectors disagreed on the redshift or quality flag, a third person viewed the spectrum independently to reconcile differences. We include only those objects with a secure redshift (quality flag = 3,4) in our sample, which amounts to 529 galaxies. Our redshift success rate will improve with continuing reduction efforts to handle cases where slits were tilted to cover close pairs or to measure velocity dispersions along the major axis of a galaxy. There are 8 objects in this sample that have been observed by SDSS, with a median and scatter between redshift measurements of 16 and 43km s^{-1}, respectively. For 126 objects observed by both FORS2 and zCOSMOS, the scatter in redshifts is 160 km s^{-1} after removing 2 outliers with $|\Delta z| > 0.002$. We have detected a median offset of ~ 100 km s^{-1} between zCOSMOS redshifts and those measured by FORS2 and SDSS which is still under investigation, but since the magnitude of this offset is a factor of 3 smaller than the typical group velocity dispersion and several times smaller than photometric redshift errors it should not impact our results.

2.2.3 Photometric Redshifts

Despite the extensive spectroscopic data available, coverage of group members is incomplete. We instead use photometric redshifts (hereafter photo-zs) to determine distances to galaxies. Ilbert et al. (2009) constructed spectral energy distributions (SEDs) from over 30 bands of UV, optical, and IR data described in Capak et al. (2007b), and compared these

[5] http://www.eso.org/cpl/esorex.html

SEDs with templates from galaxies at known redshifts supplemented with stellar population synthesis models. They computed photo-zs from SEDs using a χ^2 template fitting method which included a treatment of emission lines. The derived $\chi^2(z)$ function was used to compute a probability density function (PDF), $\mathcal{P}(z)$, which is the likelihood that a galaxy lives at a redshift z given the photometric data and the spectral templates used. Rather than collapsing this function to a single value at the mean, median, or peak and assuming Gaussian uncertainty as is often done, we make use of the full PDF to determine group membership, described in § 2.4. We use an updated version (pdzBay_v1.7_010809) of the photo-z catalog presented in Ilbert et al. (2009) with additional deep H band data and small improvements in the template fitting techniques.

Ilbert et al. (2009) demonstrated that these photo-zs are precise and accurate thanks to the broad wavelength range covered by the photometric data and the many bands into which it is divided. Those authors discussed the quality of the photo-zs in comparison with a number of samples of spectroscopic redshifts using the normalized median absolute deviation (NMAD $= 1.48\times$ median($|z_{\rm s} - z_{\rm p}|/(1 + z_{\rm s})$); Hoaglin et al. 1983), which is an estimator for $\sigma_{\Delta z/(1+z_{\rm s})}$ that is robust to outliers. Ilbert et al. (2009) showed that the distribution of offsets between the photometric and spectroscopic redshifts is well-fit by a Gaussian with a standard deviation equal to the NMAD. Applying this estimator to galaxies considered for group membership, i.e., those with F814W < 24.2, $z_p < 1.2$, and an available stellar mass estimate (see § 2.2.4), there are over 12000 spectroscopic redshifts and the overall agreement with photo-zs is $\sigma_{\Delta z/(1+z_{\rm s})} = 0.008$. However, the spectroscopic sample is dominated by the zCOSMOS survey, which has a magnitude limit of $i^+ = 22.5$. The other spectroscopic samples have a variety of selection functions, so we cannot assume that the sample is representative of the full photometric sample of galaxies.

A second measure of uncertainty of a photometric redshift comes directly from the width of the PDF. Ilbert et al. (2009) have shown that the shape of $\mathcal{P}(z)$ is broadly consistent with the distribution of offsets between photometric and spectroscopic redshifts. For example, 65% of objects have a redshift offset within the 68% uncertainty on the PDF, $\sigma_{\mathcal{P}}$. In § 2.3.2, we discuss further tests on the agreement between these two estimates of redshift uncertainty, $\sigma_{\mathcal{P}}$ and $\sigma_{\Delta z}$ (we henceforth drop the conventional factor of $1 + z_{\rm s}$ to make direct comparisons between the two quantities), and we study variations in photo-z quality that could bias our selection against different galaxy populations.

2.2.4 Stellar Mass Estimates

Stellar masses are used in the identification of group centers (see § 2.4.3) and are estimated using the Bayesian code described in Bundy et al. (2006), with good agreement to the masses determined by Drory et al. (2009). For each galaxy, the SED and photo-z described above are referenced to a grid of stellar population synthesis models constructed using the Bruzual & Charlot (2003) code and assuming an initial mass function from Chabrier (2003). The grid includes models that vary in age, star formation history, dust content, and metallicity. At each grid point, the probability that the observed SED fits the model is calculated, and the corresponding stellar mass is stored. By marginalizing over all parameters in the grid, the stellar mass probability distribution is obtained. The median and width of this distribution are taken respectively as the stellar mass estimate and the uncertainty due to degeneracies and the model parameter space. The final stellar mass error estimate also includes uncertainties from the K-band photometry and the expected error on the luminosity distance that results from the photo-z uncertainty, producing a typical final uncertainty of 0.2-0.3 dex. Stellar mass estimates used here require a 3σ detection in K_s-band, which is complete to a typical depth of $K_s = 24$ (McCracken et al. 2010).

2.3 Sample Limits and Quality of Photometric Redshifts

2.3.1 Mass Limits and Quality Flags

In this section we present the sample selection and sensitivity limits for galaxies and groups used in our analysis. Since one of our limiting factors is the decline in photo-z precision at faint magnitudes, we also discuss tests of the accuracy and precision of photo-zs for different galaxy populations to show that our group member sample is not biased by variations in the quality of photo-zs.

As mentioned in § 2.2.1, we consider X-ray detected groups at redshifts $0 < z_G < 1$. Identifying optical associations with X-ray groups becomes more challenging at $z_G > 1$ and typically requires dedicated spectroscopic followup, so we omit high redshift candidates from this work. In addition to the flags from the X-ray catalog describing the quality of the optical identification and centroid uncertainty, we record three additional flags for each group:

- MASK: more than 10% of the area within R_{200c} or within R_s of the X-ray center is masked in optical images or falls outside the edges of the ACS field
- POOR: 3 or fewer member galaxies are associated with the group (using $P_{mem} > 0.5$, see § 2.4)
- MERGER: the projected radius (R_{200c}) drawn from the X-ray center of one group overlaps with that of another by more than 25% and the group redshifts are consistent ($|\Delta z| < 0.01$).

We flag groups in masked regions because their membership may not be adequately represented and central galaxies may not be properly identified. Poor groups are flagged as possibly questionable optical associations or redshift determinations, and merging groups are flagged because the algorithm may confuse membership assignments. Of the 165 X-ray groups with a clear optical counterpart (XFLAG = 1 or 2), 10, 12, and 15 groups are assigned the MASK, POOR, and MERGER flags, respectively. Our rationale for assigning these flags is to attain a group catalog that is as pure as possible, though not necessarily complete.

The left panel of Figure 2.1 shows the halo masses and redshifts for the group sample. Green squares represent the cleanest sample of 129 groups with XFLAG = 1 or 2, and none of the other flags set, black points relax the restrictions on the MASK, POOR, and MERGER flags, and gray dots represent the remaining sources in the catalog with higher values of XFLAG. The red curve shows the 4σ X-ray flux limit reached in 96% of the field of 1.0×10^{-15} erg cm^{-2} s^{-1} converted to a limiting group mass. Coverage is non-uniform, so some groups are detected below this threshold in areas with deeper coverage. Blue lines show the mass and redshift bins used for later analysis.

To be considered for group membership and to derive stellar mass estimates, galaxies must be brighter than F814W < 24.2 and have a photo-z in the range $0 < z_{\rm p} < 1.2$. Galaxies must also have a 3σ $K_{\rm s}$-band detection, for which the typical limiting depth is $K_{\rm s} = 24$. Though the photometry in COSMOS is complete to $i^+ = 26.2$ and has similar depths in other optical filters (Capak et al. 2007b), the $K_{\rm s}$-band detection requirement causes detections in the ACS imaging to become incomplete near F814W=24.2, which is also in the magnitude range where photo-z quality deteriorates rapidly (see § 2.3.2). The F814W filter magnitude correlates more strongly with photo-z precision than longer wavelength filters (the 4000Å break enters the filter range at $z \sim 0.75$ and remains in that range beyond our redshift limit), so we use it to apply the formal magnitude cut at F814W=24.2. Taking this as our primary magnitude cut, we find that only 5% of the sample with F814W < 24.2 is excluded due to a nondetection in $K_{\rm s}$ or a failure to find an acceptable stellar mass fit, with 2% of bright objects (F814W < 22.5) and 8% of faint obects ($23.5 <$ F814W < 24.2) being cut. Because of photo-z uncertainties, we allow galaxies to have a higher redshift limit than the groups in which they reside, giving the $z_{\rm p} < 1.2$ cut.

The right panel of Figure 2.1 shows the stellar masses and photometric redshifts for galaxies meeting the selection criteria. We plot only every third galaxy for clarity. The red curve shows the 85% stellar mass completeness limit calculated for the oldest allowable stellar template at each redshift for the combined requirements of $K_{\rm s} < 24$ and F814W < 24.2. This passive limit is conservative, as younger stellar populations have lower mass-to-light ratios. At $z = 1$, our stellar mass limit is roughly $\log(M_\star/M_\odot) = 10.3$, or $0.25M^*$ (Drory et al. 2009 found $\log(M^*/M_\odot) \approx 10.9$ for the massive end of a double-Schechter function fit to the stellar mass function at $z \sim 1$, with little redshift evolution). Solid blue lines in the figure show the mass and redshift bins for later analyses, and dashed lines are drawn for stellar mass bins that extend significantly below our completeness limits. Our sample has fewer galaxies and groups at $z < 0.2$ than at higher redshifts because of the smaller volume probed, but the increasing volume at higher redshifts allows for good statistical samples.

2.3.2 Tests of Photometric Redshifts

We have described how the increase in photo-z errors at faint magnitudes partially motivates our selection cut on galaxies brighter than F814W $= 24.2$, with the implicit concern that poorer photo-zs degrade our ability to assign galaxies to groups. Here we test how photo-z quality varies with other galaxy properties to ensure that our selection is not biased by systematic errors for certain galaxy populations.

In principle, photo-z quality can depend on any property of an SED or the templates used

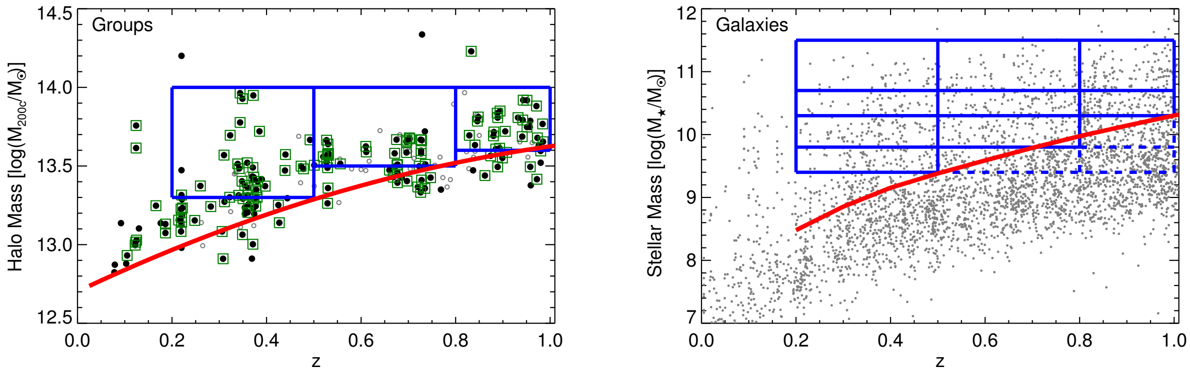

Figure 2.1: Mass limits for groups (left) and galaxies (right) over the redshift range $0 < z < 1$. Symbols for groups denote their quality flags; green squares have XFLAG=1,2 and MASK=POOR=MERGER=0, black filled circles have XFLAG=1,2, and gray open circles are the rest. Red curves denote the mass sensitivity corresponding with the X-ray flux limit (left) and the stellar mass limits for a passive galaxy (right). Blue boxes show the mass and redshift bins used for analysis in § 2.7, with dashed boxes denoting stellar mass bins with significant incompleteness. Only every third galaxy is plotted for visual clarity.

in the fitting process. Redshifts of red galaxies with strong 4000Å breaks have traditionally been easier to constrain than their bluer counterparts. Fainter galaxies have larger photometric uncertainties which propagate into their photo-zs. Galaxy mass and environment may play a role if, for example, the photo-z templates are not representative of evolutionary histories unique to dense group regions. Morphology can also have a subtle effect since the inclination of disks alters the extinction along the line of sight (Yip et al. 2011).

Motivated by these possible sources of variation in photo-z quality, we divide our sample into different populations and quantify the precision and accuracy of their redshift estimates. We also compare two estimates of photo-z uncertainty, the 68% width of the PDF ($\sigma_{\mathcal{P}}$), and the deviation between photometric and spectroscopic redshifts ($\sigma_{\Delta z/(1+z_s)}$).

In order to test the reliability of the redshift uncertainty for different galaxy populations, we slice the galaxy sample into bins based on their brightness, redshift, color, morphology, stellar mass, and environment. Here we use unextincted rest frame colors derived from the best-fitting templates using the difference between absolute magnitudes in near-ultraviolet (NUV) and R bands ($C \equiv M(NUV) - M(R)$) as described by Ilbert et al. (2010). In that paper, spectral classes were identified with the following cuts on C from blue to red:

$$\begin{array}{rl} C < 1.2 & \text{“high activity"} \\ 1.2 < C < 3.5 & \text{“intermediate activity"} \\ C > 3.5 & \text{“quiescent."} \end{array}$$

These classes were found to correlate with visually classified morphologies as expected. For these tests, we use morphologies determined using the Zurich Estimator of Structural Types

(ZEST; Scarlata et al. 2007) on the ACS images. The results are compiled in Table 2.1, in which we present the size and average magnitude of each population, along with the two measures of photo-z uncertainty and the fraction of sources for which the photo-z deviates significantly from the spectroscopic redshift.

The two independent measures of photo-z uncertainty are in good agreement, suggesting that we can safely use PDF widths to quantify the precision of a given photo-z. Furthermore, we do not see strong trends in photo-z quality with galaxy type or environment, and the outlier fraction is typically no larger than a few percent. In particular, the photometric depth in many bands and the treatment of emission lines in fitting SEDs by Ilbert et al. (2009) appears to balance the weakening 4000Å break for bluer galaxies, so that photo-z quality does not significantly depend on color. The lack of strong variations in photo-z uncertainties, and the agreement between the two measures of photo-z uncertainties across galaxy types and environments demonstrates the robustness of these redshifts for different populations. We have not included the photo-zs from Salvato et al. (2009) for AGN due to their rarity and the reasonable accuracy of the photo-zs of Ilbert et al. (2009) for these sources, but future work focusing on AGN may benefit from the improved redshift accuracy.

While the photo-z accuracy is good across the sample, the quality does decrease at fainter magnitudes. We account for this effect when selecting member galaxies by allowing larger tolerances in redshift space for fainter sources. There is also some degradation at higher redshift, but since our sample is not as heavily weighted toward high redshifts as it is toward faint magnitudes, we do not currently account for the redshift dependence of photo-z accuracy when selecting group members. We note that Table 2.1 shows mean magnitudes and photo-z errors for objects that also have spectroscopic redshifts; these errors are representative of the PDF uncertainties for the full galaxy sample in the bright bins, but in the faint bins the spectroscopic sample is brighter than the full population and photo-z errors are smaller than average.

Figure 2.2 illustrates how the photo-z PDF uncertainty varies with magnitude, redshift, and color for the full galaxy sample. The parameter space is divided into bins of $\Delta z_{\rm p} = 0.01$, ΔF814W $= 0.1$, and $\Delta C = 0.1$. For bins containing at least 10 galaxies, the half-width of the median 68% uncertainty on $\mathcal{P}(z)$ is computed and plotted according to the color scale shown. Additionally, we plot the redshift, magnitude, and color distributions of galaxies to characterize the catalog. Clearly the strongest trend in photo-z precision is the decrease in quality at faint magnitudes, and there is only a weak dependence on redshift and galaxy color. Where the group member selection algorithm requires an estimate of redshift uncertainty, we consider only the magnitude dependence of the photo-z uncertainties, ignoring the smaller variations due to color and redshift.

Table 2.1: Photo-z quality for galaxies with spectroscopic redshifts

Sample	N_{obj}	$\langle z \rangle$	$\langle$F814W$\rangle$	med($z_s - z_p$)	$\sigma_{\Delta z}$[a]	$\sigma_{\mathcal{P}}$[b]	$\eta(\%)$[c]
All	12370	0.52	21.3	0.003	0.012	0.013	1.1
Bright; low z	5768	0.31	20.7	0.001	0.009	0.011	1.0
Bright; high z	5613	0.71	21.6	0.006	0.015	0.014	1.0
Faint; low z	280	0.27	23.0	-0.002	0.014	0.016	3.9
Faint; high z	709	0.86	23.0	0.007	0.027	0.024	2.7
Bright; blue	6840	0.52	21.3	0.002	0.011	0.013	1.1
Bright; green	2548	0.44	21.0	0.006	0.014	0.013	1.2
Bright; red	1993	0.55	20.6	0.003	0.010	0.011	0.4
Faint; blue	731	0.70	23.1	0.000	0.021	0.021	3.8
Faint; green	259	0.64	23.2	0.011	0.028	0.027	2.7
Faint; red	67	0.92	23.1	0.013	0.031	0.020	7.5
Bright; early type	2450	0.53	20.4	0.004	0.011	0.011	0.8
Bright; late type	7248	0.49	21.3	0.003	0.012	0.013	0.7
Bright; irregular	1444	0.59	21.3	0.002	0.012	0.012	2.1
High stellar mass	4216	0.62	20.8	0.005	0.013	0.012	1.1
Low stellar mass	8154	0.47	21.5	0.002	0.012	0.013	1.2
Near groups	961	0.45	20.6	0.002	0.011	0.012	0.9
Outside groups	9691	0.54	21.4	0.003	0.012	0.013	1.2
Clean regions	10987	0.53	21.3	0.003	0.012	0.013	1.2
Masked regions	1439	0.51	21.2	0.003	0.013	0.012	2.5
$\mathrm{MMGG_{scale}}$	126	0.49	19.3	0.000	0.009	0.010	0.0
AGN	229	0.56	20.3	0.003	0.015	0.011	1.3

[a]NMAD = 1.48× median[$|z_s - z_p|$]

[b]1.48× median[|68% uncertainty on photo-z PDF|]

[c]Fraction of objects with $|z_s - z_p|/(1 + z_s) > 0.1$

Note. — Brightness bins are divided at F814W=22.5 which is the limiting magnitude for zCOSMOS; redshift bins are split at $z = 0.5$; color bins are $M(NUV) - M(R) < 1.2$ (blue), $1.2 < M(NUV) - M(R) < 3.5$ (green), and $M(NUV) - M(R) > 3.5$ (red); morphologies are categorized by ZEST; stellar masses are separated at $\log(M_\star/M_\odot) = 10.5$; group environments are classified as “near" within R_{200c} of an X-ray group center and where $|z_s - z_G|/(1 + z_G) < 0.005$, and “outside" beyond $3R_{200c}$ and where $|z_s - z_G|/(1 + z_G) > 0.01$. Masked regions are areas in the optical images with bright foreground stars, satellite trails, or image defects. $\mathrm{MMGG_{scale}}$ are the most massive group galaxies within an NFW scale radius of the X-ray center (see § 2.4.3). AGN have been identified in *Chandra* X-ray data (Elvis et al. 2009).

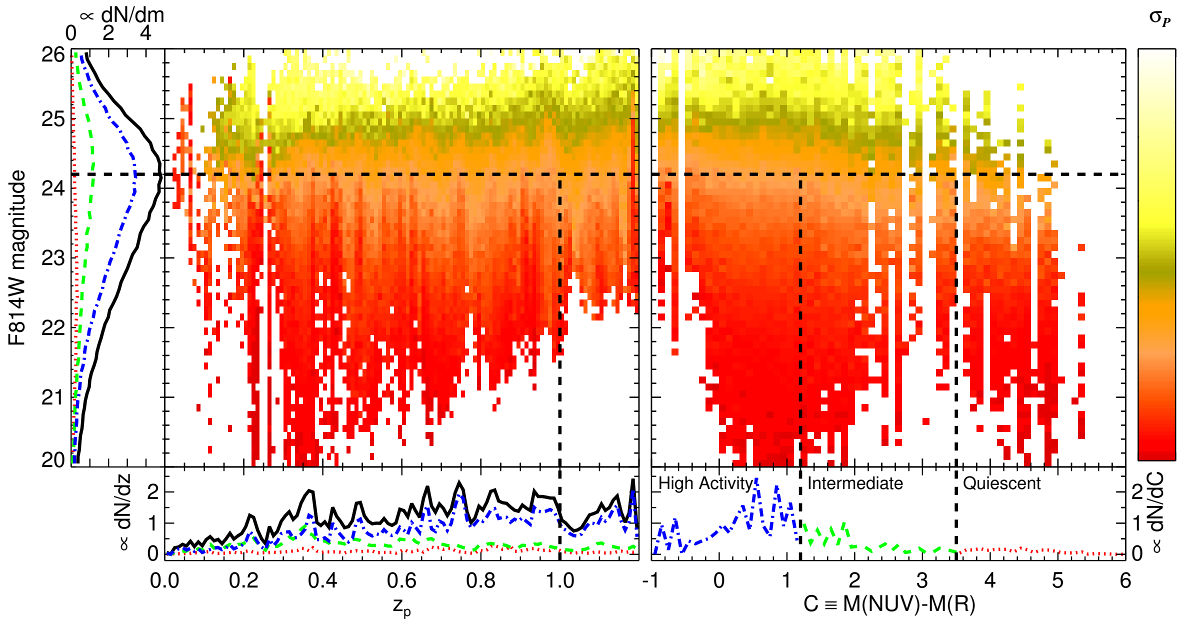

Figure 2.2: Photo-z uncertainties ($\sigma_{\mathcal{P}}$) as a function of magnitude and redshift (left), and color (right). Main panels show photo-z uncertainty in bins colored according to the scale at right. Margin plots on the left side, bottom left, and bottom right show the magnitude, redshift, and color distributions, respectively. Curves are separated by color classification showing all galaxies considered (solid black), "high activity" galaxies (blue dot-dashed), "intermediate activity" galaxies (green dashed), and "quiescent" galaxies (red dotted). Dashed black lines show the galaxy magnitude and group redshift cuts at F814W=24.2 and $z_{\rm G} = 1$ for the sample, as well as the divisions between color types. Ordinate axes on margin plots should be multiplied by 10^4 (left side) and 10^5 (bottom) for normalization. We do not see strong variations in photo-z precision with redshift or color, but there is a significant magnitude-dependence.

2.4 Group Membership Selection

2.4.1 Overview

Our focus is not in *finding* galaxy groups; instead our aim is to associate galaxies with groups that have already been identified as extended X-ray sources. Our basic strategy is to take the locations of groups from the X-ray catalog described in § 2.2.1 and Finoguenov et al. (2007, and in prep.) and assign galaxies to groups based on their positions and redshifts. Previous work on finding group and cluster members has often included assumptions about properties such as their red sequence content, luminosity function, and radial distribution. Because galaxy group populations have not been well-characterized in the mass and redshift range probed by this data set, we do not apply such filters to select members, with the hope that we can then measure these properties in an unbiased manner.

Effectively, we are selecting galaxies in a cylinder oriented along the line of sight around the X-ray position and redshift for each group. The radius chosen for this cylinder is the estimated R_{200c} of each group based on the total mass derived from the X-ray luminosity versus M_{200c} relation for the group sample as determined by weak lensing (Leauthaud et al. 2010). The depth of the cylinder in redshift space is allowed to vary for each candidate member galaxy according to the typical photo-z uncertainty for its apparent magnitude (see Fig. 2.2).

Photometric redshift uncertainties are larger than the typical intrinsic span of a galaxy group in redshift space. A typical photo-z error of $\sigma_{\mathcal{P}} = 0.01$ in redshift-space corresponds to an uncertainty of roughly 40 Mpc in distance along the line of sight, while a halo with $\log(M_{200c}/M_{\odot}) = 13.5$ has a velocity dispersion of $\Delta z_{\mathrm{G}} \approx 0.001$ (Evrard et al. 2008) or a line of sight distance uncertainty of roughly 4 Mpc at $z = 0$. As a result, we must account for contamination of the member sample by galaxies at a similar redshift and position that do not belong to the group. One option is to subtract a mean background density from the number of galaxies found near the group. This statistical background subtraction can be extended to other quantities of interest, such as the total stellar mass in a group, by measuring those quantities averaged over regions away from the group and subtracting them from the values measured at the position of the group. One is left with the measured aggregate quantities for each group, but not a clear list of members and non-members. Another approach is to assign each galaxy a membership probability reflecting the likelihood that it belongs in a group, given some information about the relative number of field galaxies and group members. One can then determine properties of the group by selecting members above a given probability threshold, or by weighting members according to their probability of being a member.

We adopt this Bayesian approach to produce a group member catalog, which can in turn be used to measure a variety of properties about each group without requiring a new statistical background subtraction for each quantity. The selection algorithm thus assigns a probability of membership in a particular group to each galaxy given a number of observables: the projected separation of the group and galaxy in units of the group radius, the redshifts of the galaxy and group along with the typical photo-z uncertainty for the magnitude of the galaxy, and an estimate of the number density of field galaxies relative to group members. Additionally, stellar masses are used to select a central galaxy from the membership list, refining the somewhat uncertain X-ray positions (see § 2.4.3).

2.4.2 Algorithm

In this section, we explain in detail how our selection algorithm works. We reiterate that our task is to identify galaxies that belong to groups rather than to find groups themselves. Our use of photo-z PDFs to associate galaxies to known groups and clusters is similar to the method outlined by Brunner & Lubin (2000); we extend this method to incorporate varying photo-z errors and a prior on the relative fractions of galaxies in groups and the field. The approach presented here was designed with COSMOS data in mind, but may be applicable to other multi-wavelength group and cluster studies, such as optical imaging surveys in fields with SZ or X-ray data. In § 2.5, we consider the quality of our resulting member catalog and how it could be modified by these different data sets. We attempt to keep the discussion here general while inserting details specific to the COSMOS data when necessary. To find the center of a group, we start with the X-ray centroid and then refine this position using the most massive member galaxy near the X-ray position, and finally we update the member list around the new central galaxy (more details on centering are presented in § 2.4.3 and Chapter 3.)

We first consider the field galaxies that can contaminate our selection. The background density of galaxies varies with position, redshift, and magnitude. We measure the number of galaxies in redshift bins ($\Delta z = 0.05$) and magnitude bins (starting at F814W < 21.0, then using a width of 0.8 mag, and ending at $23.4 <$ F814W < 24.2). This count excludes the volume within $3R_{200\mathrm{c}}$ and $z_{\mathrm{G}} \pm 5\sigma_{\mathcal{P}}(\bar{m})$ around all groups in the catalog regardless of flags, where $\bar{m}$ is the mean magnitude of galaxies in the bin. The final results are not strongly sensitive to the choice of volume removed around groups. Figure 2.3 shows this field density $n_F(\mathrm{F814W, z}) = \mathrm{dN_F/dz/d\Omega}$, which is similar to the quantity shown in the bottom left panel of Figure 2.2 but split into magnitude bins. Figure 2.3 also shows the field density as computed by summing the redshift probability distribution functions of galaxies for comparison to the approach of directly counting galaxies in photo-z bins. Despite different sampling intervals ($\Delta z = 0.01$ for the PDFs and 0.05 for bin counting), the methods show excellent agreement.

One can measure the background density locally around groups to account for correlated structure or globally across the field to increase the statistical sample with a larger volume, reducing noise. We have divided the COSMOS field into four separate quadrants to look for variations in n_F with position and find that the values are in reasonable agreement across the field, with the density in individual quandrants deviating from the mean by typically no more than the Poisson errors. When smaller volumes are chosen to estimate the field density surrounding groups, the increased Poisson uncertainty swamps the constraint on locally correlated structure. We thus opt to use the entire area to estimate the mean density of background galaxies as a function of magnitude and redshift. We discuss further the choice of this method of estimating the field density in § 2.5.3.

We next consider candidate member galaxies, constructing a list of those objects in a cylinder with a projected distance from the group center less than R_{200c} and a redshift within $3\sigma_{\mathcal{P}}(m_{\rm max})$ of the group redshift $z_{\rm G}$, where $m_{\rm max}$ is the limiting magnitude F814W=24.2 and $\sigma_{\mathcal{P}} = 0.035$. The number of member candidates can be compared with the field density in Figure 2.3 to estimate the fraction of galaxies that are group members.

For each candidate, we compare the photo-z PDF to the expected redshift distributions of group members and field galaxies. We assume that each galaxy is either a group member (G) or part of the field (F), and assign a Bayesian membership probability using the relative sizes of the group and field populations as a prior to normalize the distributions. While the intial $3\sigma_{\mathcal{P}}$ cut uses the photo-z value $z_{\rm p}$ to make a rough selection, here we use the full distribution $\mathcal{P}(z)$ for each galaxy to account for secondary peaks or other unusual features in the redshift PDF. The probability that a galaxy belongs to a group given $\mathcal{P}(z)$ can be written as

$$P(g \in G|\mathcal{P}(z)) = \frac{P(\mathcal{P}(z)|g \in G)P(g \in G)}{P(\mathcal{P}(z))}. \tag{2.1}$$

The term $P(\mathcal{P}(z)|g \in G)$ is the likelihood of measuring the particular photo-z PDF for a known group member. The prior $P(g \in G) = N_G/(N_G + N_F) = 1 - P(g \in F)$ is based on the relative number of group and field galaxies in the cylinder, and

$$\begin{aligned} P(\mathcal{P}(z)) &= P(\mathcal{P}(z)|g \in G)P(g \in G) + \\ &\quad P(\mathcal{P}(z)|g \in F)P(g \in F) \end{aligned} \tag{2.2}$$

is the probability of measuring $\mathcal{P}(z)$ for any galaxy in the group or field. Each factor in Equation 2.1 has an implicit dependence on magnitude which we omit here and in following equations for notational simplicity, but we do account for magnitude-dependent variations in $\mathcal{P}(z)$ and in the field and group densities.

In order to compare the observed $\mathcal{P}(z)$ with that expected for a group or field galaxy, we must assume a distribution of redshifts for each population. Since the intrinsic velocity dispersion of groups is smaller than the uncertainty in $z_{\rm p}$ we model the true group redshift distribution as a δ-function at $z_{\rm G}$, which is then convolved with a Gaussian of width $\sigma_{\mathcal{P}}(m)$ to account for photo-z measurement uncertainty. We have tested the effects of modifying the true group redshift distribution to be broader than a δ-function to account for intrinsic velocity dispersion but found this correction to be negligible. The redshift distribution of field galaxies is assumed to be uniform near $z_{\rm G}$ and remains unchanged after accounting for photo-z measurement uncertainty. Each of these redshift distributions is convolved with the photo-z PDF $\mathcal{P}(z)$ (note that $\int \mathcal{P}(z)dz = 1$), giving

$$P(\mathcal{P}(z)|g \in G) = \int \mathcal{P}(z)\mathcal{N}(z_{\rm G}, \sigma_{\mathcal{P}})dz \tag{2.3}$$

$$P(\mathcal{P}(z)|g \in F) = \int \frac{\mathcal{P}(z)}{w(\sigma_{\mathcal{P}})}dz \tag{2.4}$$

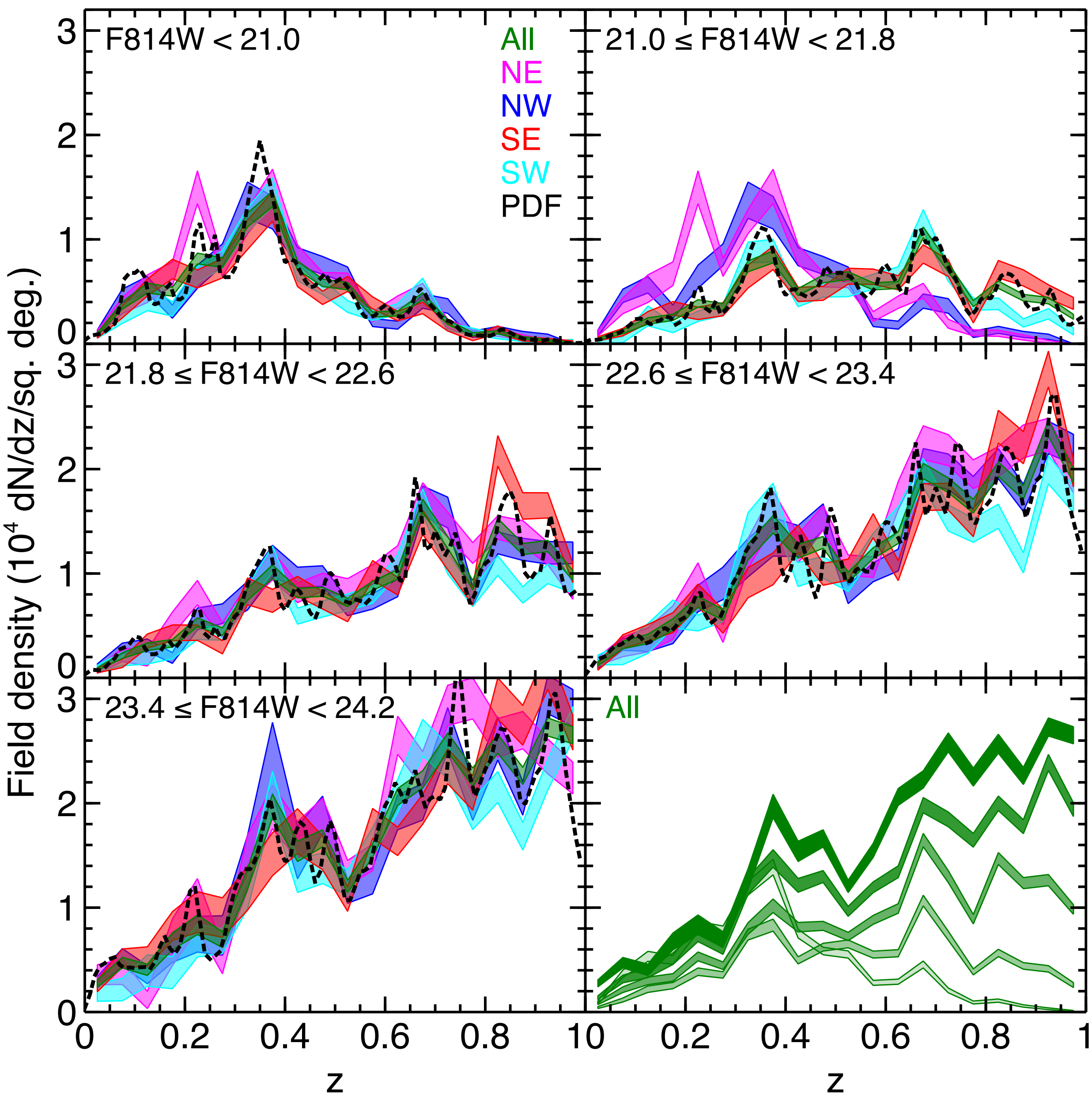

Figure 2.3: Field density as a function of position, redshift, and magnitude. Different colored curves correspond to quadrants of the COSMOS field. The thickness of each curve corresponds to the Poisson uncertainty in each measurement. The dashed black line gives the stacked $\mathcal{P}(z)$ for all galaxies sampled at redshift intervals of 0.01, agreeing nicely with the measurement from counting galaxies in photo-z intervals of 0.05. The variation between quadrants is not large, so we use the mean density across the whole field, shown by the green curve in each of panel and repeated in the bottom right panel for each magnitude bin.

where $\mathcal{N}(z_G, \sigma_\mathcal{P})$ is a Gaussian centered on the group redshift with width equal to the typical $\mathcal{P}(z)$ uncertainty for the magnitude of the galaxy considered. The field density distribution is normalized so that the integral over the redshift range $z_G \pm 3\sigma_\mathcal{P}$ is unity, so the width normalization parameter is $w(\sigma_\mathcal{P}(m)) = 6\sigma_\mathcal{P}(m)$. We have written these convolutions as indefinite integrals, but in reality they are discrete sums sampled at the redshift intervals $\Delta z = 0.01$ and range $0 \leq z \leq 6$ for which $\mathcal{P}(z)$ has been calculated. Because $\mathcal{P}(z)$ is sampled at intervals close to the typical photo-z uncertainty, the distribution can effectively become a δ-function, underestimating the true redshift error which has contributions from template uncertainties as well as photometric uncertainties. So we first convolve $\mathcal{P}(z)$ with a Gaussian of width $\mathrm{d}z = 0.01$ to account for these uncertainties and avoid sharply peaked PDFs.

To estimate the prior, $P(g \in G)$, we begin by counting the number of galaxies in the range $z_G \pm 3\sigma_\mathcal{P}(m)$, measuring $N_{tot} = N_G + N_F$. The measurement of the field density shown in Figure 2.3 provides an independent estimate of n_F, which allows us to calculate an expected number of field galaxies in the cylinder, $\hat{N}_F = \int n_F dz d\Omega$. For each galaxy we linearly interpolate the curve in the relevant magnitude bin to the group redshift, and multiply n_F by the volume searched around the group, $6\pi {R_{200c}}^2 \sigma_\mathcal{P}(m)$, to determine $\hat{N}_F$. This value is subtracted from the measured N_{tot} to determine the expected number of group galaxies in the cylinder, $\hat{N}_G$. We use the estimated values, $\hat{N}_F$ and $\hat{N}_G$, to determine $P(g \in G)$ and $P(g \in F)$, and Equation 2.1 assigns each galaxy a membership probability between zero and one. In cases where a group is not well-detected in a given magnitude bin ($N_{\mathrm{tot}} < \hat{N}_F$, i.e. $\hat{N}_G < 0$), galaxies in the bin are flagged and excluded from membership analysis. Tests in § 2.5 show that excluding these galaxies does not cause significant incompleteness in the member selection.

It is possible for the search cylinders of different groups to overlap, either because they reside in neighboring positions at the same redshift, or because of projections along the line of sight within the redshift uncertainties. In cases where a galaxy is a candidate member of multiple groups, each probability is recorded. A total of 4631 galaxies are assigned high probabilities of membership ($P_{\mathrm{mem}} \equiv P(g \in G|\mathcal{P}(z)) > P(g \in F|\mathcal{P}(z))$, i.e. $P_{\mathrm{mem}} > 0.5$) in a group, and of these members only 163 or 3.5% are also assigned to a second group. For most applications we can restrict our analysis to the highest group membership probability for each galaxy without any significant change in results, but recording each probability assignment will aid in the study of merging groups.

2.4.3 Group Centers

The robust identification of central galaxies is a challenging task, and relevant for a range of applications from satellite kinematics to stacked weak lensing to studying the most massive galaxies (e.g., Skibba et al. 2011). Miscentering is a significant source of systematic uncertainty in measuring the richness and weak lensing signal in optical groups (e.g., Johnston et al. 2007b; Rozo et al. 2011; Rykoff et al. 2011). X-ray data and weak lensing offer additional information about the centers of mass of halos, which we use along with the galaxy content to guide our selection. We outline our approach to determining the optimal tracer of the center of mass here, and present our results in further detail in Chapter 3.

We use the X-ray position as an initial approximation of a group's center, but for these faint detections the position can be uncertain by up to the wavelet detection scale of $32''$($\sim$ 200 kpc at $z = 0.5$), so we consider other data to improve upon these constraints on the centers. Briefly, we have defined multiple candidate centers based on luminosity, stellar mass, and proximity to the X-ray center. By measuring the weak gravitational lensing signal stacked around each of these positions we can find the optimal center which maximizes the lensing signal at small radii. Our results indicate that this optimum center is the member galaxy (i.e., $P_{\rm mem} > 0.5$) with the highest stellar mass within the scale radius plus the X-ray positional uncertainty of the X-ray center. We refer to this object as the $\rm MMGG_{scale}$, for Most Massive Group Galaxy within the scale radius. We assign this galaxy to be the group center, and rerun the algorithm above to find members within $R_{\rm 200c}$ of this galaxy for the final catalog.

Traditional visual selection of group and cluster centers includes looking for a bright, usually early type galaxy near the center of the X-ray or optical distribution, perhaps with an extended stellar envelope. Visual inspections of the Subaru, ACS, and XMM data support our objective selection, with broad agreement between the $\rm MMGG_{scale}$ and the objects one would traditionally identify as central galaxies. Visual selection becomes more ambiguous at high redshift and for groups lacking dominant galaxies, while our selection algorithm makes an objective choice. In a few percent of cases the $\rm MMGG_{scale}$ disagrees with a visually identified central galaxy due to photo-z error or because of a significant offset from the X-ray position putting it outside the scale radius. We do not amend these cases, sacrificing a small degree of accuracy for a uniform and objective selection.

The selection of group centers used here is different than in Leauthaud et al. (2010), which employed a weighting based on stellar mass and distance to the X-ray position. Of the groups that have a confident central galaxy assignment from Leauthaud et al. (2010) and also satisfy the quality cuts for clean groups in § 2.3, 80% are assigned the same central galaxy by the two methods, 9% of the centrals identified by Leauthaud et al. (2010) are too distant from the X-ray center for our method to select, and 4% are not identified as members with the current algorithm. In these cases of disagreement, the selection of Leauthaud et al. (2010) tends to favor more massive galaxies that are farther from the X-ray centroid than the selection used here, with average differences of 0.2 dex in stellar mass and 55 kpc in distance to the X-ray centroid.

2.5 Purity and Completeness

Any selection of group members will have some fraction of false positives, interlopers selected as members that do not belong to a group, and false negatives, true member galaxies missed by the selection. To measure properties of member galaxies, we can weight each galaxy by its membership probability to account for these uncertainties. But we must test the reliability of those membership probabilities, and furthermore, for some applications we wish to define a set of galaxies exceeding a membership probability threshold with a reasonable degree of purity and completeness.

Purity and completeness are measures of overlap between the sample of selected members and the population of true members. We define the purity of the sample, p, to be the fraction of selected members which are also true members. The completeness of the sample, c, is the fraction of true members which are selected. Interlopers are objects which are selected but are not true members and missed galaxies are objects which are not selected but are true members. Formally,

$$\mathsf{p} = \frac{N_{\mathrm{selected}} - N_{\mathrm{interlopers}}}{N_{\mathrm{selected}}} \tag{2.5}$$

$$\mathsf{c} = \frac{N_{\mathrm{true}} - N_{\mathrm{missed}}}{N_{\mathrm{true}}}. \tag{2.6}$$

We can use the values of p and c to estimate N_{true} using $N_{\mathrm{true}} = N_{\mathrm{selected}} + N_{\mathrm{missed}} - N_{\mathrm{interlopers}}$ which can be rearranged into

$$\frac{N_{\mathrm{true}}}{N_{\mathrm{selected}}} = \frac{\mathsf{p}}{\mathsf{c}} \tag{2.7}$$

using Equations 2.5 and 2.6. This correction factor, p/c, can be used to remove bias in the estimate of the intrinsic number of group members, N_{true}, if we understand the purity and completeness of the selection algorithm.

To measure the purity and completeness of our member selection, we must have some way of telling which galaxies truly belong to groups. For our application, we use the subsample of objects with spectroscopic redshifts as well as mock catalogs to obtain knowledge of group membership that is independent of our photo-z selection. The galaxies with spectroscopic redshifts allow us to test the photo-z selection method on the same catalog, directly probing the effect of photo-z uncertainties. But constraints on p and c are limited by the sparseness of spectroscopic coverage, and biases could be introduced since spectroscopic coverage is not representative of the full range of galaxies in the group sample. Furthermore, even spectroscopic selection of group members can have contamination and incompleteness (e.g., Gerke et al. 2005).

We perform further diagnostic tests using mock catalogs from N-body simulations described in § 2.5.2. Mock galaxies are prescribed to occupy halos according to a halo occupation distribution (HOD) model constrained by measurements of clustering, lensing, and stellar mass functions in COSMOS (Leauthaud et al. 2011a,b). After running the selection algorithm on a mock catalog, we can estimate its purity and completeness by comparing the results with the input list of group members. The mocks allow us to study greater volumes than the observed region, increasing statistical precision and providing estimates of the effects of sample variance for the volume probed. Mocks also give direct knowledge of galaxy group membership in real space without the redshift space distortions that mar spectroscopic selection, so we can study how the selection algorithm would perform on data sets with different errors in redshifts or positions. However, caution must be taken to ensure that the mock galaxies adequately represent the reality of correlated structure for all relevant properties, particularly in their distribution of positions, masses, and halo occupation.

In the following sections we describe in more detail our diagnostic tests on the selection algorithm using spectroscopic redshifts and mock catalogs. We begin by testing the tradeoff between purity and completeness for different membership probability thresholds, and proceed to study the principle sources of contamination and incompleteness in our selection.

2.5.1 Spectroscopic Tests

Here we consider the subset of galaxies with spectroscopic redshifts to measure the purity and completeness of the selection and study the effect of photo-z errors. A "true" member in this case is defined to be a galaxy within R_{200c} of the X-ray center and with $c|z_{\rm s} - z_{\rm G}| < 2\sigma_{\rm v}(M_{200c}, z)(1+z_{\rm G})$, where c is the speed of light and $\sigma_{\rm v}(M_{200c}, z)$ is the velocity dispersion from the simulations of Evrard et al. (2008), assuming that the velocity bias between galaxies and dark matter is unity.

As we vary the membership probability threshold for photo-z selection, we can see a tradeoff between purity and completeness shown in Figure 2.4 with black points from the spectroscopic test. Error bars show the standard deviation of 1000 bootstrap samples of the spectroscopic catalog. Restricting the member list to sources with membership probability $P_{\rm mem} > 0.9$ gives a purity and completeness of 80% and 19% respectively. Lowering the membership threshold increases completeness while decreasing purity. In later sections, we use a threshold of $P_{\rm mem} > 0.5$ as a compromise between these competing factors, which for the spectroscopic test produces a purity of 69% and a completeness of 92%.

To further study the quality of the membership selection, we can measure trends in purity and completeness against other properties, seen in Figure 2.5. In this figure, we show how the selection performs for galaxies of different redshift, magnitude, stellar mass, groupcentric distance, and group halo mass, by measuring the purity and completeness of objects assigned $P_{\rm mem} > 0.5$. Figure 2.6 shows the same tests for color and morphology. The results are discussed in more detail in § 2.5.3, but we can see that the selection quality does not vary significantly with redshift or group mass, but does degrade in the outskirts of groups and for faint, low-mass galaxies, which also tend to have blue colors and late type morphologies. We have tested the influence of target selection effects on these results by restricting the spectroscopic sample to zCOSMOS galaxies which were uniformly selected at $i^+ < 22.5$. The purity and completeness measurements are consistent within the error bars of the full sample, but have slightly larger uncertainties due to the smaller sample size.

2.5.2 Mock Catalogs

We use numerical simulations to construct a series of mock catalogs for a COSMOS-like survey to test the reliability of our member selection. Mocks are created from a single

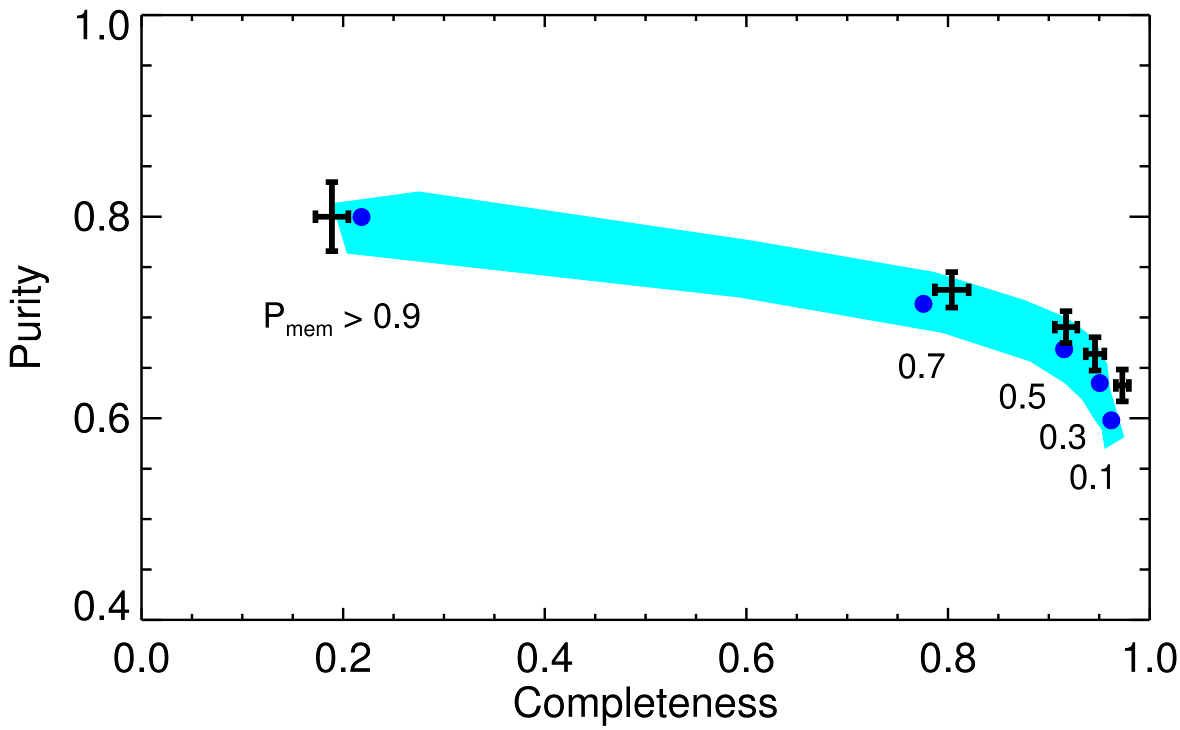

Figure 2.4: Purity and completeness for different membership probability thresholds ($P_{\rm mem} > \{0.1, 0.3, 0.5, 0.7, 0.9\}$) as measured by the spectroscopic subsample (black crosses) and mock catalogs (blue circles, mean of ten lightcones). Error bars are the standard deviation from 1000 bootstrap samples of the spectroscopic catalog. The cyan shaded band is the region spanned by the ten mock lightcones.

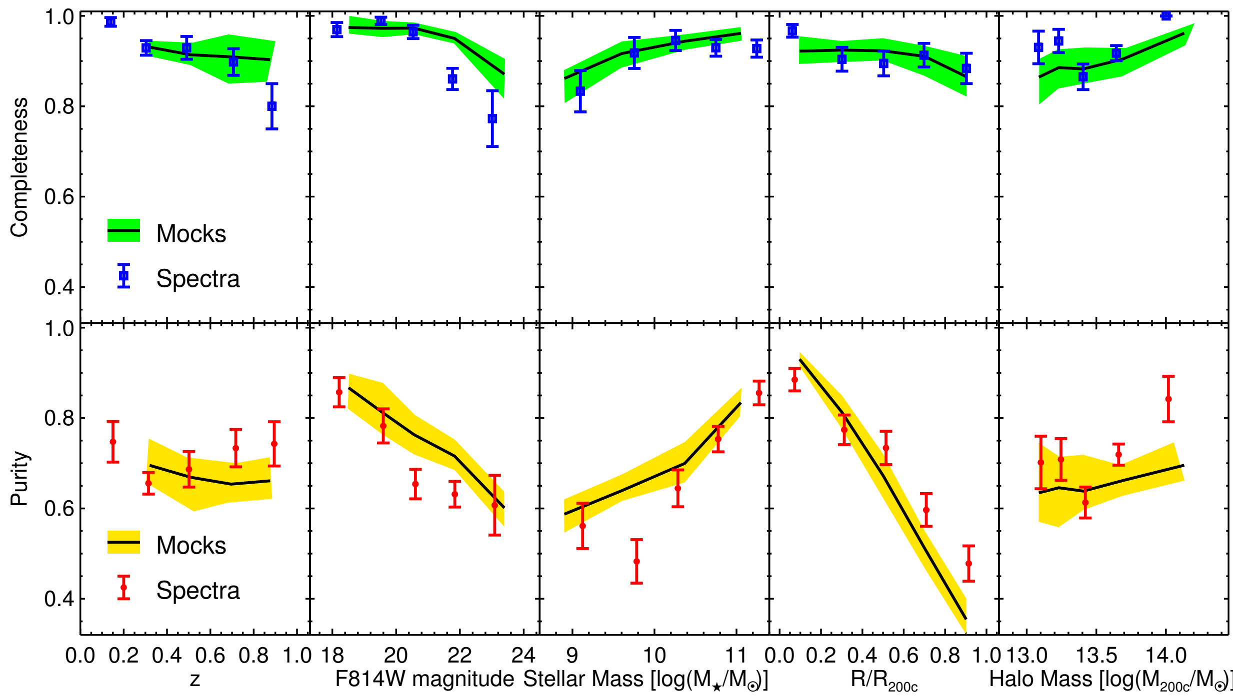

Figure 2.5: Completeness (top row) and purity (bottom row) of the galaxy membership selection as measured by the spectroscopic subsample (points with error bars) and mock catalogs (shaded bands) for galaxies with $P_{\rm mem} > 0.5$. Error bars are the standard deviation from 1000 bootstrap samples of the spectroscopic catalog, and shaded bands show the range spanned by the ten mock lightcones, while the solid black curve represents the mock mean. Bins were chosen to measure a roughly constant number of galaxies for each property tested while still representing the range of observed properties.

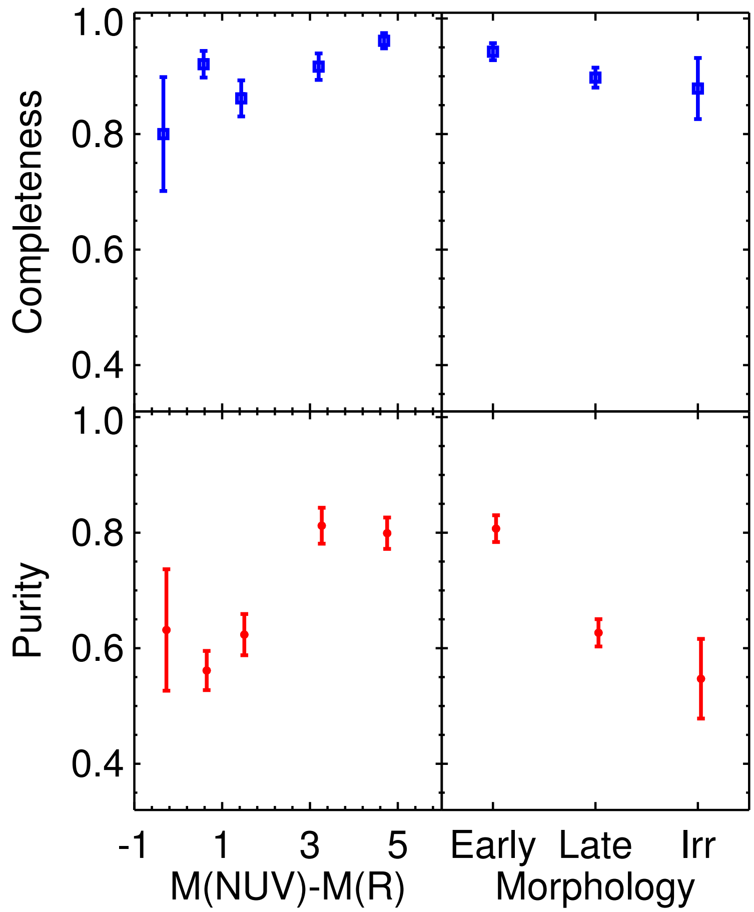

Figure 2.6: Completeness (top row) and purity (bottom row) of the galaxy membership selection as measured by the spectroscopic subsample for galaxies with $P_{\rm mem} > 0.5$. Error bars are the standard deviation from 1000 bootstrap samples of the spectroscopic catalog. Morphological classes are defined from ZEST (Scarlata et al. 2007); the early type category includes ellipticals (type=1) and bulge-dominated disks (type=2.0), the late type category includes the remaining type=2 sources, and irregulars have type=3.

simulation (named "Consuelo"), part of the Las Damas suite (McBride et al., in prep.)[6]. Consuelo is a box of 420 h^{-1} Mpc on a side with 1400^3 particles of mass 1.87×10^9 h^{-1} $M_\odot$ and a softening length of 8 h^{-1} kpc.[7] This simulation can robustly resolve halos with masses above $\sim 10^{11} h^{-1}$ $M_\odot$ which corresponds to central galaxy stellar masses of $\sim 10^{8.5}$ h^{-1} $M_\odot$, well-matched to our completeness limit of F814W=24.2 at $z = 0.2$ (see Figure 2.1).

We extract ten light cones from the Consuelo simulation that have the same area as COSMOS and individually non-overlapping volumes. Halos within the simulation are identified with a friends-of-friends (FOF) halo finder (Davis et al. 1985) with a linking length of $b = 0.2$. For typical halos in the mass range we consider, FOF masses and spherical overdensity masses (defined within a radius where the mean density is 200 times the background) typically agree within $\sim 10 - 20\%$ (Tinker et al. 2008); we thus only convert from background to critical overdensity to obtain M_{200c}. Halos are populated with galaxies using the HOD model of Leauthaud et al. (2011a,b) that simultaneously fits the stellar mass functions, galaxy clustering, and galaxy-galaxy lensing signals of COSMOS. We adopt the $z \sim 0.6$ HOD model of Leauthaud et al. (2011b) with the following parameters from Table 5 of that paper: $\log(M_1) = 12.725$, $\log(M_{*,0}) = 11.038$, $\beta = 0.466$, $\delta = 0.61$, $\gamma = 1.95$, $\sigma_{\log M_*} = 0.249$, $B_{\rm cut} = 1.65$, $B_{\rm sat} = 9.04$, $\beta_{\rm cut} = 0.59$, $\beta_{\rm sat} = 0.740$, $\alpha_{\rm sat} = 1$. Details regarding the parameters in this HOD model can be found in Leauthaud et al. (2011a). As shown in Leauthaud et al. (2011b), there is a small amount of redshift evolution in this parameter set from $z \sim 0.2$ to $z \sim 1$. However, the redshift evolution should not have a large impact on our assessment of the completeness and purity of the group membership selection and so we neglect the redshift evolution of the HOD in this work.

Galaxies are assigned cosmological redshifts as well as mock spectroscopic redshifts which include the effect of peculiar velocities from the velocity dispersion within halos. Photometric redshifts are drawn from a Gaussian distribution centered around the spectroscopic redshift with width equal to the photo-z uncertainty for that magnitude. A Gaussian $\mathcal{P}(z)$ is then centered at $z_{\rm p}$ with the same width, and sampled at the same redshift interval as the PDF for real galaxies. We do not include catastrophic photo-z errors which are shown in Table 2.1 to be a small fraction of the sample.

The HOD model of Leauthaud et al. (2011a) assigns stellar masses to mock galaxies but does not assign magnitudes or colors. In order to apply a similar magnitude cut to the mock galaxies as used in the selection algorithm, we assign F814W magnitudes to mock galaxies. For each mock galaxy, we construct a galaxy sample from the COSMOS data that is matched in redshift and stellar mass in bins of $\Delta z = 0.02$ and $\Delta \log(M_\star/M_\odot) = 0.2$. An F814W magnitude is assigned to each mock galaxy by randomly drawing a magnitude from the matched sample. We do not assign colors or morphologies to mock galaxies since the dependence of these properties on redshift and environment are not well-constrained. We will rely on our spectroscopic sample in order to determine the completeness and purity of the group membership selection as a function of color and morphology instead of using mock

[6]Details regarding this simulation can be found at http://lss.phy.vanderbilt.edu/lasdamas/simulations.html

[7]We use $H_0 = 100$ h km s^{-1} Mpc^{-1} in this paragraph only.

catalogs.

Mock halos are given the redshift of the central galaxy and X-ray luminosities according to the mean $L_X - M_{200c}$ relation of Leauthaud et al. (2010). To mimic the position uncertainties of the X-ray detections, XFLAG quality flags 1 or 2 are assigned randomly in proportion to their appearance in the COSMOS group catalog. The nominal group center is offset from the central galaxy with a Gaussian scatter of $32''$ for XFLAG = 2 halos which is reduced by the measured flux significance for XFLAG = 1 halos, and we assume a typical 5σ flux measurement. The impact of centroiding errors is investigated in § 2.5.4.

Next we run the membership algorithm described in § 2.4 on the mock galaxy and halo catalogs, associating galaxies with halos. We can perform the same purity and completeness tests as with the spectroscopic sample above, but this time we know the halo membership *a priori*. The results from these mock catalog tests are presented alongside those for the spectroscopic subsample as colored bands in Figures 2.4 and 2.5.

2.5.3 Sources of Error

Results from the tests on spectroscopic data and mock catalogs above can differ because the spectroscopic sample is weighted toward bright objects and because our knowledge of true membership in the spectroscopic data is limited by redshift-space distortions, while membership in the mock catalogs is known by design. The general agreement seen in Figures 2.4 and 2.5 between these tests of membership quality is encouraging, and it suggests that the biases are modest and that the mock catalogs accurately represent the properties of real galaxies that we wish to study. The normalization of the purity and completeness curves for the spectroscopic test has a degree of freedom in the velocity width used to determine whether a spectroscopic redshift is consistent with a group redshift. We used the criterion $c|z_s - z_G| < 2\sigma_v(M, z)(1 + z_G)$ for spectroscopic membership; a broader velocity range for the spectroscopic test would result in a higher measured level of purity and lower completeness in the photo-z selection, and the converse holds for a smaller velocity range, shifting the curves up or down. Though the *absolute* measure of purity and completeness in the spectroscopic tests holds some degree of arbitrariness, the *relative* trends shown in Figure 2.5 are in general agreement with the mocks, with some offsets likely due to sampling bias and redshift-space distortions. We study the effects of redshift-space distortions on member selection in the limit of a completely spectroscopic survey in § 2.5.4.

Information from the spectroscopic tests has the advantage that it can probe member selection effects due to properties that cannot easily be modeled (e.g., galaxy color and morphology), and these tests directly measure the effects of photo-z errors on our selection of galaxies in the same set of groups. We see in Figure 2.6 that the trends of selection quality with color and morphology parallel the trends with magnitude and stellar mass from Figure 2.5. We have shown in § 2.3.2 that photo-z quality is not strongly affected by color or morphology, and no other inputs to our selection algorithm explicitly depend on these properties. We infer that the lower completeness and purity seen for faint, low mass, blue, and late type galaxies is driven by two effects; fainter galaxies have larger photo-z

uncertainties, and galaxies in this population tend to live outside of dense groups so that they are more likely to be contaminants when selected.

Because only a fraction of objects have spectroscopic redshifts, the uncertainties can be large. Tests with mock catalogs alleviate this issue and provide an estimate of the sample variance in our selection due to the finite size of the COSMOS region. An additional advantage of the mocks is that the central galaxy of each halo is known, so we can test the success rate for identifying these objects. We find that 77% of central galaxies are correctly identified as the $\mathrm{MMGG_{scale}}$ galaxies in the corresponding halos, 12% are misidentified as satellites because the central galaxy is not the most massive member near the centroid, 5% are misidentified as satellites because the assigned centroid error puts the galaxy outside of the search region, and only 5% are assigned to neighboring groups or the field due to photo-z errors. While the HOD used to create the mocks allows for satellite galaxies to be more massive than centrals due to scatter in the relation between stellar mass and halo mass, the fraction of groups where this occurs is sensitive to the parametrization of the HOD model and is not well-constrained. The problem of identifying group centers will be discussed in more detail in Chapter 3.

For the full sample of mock galaxies with $P_{\mathrm{mem}} > 0.5$, we find a mean purity of 67% and completeness of 92%. Looking at Figure 2.5, it is clear that the dominant source of impurity comes from galaxies in projection near the outskirts of groups. We can attribute this contamination to the fact that the density of true members falls steeply as a function of distance from group centers while our membership algorithm selects galaxies uniformly out to $R_{200\mathrm{c}}$. Faint galaxies are another source of impurity since their photo-z errors are larger than average. Galaxies with lower masses and bluer colors are more common in the field than in dense environments (see § 2.7), so a higher contamination fraction from these populations is to be expected. There is also a slight dependence on halo mass, since the density contrast between the field and groups is smaller for low mass halos, lowering the assigned membership probabilities of candidate members and reducing the completeness of the selection. These factors motivate the use of matched filters in finding groups and clusters when the properties of their galaxy populations are well-characterized; we have not employed such filters to avoid biasing our sample and because galaxy properties in this range of halo masses and redshifts are not thoroughly constrained.

The covariance between these galaxy properties makes it challenging to isolate their influence on the contamination fraction. For example, the correlation between the stellar mass and brightness of a galaxy means that the corresponding panels of Figure 2.5 are related and not independent probes of contamination sources. The simplest way to increase the purity of the group sample is to consider only galaxies at smaller distances from the group center than the cut of $R_{200\mathrm{c}}$ used here. Restricting the mock sample to $R < 0.5R_{200\mathrm{c}}$ results in a mean purity and completeness of 84% and 92%, respectively.

An alternative way to address the contamination and incompleteness of the selection would be to apply correction factors to the member selection as a function of these properties, as in Equation 2.7. This would amount to introducing strong priors to the membership algorithm based on our HOD model, limiting the independence of the sample. In testing this approach however, we have noticed that the correction factor as a function of group-centric radius is not significantly tied to other properties such as magnitude, stellar mass, or color, indicating that the contamination is due more to geometry than distinct populations of galaxies. This suggests that we can reliably study the relative radial trends of these properties, though the absolute radial trends are subject to uncertainties in the correction factor.

We can compare the member selection used here with that of Giodini et al. (2009), who used a statistical background subtraction on the same body of data to determine galaxy membership and estimate the total stellar mass in groups. Because the statistical background approach does not individually assign galaxies to groups, we cannot directly compute the purity and completeness of the selection, but we can compare the total stellar mass estimates from the two selection methods to the mock values. Giodini et al. (2009) selected candidate members within a projected radius R_{500c} of X-ray centroids and $0.02 \times (1 + z)$ of the group redshift, and estimated a mean foreground/background contribution in 20 non-overlapping field regions of the same size and redshift.

We run both member selection methods on the mocks, applying to each method the same corrections described by Giodini et al. (2009) to deproject the cylindrical search volume into a sphere of radius R_{500c} and to account for stellar mass contributions below our sensitivity limit, adapted to the stellar mass function and limits of our mocks. The mean stellar mass content in groups recovered using their method is 3% lower (3% higher) than the input mock value in the redshift range $0.2 < z < 0.5$ ($0.5 < z < 1.0$). With the same corrections, our selection method estimates the mean stellar mass to be 3% higher (9% higher) than the mock values over the same redshift intervals. The typical scatter of 35% between the recovered values and the input values for a given group is much larger than the offsets for both methods, but with these tests on mock catalogs we could remove the small biases in future measurements. The mean stellar masses inferred by the two methods happen to be quite similar because they are typically dominated by massive galaxies for which membership assignment is relatively straightforward. However, we note that the full membership selected can be quite different because our approach optimizes group centers using the weak lensing signal and handles magnitude-dependent photometric redshift uncertainties, whereas Giodini et al. (2009) use the X-ray centers and a fixed redshift window.

We can also test different methods of estimating the field density to see how it influences our member selection. Our selection algorithm estimates $\hat{N}_F$ from the mean density across the whole field, but smaller regions could instead be used to estimate the local density around individual groups. While the local density estimate has the advantage that it traces correlated structure around groups, it does suffer from greater shot noise than the density estimated over a larger volume. We have tested our approach by using annuli centered on each group with inner and outer radii of $2R_{200c}$ and $5R_{200c}$, while keeping the rest of the selection algorithm the same. With this approach, the typical field density is higher due to clustering around groups and the resulting membership probability is slightly lower (increasing the field density by a factor of 2 typically lowers the membership probability by only $\sim 20\%$), but the purity and completeness of the sample are essentially unchanged, and the fraction of members crossing a threshold of $P_{\rm mem} > 0.5$ between samples is less than 10%. We obtain similar results when substituting the background estimation method used by Giodini et al. (2009) for our field density prior, so the selection algorithm is not strongly sensitive to the approach used for background estimation.

2.5.4 Applicability to Other Surveys

In view of other surveys which will search for groups and clusters in multi-wavelength data, and to better characterize the advantages or shortcomings of the COSMOS data used in this analysis, we test our selection algorithm on mock catalogs with different levels of uncertainty in redshift and centroid measurements. We consider five hypothetical data sets: a full spectroscopic survey where all galaxies have the typical redshift uncertainty in zCOSMOS[8] of $\sigma_z = 3.7 \times 10^{-4}$, a low-resolution spectroscopic survey like PRIMUS (Coil et al. 2010) with redshift uncertainties of $\sigma_z = 0.005$, a photometric survey with fewer bands and larger photo-z errors like SDSS (Csabai et al. 2003) or DES (Banerji et al. 2008) with $\sigma_z = 0.05$, a deeper X-ray survey with more precise centroids of $3''$, and a lower resolution X-ray or SZ survey with centroid uncertainties of $1'$. In the first three mock surveys we vary only the redshift uncertainty and apply the same centering uncertainty as the fiducial COSMOS mocks described in § 2.5.2 assuming similar X-ray detections. In the final two mock surveys we use the magnitude-dependent redshift uncertainties of the COSMOS mocks and assign centroiding uncertainties, $\sigma_{\rm X}$, in each dimension on the sky. We offset the nominal centroid from the central galaxy in each dimension by a random value drawn from a Gaussian of width $\sigma_{\rm X}$. In all cases we keep the same group and galaxy detection limits as in the COSMOS data.

Figures 2.7 and 2.8 show the purity and completeness obtained when applying our member selection algorithm to these mock surveys, in a manner similar to Figure 2.5. We reiterate that these statistics describe the accuracy of the assignment of galaxies to groups, and not the detection of groups themselves. The figure illustrates that purity and completeness improve as redshift and centroid uncertainties decline. A number of other points can be made about these results:

- Deeper and more complete spectroscopic coverage would improve our member selection, increasing the purity of the sample from $\sim 70\%$ with photo-zs to $\sim 85\%$. Improvements for completeness would mainly be gained from faint galaxies near our magnitude limit.

- Among spectroscopic redshifts, high precision is not critical. The completeness of the $\sigma_z = 3.7 \times 10^{-4}$ and 0.005 samples are nearly identical, and the higher precision spectra provide only a modest improvement in sample purity over the low-resolution spectra, from $\sim 80\%$ to $\sim 85\%$. Once the redshift measurement uncertainty becomes comparable to the magnitude of intrinsic redshift distortions due to peculiar velocities in groups, additional spectral resolution does not greatly improve our ability to identify

[8] http://archive.eso.org/archive/adp/zCOSMOS/VIMOS_spectroscopy_v1.0/index.html

members. PRIMUS data in the COSMOS field will improve upon the existing sampling of zCOSMOS, but we note that the completeness limit for that survey is $i = 22.5$ with sparse sampling to $i = 23.5$, still shallower than our photo-z depth of F814W=24.2.

- The precise photometric redshifts available in the COSMOS field are critical for identifying members using our approach. Redshifts that are less accurate or precise show significantly reduced purity and completeness.

- The precision of X-ray centroids for COSMOS groups is quite sufficient for member selection. Improving the positional uncertainty by roughly a factor of eight from the mean COSMOS value results in only a few percent improvement in completeness and a negligible gain in purity. Conversely, less precise centers (such as those available from SZ measurements) produce a sample with lower purity in the central region ($\sim 85\%$ instead of $\sim 95\%$) and significantly lower completeness ($\sim 75\%$ instead of $\sim 90\%$). Though the existing COSMOS centroids are adequate for assigning member galaxies to groups, we note that several aspects of groups could still be studied with deeper X-ray or SZ data including physical offsets between central galaxies and hot gas, and the relationships between temperature or entropy with other group properties.

- Note that we do not optimize our selection algorithm for these hypothetical data sets. Combining catalogs built from different observables (e.g., Cohn & White 2009), and other techniques such as iterative centering or matched filters could improve results.

We can compare the results of our mock spectroscopic selection to other methods in the literature. We must note that our definitions of purity and completeness refer to the success rates for assigning members to known groups, while previous spectroscopic group-finding efforts have typically quantified the purity and completeness of the identified group catalog in addition to the galaxy membership assignment. In our mock tests, we have implicitly assumed that the identification of groups is pure and complete. It is also difficult to make direct comparisons across surveys because of differences in data sets, limiting depths, and mock catalogs. However, looking briefly at the quoted purity and completeness of spectroscopic group catalogs, we can assess our algorithm and see the advantage to assigning group membership when the existence of a group is already know (e.g., from an X-ray detection).

Using a tesselation method to find galaxy groups in DEEP2 with a limiting galaxy magnitude of $\mathrm{R_{AB}} = 24.1$, Gerke et al. (2005) attained a mean interloper fraction (analogous to our impurity, $1 - \mathsf{p}$) of $f_I = 0.458 \pm 0.004$ and a mean galaxy success rate (analogous to our completeness) of $S_{\mathrm{gal}} = 0.786 \pm 0.006$ in their mock tests. They reported a one-way group identification purity of $P_1 = 0.545 \pm 0.005$ and completeness of $C_1 = 0.782 \pm 0.006$. Knobel et al. (2009) found that a friends-of-friends approach performed better than the tesselation method for identifying groups in zCOSMOS to a limiting magnitude of $\mathrm{I_{AB}} = 22.5$, and reported values of $f_I = 0.29$, $S_{\mathrm{gal}} = 0.84$, $P_1 = 0.66$, and $C_1 = 0.81$ from their mocks. These values are for groups with $N_{\mathrm{mem}} \geq 2$, and while Gerke et al. (2005) showed values for group

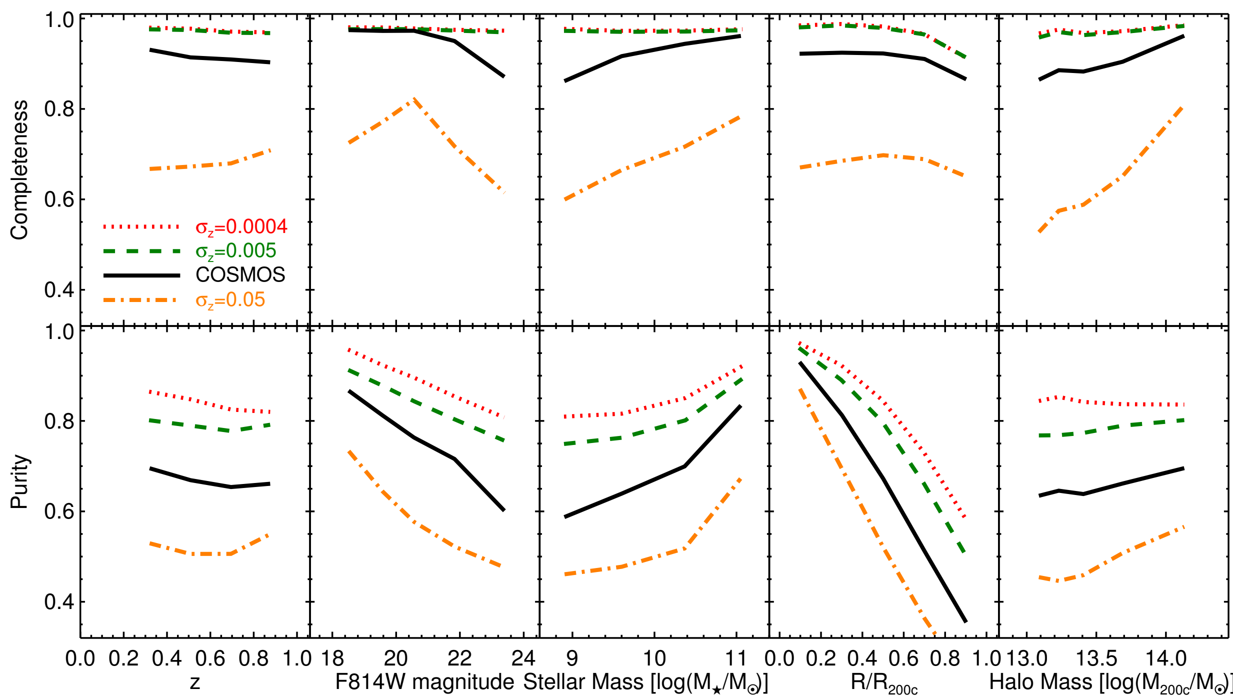

Figure 2.7: Completeness (top row) and purity (bottom row) of the galaxy membership selection for hypothetical surveys with different redshift uncertainties according to the legend. Each curve represents the mean of ten mock lightcones. The fiducial survey is the same as that plotted in Figure 2.5 for COSMOS. Note that the completeness curves for $\sigma_z = 0.0004$ and 0.005 lie atop one another.

purity and completeness that were roughly constant with group velocity dispersion, Knobel et al. (2009) showed that each of these statistics improved when restricting the sample to higher richness groups, flattening out for groups with $N_{\rm mem} \gtrsim 5$. Disentangling the effects of group identification from galaxy membership assignment is difficult, but since the reported $S_{\rm gal}/C_1$ and $(1 - f_I)/P_1$ are both approximately unity, it appears that the main challenge in assigning galaxy membership with these algorithms is in identifying real groups. This fact illustrates the advantage of combining group-finding methods to ensure a reliable sample of groups before assigning members.

2.6 Member Catalog

In the spirit of public releases of COSMOS data, we make our membership assignments available as machine-readable files through the NASA/IPAC Infrared Science Archive

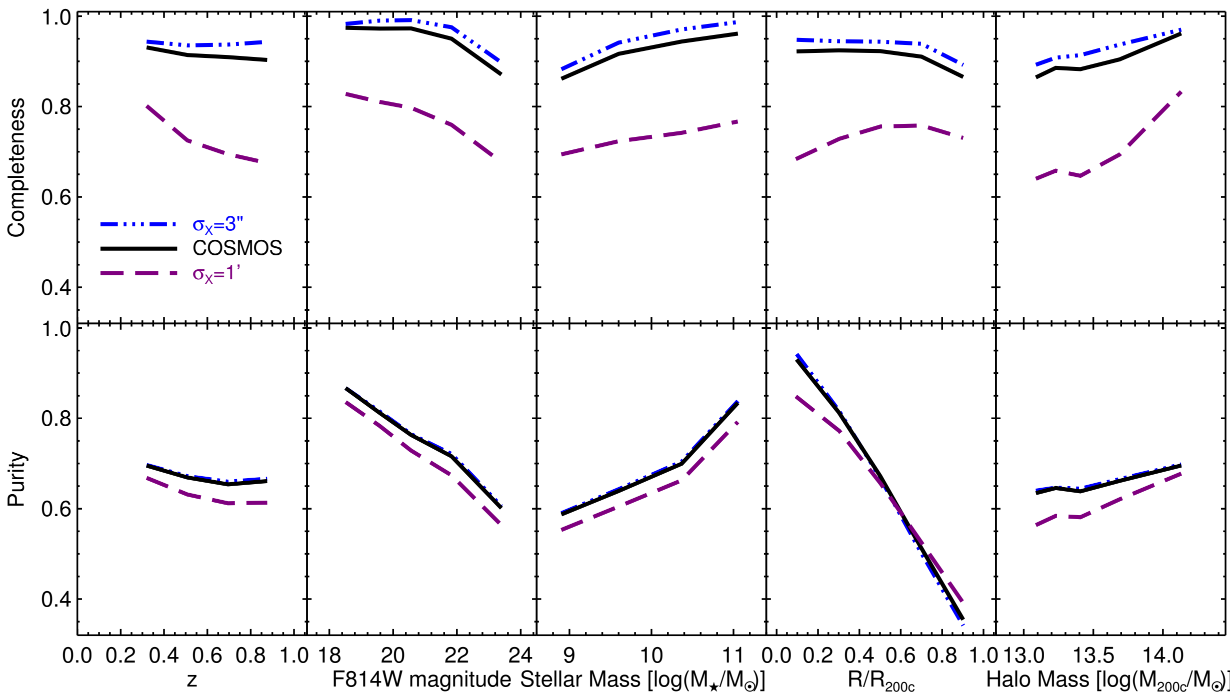

Figure 2.8: Completeness (top row) and purity (bottom row) of the galaxy membership selection for hypothetical surveys with different centroid uncertainties according to the legend. As in Figure 2.7, each curve represents the mean of ten mock lightcones, and the fiducial survey is the same as that plotted in Figure 2.5 for COSMOS.

Table 2.2: Basic catalog properties

Property	Value
Field coordinates (J2000)	RA=(149.°4, 150.°8), Dec=(1.°57, 2.°90)
Group redshift	$0 < z_G < 1$
Galaxy magnitude	F814W < 24.2
Halo mass	$12.8 < \log(M_{200c}/M_\odot) < 14.2$
X-ray luminosity	$41.3 < \log(L_X/\mathrm{erg\ s^{-1}}) < 44.1$
N_{groups}	211
N_{groups} (XFLAG $= 1, 2$)	165
N_{groups} (clean groups)[a]	129
$N_{mem}(P_{mem} > 0.5)$	4639
$N_{mem}(P_{mem} > 0.5$, clean groups)	3415
$N_{mem}(P_{mem} > 0.5, R < 0.5R_{200c}, \log(M_\star/M_\odot) > 10.3)$	867
$N_{mem}(P_{mem} > 0.5, R < 0.5R_{200c}, \log(M_\star/M_\odot) > 10.3$, clean groups)	656

[a]XFLAG $= 1, 2$, MASK=POOR=MERGER=0

(IRSA)[9]. These data include galaxy positions, redshifts, stellar masses, colors, and membership probabilities, along with group identifications. For each group we provide the X-ray position, flux, and luminosity, along with the redshift, halo mass, quality flags, and the position and stellar mass of the central galaxy $\mathrm{MMGG_{scale}}$. For reference, the basic parameters describing the catalog are compiled in Table 2.2. For analyses requiring a clean selection of galaxy groups, we restrict the sample to groups with XFLAG $= 1$ or 2 and the MASK, POOR, and MERGER flags blank to ensure that groups and members have been reliably identified; in the group catalog we define a new property, FLAG_INCLUDE, to encode this combination of selection cuts. When a pure and complete sample of members is needed, we select galaxies with $P_{mem} > 0.5$ in the inner regions of groups, $R < 0.5R_{200c}$, with stellar masses above our sample limit shown in Figure 2.1.

In addition to the catalog described above using photometric redshifts, we have also produced a catalog replacing photo-zs with spectroscopic redshifts when available. We use the same selection algorithm and replace $\mathcal{P}(z)$ from the photo-z with a Gaussian of width equal to the typical uncertainty in zCOSMOS, $\sigma_z = 3.7 \times 10^{-4}$, and sample each distribution at intervals of 10^{-5} in redshift. This catalog has better purity and completeness than the photo-z catalog because of the improved redshift accuracy, but the selection is less homogeneous because spectroscopic sampling is not representative or complete.

2.7 Analysis and Discussion

With the catalog of group members identified and the purity and completeness of the sample characterized, we provide a first look at the properties of galaxies in these groups. Here we present an analysis of the colors of group members relative to the field. Elsewhere we study member properties in more detail, including galaxy morphologies and star formation rates with respect to group properties like redshift, halo mass, and group-centric distance 4.

[9]http://irsa.ipac.caltech.edu/Missions/cosmos.html

Figure 2.9 shows the unextincted rest-frame NUV-R colors from Ilbert et al. (2010) for group members. We use the clean sample of groups, selecting members with $P_{\rm mem} > 0.5$ within $R_{\rm 200c}$ of the group center. The apparent banding in colors is due to the finite number of templates used. We call galaxies identified as the $\rm MMGG_{scale}$ "centrals" with the other members as "satellites." We see a bimodal distribution in color space for both central and satellite galaxies, though redder colors are more common than blue for both types of members. In the margin plots, we show the distributions of colors and stellar masses for centrals and satellites, as well as field galaxies not assigned to any X-ray detected group ($P_{\rm mem} = 0$). The field sample has been selected to match the redshift distribution of group members in bins of $dz = 0.1$. Although the color distribution of field galaxies is also bimodal, it is clear that bluer galaxies are more common in the field than in groups, a well-known result in clusters and dense environments over a range of mass scales and redshifts (e.g., Gerke et al. 2007).

We also see that there exist a number of blue centrals, which are of interest because they suggest that star formation can persist or be reactivated in the centers of dense groups, or that AGN exist there. The set of red points in Figure 2.9 omits ambiguous cases where there is a more massive galaxy in the outskirts of a group or where the $\rm MMGG_{scale}$ differs between the photo-z-only catalog and the one supplemented with available spectroscopic redshifts; 79% of groups satisfying the quality cuts of § 2.6 have an unambiguous central according to these criteria. While the majority of this sample of centrals are red (77 out of 102), there are 5 centrals with blue colors indicative of active star formation or AGN, and 20 centrals with colors indicating intermediate activity. This population warrants further study to verify that they are accurate centers and to determine what environmental factors could contribute to the star formation or AGN activity.

2.7.1 Environmental Dependence from $z = 0.2$ to 1

The higher fraction of blue galaxies in the field compared to groups shown in Figure 2.9 indicates that star formation is less common in dense environments. As discussed in the introduction, much work has been carried out to determine whether this well-known effect is due to a physical process acting on galaxies in dense enviroments to suppress their star formation rates, or due to the intrinsic properties of galaxies that exist in these regions.

To distinguish between the possibilities of environmental influence and innate differences, we compare galaxy colors in group and field environments within fixed stellar mass bins. We measure the fraction of galaxies of the quiescent type defined by Ilbert et al. (2010), i.e. those with $M(NUV) - M(R) > 3.5$. These are unextincted rest-frame colors from the spectral template that best fits each galaxy's SED, allowing us to study intrinsic colors that are related to specific star formation rates without the obscuring effects of dust. The correction is important because galaxies in low density environments have a higher dust content, even among massive galaxies (Kauffmann et al. 2004).

The fraction of red galaxies in fixed stellar mass bins is plotted for three redshift ranges in Figure 2.10. For group members, we consider only galaxies with membership probability

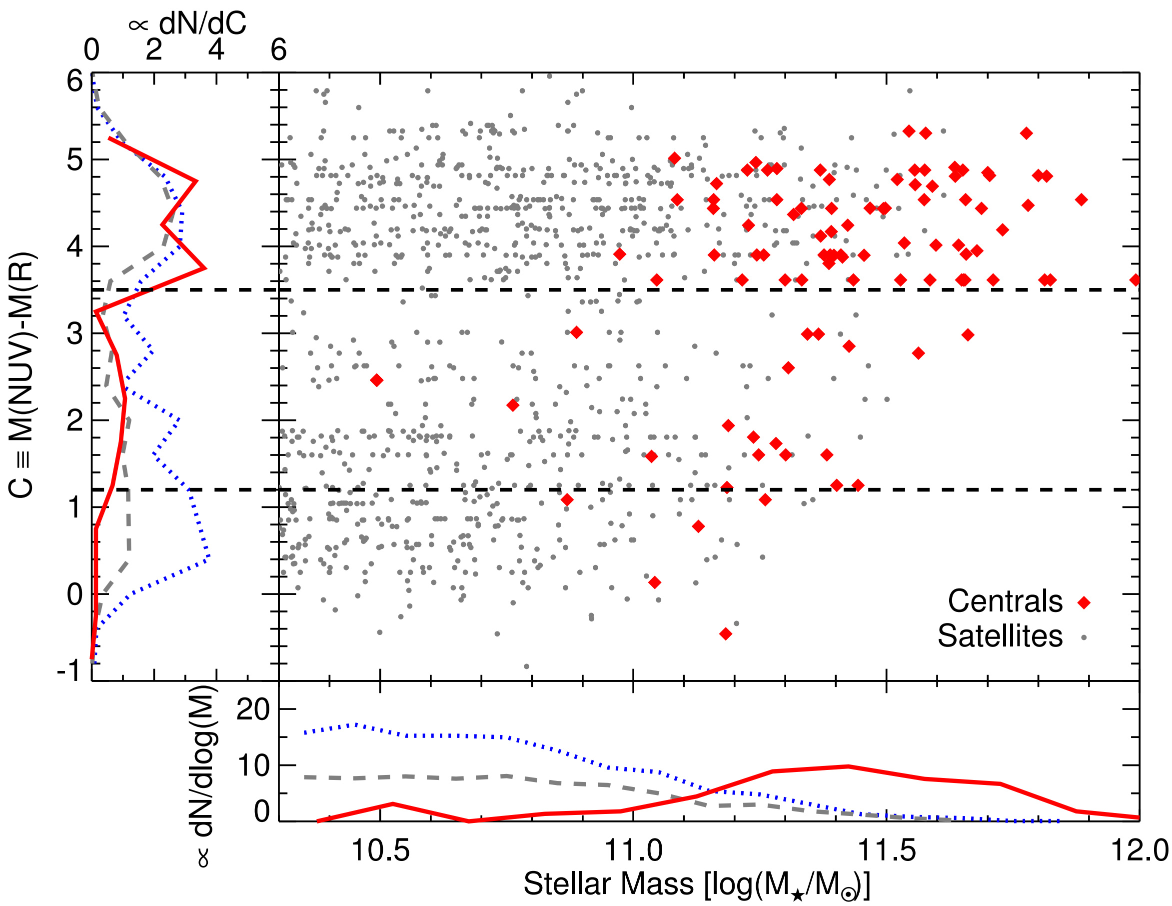

Figure 2.9: Stellar masses and unextincted rest-frame template colors for central galaxies (red diamonds) and satellites (gray dots). We plot only the unambigous centrals, i.e.those designated as the $\mathrm{MMGG_{scale}}$ in groups which do not have a more massive galaxy in the outskirts or a discrepancy between identification with spectroscopic and photometric redshifts. Horizontal dashed black lines show the galaxy spectral classes of Ilbert et al. (2010). Margin plots show the distribution of colors and stellar masses for centrals (red solid), satellites (gray dashed), and a redshift-matched sample of field galaxies (blue dotted), rescaled for comparison. Axis labels should be multiplied by 15 (centrals), 150 (satellites), and 500 (red-shift matched field sample) to obtain the normalized distributions. The lower end of the stellar mass range plotted corresponds to our completeness limit at $z = 1$.

$P_{\rm mem} > 0.5$ within a projected distance of $0.5R_{\rm 200c}$ of the center of groups in the mass completeness-limited bins of Figure 2.1. The radial cut on the group sample is to avoid contamination in the outskirts discussed in § 2.5.3. The plot includes both centrals and satellites; excluding centrals leaves the results essentially unchanged because the sample is dominated by satellites even in the highest stellar mass bin plotted. The fraction of red galaxies in this population is plotted against the mean stellar mass for each bin. We also plot the red fraction in individual groups for galaxies in the same stellar mass bins to show the variation between groups. At all redshifts, higher mass galaxies tend to have higher red fractions than lower mass galaxies. In addition to this stellar mass dependence, we see a clear separation between the group and field populations at all redshifts for the stellar masses probed. The field sample plotted matches the the redshift bins used for group members; matching the redshift distribution on finer scales results in quenched fractions that are at most a few percent different from those plotted.

We also see evidence for an increase in the red fraction with decreasing redshift among low mass group galaxies. Redshift trends are somewhat difficult to interpret because the range of group masses used is different in each redshift bin (see Figure 2.1) and the color cut does not account for evolution, so we leave a detailed analysis for future work. Because our galaxy sample is magnitude-limited, the low mass bins at high redshift are incomplete and plotted as open symbols. We make no corrections for incompleteness here, which likely leaves the sample in these bins biased toward the detection of blue galaxies that tend to have lower mass-to-light ratios than red galaxies, so we consider the red fractions in incomplete bins to be lower limits.

We detect a clear dependence of galaxy color on environment, even at fixed stellar mass and high redshift. Figure 2.10 uses the member catalog determined with photometric redshifts only, but including the available spectroscopic redshifts does not affect the results. Our results are similarly insensitive to the choice of a probability threshold for membership; changing the cut on $P_{\rm mem} > 0.5$ to 0.3 or 0.7 or weighting objects by $P_{\rm mem}$ instead of choosing a threshold moves the red fractions by no more than a few percent in any bin. Using the color cuts described in Bundy et al. (2010) to separate passive galaxies in COSMOS from dusty star-forming galaxies also gives qualitatively similar results. Though the absolute fraction of red galaxies measured depends on the specific cuts used, the relative trends with stellar mass and environment are similar; galaxy groups have a larger proportion of red galaxies than the field, and groups dominated by blue galaxies are rare, though some appear to exist.

We note that while our results confirm a significant relationship between color and environment out to the redshift limit of our sample, the cause of this relationship remains unknown. More detailed analysis distinguishing between physical processes happening before and after galaxies join groups is necessary to determine the role that groups play in this process.

We now compare Figure 2.10 to results from the literature. Our findings are consistent with results at low-redshift that show a decrease in star formation at high stellar masses, as well as a clear connection between star-formation and environment even after accounting for stellar mass differences (e.g., Kauffmann et al. 2004; Baldry et al. 2006). At $z \sim 0.4$,

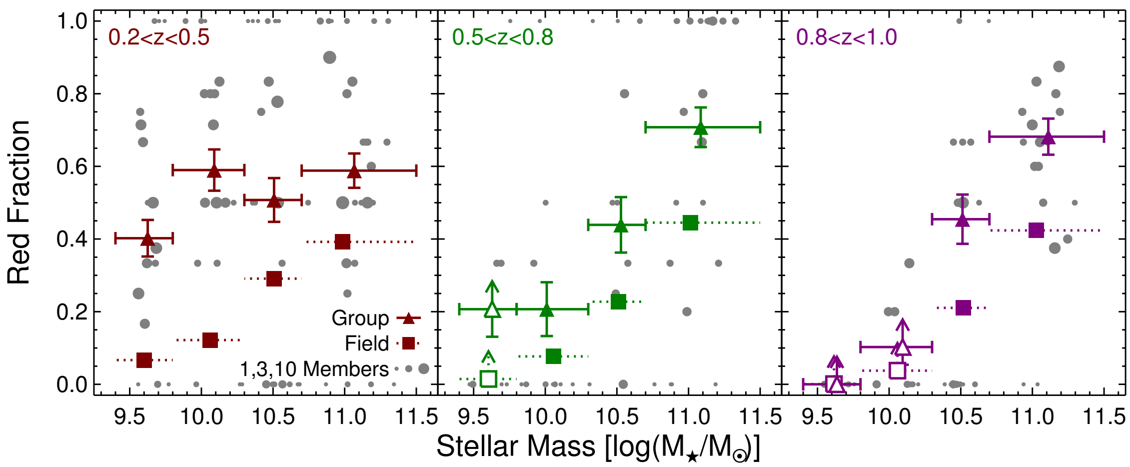

Figure 2.10: Fraction of quenched galaxies as a function of stellar mass in different redshift bins (separate panels). Triangles show the quenched fraction of members with $P_{\rm mem} > 0.5$ and projected group-centric distance within $0.5R_{\rm 200c}$ of groups in the mass bins from Figure 2.1. Squares show the quenched fraction of field galaxies with $P_{\rm mem} = 0$. Open symbols show bins with stellar mass incompleteness; the arrows above these symbols indicate that they are likely to be biased lower than the true values. Vertical error bars show the standard deviation of 1000 bootstrap samples and horizontal bars represent the stellar mass bin widths. Gray circles show the quenched fraction in a given stellar mass bin for individual groups, with size proportional to the number of members in the bin. Note that the range of halo masses for group members varies between redshift bins.

McGee et al. (2011) report an environmental trend in the GEEC survey that is smaller than a comparable low-redshift sample, but still significant. However, Poggianti et al. (2008) do not detect a significant separation in the fraction of star-forming galaxies in cluster and field environments at $z = 0.4 - 0.8$ after matching stellar mass distributions.

At the highest redshift range covered by our group sample, our findings are consistent with those of Cooper et al. (2010) and Peng et al. (2010) who detect a significant color-density relation in a similar stellar mass range covered by DEEP2 and zCOSMOS, respectively. These results appear to be at odds with some claims from VVDS and zCOSMOS analyses that such a relation could be attributed solely to the existence of more massive galaxies in dense environments (e.g., Scodeggio et al. 2009; Cucciati et al. 2010; Iovino et al. 2010). Each of these studies consider the environmental effect on color at fixed stellar mass, as we have done here. Cooper et al. (2010) emphasize that systematics in the selection of dense environments tend to wash out the measured signal of environmental dependence, so that if such correlations are seen they are likely to be real. They also suggest that the non-detection of environmental trends in other surveys is likely due to lower spectroscopic sampling rates and reliance on less confident redshifts which comprise a significant fraction of the sample at high redshift. The photometric redshifts used in the present work are certainly less precise than spectroscopic redshifts, but have a much higher sampling density.

An important distinction with this study is that we are using a unique sample of groups; X-ray detections ensure a robust sample of structures that are virialized, a trait which may not be true of optically-selected groups. The X-ray groups are also more massive than the typical spectroscopically-selected groups, and may have formed earlier giving them a longer time to suppress star formation in member galaxies. Other studies of this sample of X-ray groups also detect a significant environmental effect on galaxy colors (Giodini et al., in prep.; Tanaka et al., in prep.). Finoguenov et al. (2010) have shown that the number density of this X-ray group sample is in reasonable agreement with that expected for halos of corresponding masses within our cosmological model. The sample is therefore unlikely to be an extreme population of groups, though we cannot rule out subtle differences between X-ray-selected groups and the full population of groups in this mass range.

Because of differences in analysis methods, it is difficult to determine whether the qualitatively distinct findings in these environmental studies are also quantitatively inconsistent, or whether different results are simply due to measuring different quantities. We now consider aspects of the analysis methods and definitions of environments that may contribute to the differing results, focusing our attention to field studies at $z \sim 1$ where the results appear most discrepant. For instance, we have shown in Figure 2.8 that centroiding errors can influence the purity and completeness of a group sample, and our lensing tests (see Chapter 3) ensure a reliable determination of the center of mass. Additionally, we use only galaxies and groups in mass-complete bins, avoiding the need for volumetric corrections made in some of the previous analyses.

Our group-based definition of dense environments is most similar to that of Iovino et al. (2010), who studied optically selected groups which are less massive on average than the X-ray groups studied here. Figure 22 of Kovač et al. (2010) shows that these X-ray selected groups tend to be in more dense regions on average than the optically selected ones. The richest optical groups (with 4 or more members) show a good correspondence with X-ray groups in the density field and are more likely to have similar halo masses. Figure 12 of Iovino et al. (2010) shows that the colors of stellar mass-selected samples do not significantly depend on group richness (except perhaps at low stellar mass and redshift), so the difference in halo masses between X-ray and optical groups is not obviously the cause of discrepancy between our results and those of Iovino et al. (2010). Knobel et al. (2009) tested the purity of the optical group sample with mock catalogs and found a contamination fraction of roughly 25%, improving to about 15% for richer groups. These values are similar to our estimate of 16% contamination within $0.5R_{200c}$ for the sample used in our analysis, so the correct identification of group members is not a clear cause for the difference in results either.

Cucciati et al. (2010) quantify environment using the local galaxy overdensity $\delta = (\rho - \bar{\rho})/\bar{\rho}$, where ρ is the local density computed from the distance to the fifth nearest neighbor and $\bar{\rho}$ is the mean density at a given redshift. Their Figure 10 shows a red fraction that is roughly constant across quartiles of the local overdensity distribution for $z > 0.5$ and $\log(M_\star/M_\odot) > 10.85$, with a weak overdensity dependence at lower redshift. With the same data and density indicator, Peng et al. (2010) study the density field ρ instead of the overdensity field δ and show a significant color-density relation at $z \sim 0.5$ and state that it continues to at least $z = 1$. They attribute the difference in results to the fact that a lower fraction of galaxies at $z \sim 1$ live in regions with high δ, and so the highest overdensity quartile used in the analysis of Cucciati et al. (2010) is presumably too broad at $z \sim 1$ to isolate the small population of galaxies in regions dense enough to produce strong environmental effects. Cooper et al. (2010) use a third nearest neighbor density estimator on DEEP2 data and identify a difference in the distribution of colors between galaxies in the upper 10% and lower 50% of the density distribution, so perhaps a cut more stringent than the upper quartile of the density distribution is needed to detect environmental effects at $z \sim 1$. Referring again to Figure 22 of Kovač et al. (2010) however, we see that X-ray groups live in roughly the same range of overdensities as the upper quartile of δ used in the Cucciati et al. (2010) analysis ($\log(1+\delta) \gtrsim 1$). Thus the explanation from Peng et al. (2010) for the non-detection of environmental trends at $z \sim 1$ by Cucciati et al. (2010) is not obviously applicable since we see a clear environmental signal in this overdensity range.

The scale on which environment is defined also differs between these analyses. The fifth nearest neighbor estimator used by Cucciati et al. (2010) and Peng et al. (2010) and third nearest neighbor used by Cooper et al. (2010) measure environment on a scale that varies with density and is typically of order 1 Mpc. Scodeggio et al. (2009) measures a density field on a significantly larger scale of 8 Mpc, so correlations on the smaller scales of group halos may be washed out. The group sample in Figure 2.10 is restricted to $0.5R_{200c}$ but the environmental signal is not significantly different when all selected members out to R_{200c} are included, despite the higher contamination fraction. In either case, R_{200c} is typically about 500 kpc for these groups, so our sample is likely probing the environment on smaller scales than studies using the galaxy density field.

Differences in the colors used to identify galaxies as red or blue could also contribute to the contrasting results. The other studies discussed here typically use rest-frame $U - B$ or $B - I$ colors, sometimes with a mass or redshift dependent cut to account for varying populations. We use an extinction-corrected rest-frame $NUV - R$ color to account for unquenched galaxies that appear red due to dust. To test the effect of this correction, we have tried redefining the sample of red galaxies using the cuts $NUV - R > 3.5$ or $U - B > 1$ without any extinction correction. The red fraction increases due to the influence of dust redding, and the separation between group and field values at $z > 0.5$ is reduced by up to a factor of 2, but we still see a clear difference between the red fraction in group and field environments.

We have not identified an obvious single factor to explain why previous analyses did not detect an environmental effect on galaxy color, but suspect the cause to be a combination of factors mentioned above. To avoid confusion when discussing environmental effects and to properly detected these trends, it is clearly important to specify what is meant by "environment" and to measure it carefully.

2.7.2 Star Forming Galaxies and the SZ Power Spectrum

Recent high-resolution, ground-based experiments have probed the power spectrum of the CMB to unprecedented fine scales (e.g., $\ell \gtrsim 2000$; Lueker et al. 2010; Fowler et al. 2010; Shirokoff et al. 2010; Das et al. 2011), which are sensitive to a variety of secondary anisotropies, such as radio and submillimeter point sources, and the SZ effect from groups and clusters. It was found that the power due to the SZ effect was 50% or less than predictions of most of the models (Lueker et al. 2010; Dunkley et al. 2010), which could be indicative of our incomplete understanding of the properties of groups and clusters, especially the low mass ($< 10^{14} M_{\odot}$) systems at $z > 0.5$, as they are believed to contribute half of the SZ power at $\ell \approx 3000$ (e.g., Komatsu & Seljak 2002; Shaw et al. 2010; Trac et al. 2011). It is possible that the hot gas pressure profile of distant groups behaves differently from that of clusters or that cluster profiles deviate from expectations at large radii, although it was recently shown that local groups obey the "universal" pressure profile (Sun et al. 2011) and at least one nearby cluster obeys the profile out to R_{200c} after accounting for gas clumping (Simionescu et al. 2011). Another possibility is that star formation (SF) activity is elevated in high-z systems, and the contribution of unresolved SF galaxies in the submillimeter regime could fill in the SZ decrement at ~ 150 GHz, thus reducing the SZ power (e.g., Hall et al. 2010). Using the $z = 0.5 - 1.0$ COSMOS groups, we are in a good position to investigate the contamination due to SF galaxies in groups.

For each group, we cross-matched all candidate member galaxies with the MIPS 24 μm source catalog (Sanders et al. 2007; Le Floc'h et al. 2009), using a matching radius of $2''$. For the matched objects, we assumed a starburst SED (spanning from 3600Å to 1 cm) taken from Lagache et al. (2003), and compared the 24 μm to 148 GHz flux ratio. More specifically, we approximated the MIPS 24 μm band as a tophat spanning 20.8 to 26.1 μm, and we used 18 GHz as the bandwidth for the 148 GHz channel of the Atacama Cosmology Telescope (ACT). Given the mass of our groups, we estimated the SZ flux for our groups, following

Majumdar & Mohr (2004). We find that the sum of the fluxes from SF galaxies at 148 GHz is negligible (typically $\lesssim 0.3\%$) compared to the magnitude of the SZ effect from these groups.

We selected the SED from the set of templates of Lagache et al. (2003) that maximizes the 148 GHz to 24 μm flux ratio to set a conservative upper limit, but uncertainties in the spectral model could allow for a larger flux at millimeter wavelengths from these sources. Lee et al. (2010) compare stacked MIPS measurements at 24, 70, and 160 μm to empirical templates from Chary & Elbaz (2001); Dale & Helou (2002); Lagache et al. (2003) and theoretical models from Siebenmorgen & Krügel (2007). For the stacked MIPS fluxes of sources at $z = 0.5 - 1$, the best-fitting template from Lagache et al. (2003) tends to predict a flux at wavelengths longer than 300 μm that can be an order of magnitude lower than other models. Even accounting for these uncertainties in the spectral models, our upper limit to the contamination of star-forming galaxies to the SZ signal from our sample of groups is no more than a few percent.

Our group sample is limited to $z < 1$. Several studies have reported elevated SF activity in centers of clusters at $z \gtrsim 1.4$ (e.g., Hilton et al. 2010; Tran et al. 2010; Tanaka et al. 2010). It remains to be seen if the SF galaxies could be abundant enough at higher redshifts to make a significant impact on the SZ signal in such systems.

2.8 Summary and Conclusions

We have presented a catalog of member galaxies in X-ray selected groups in the COSMOS field, carefully taking into account photo-z errors and attempting to avoid biasing the sample with assumptions about the properties of galaxies which have not previously been well-constrained in this mass and redshift range. We have thoroughly characterized the quality of the selection algorithm using tests with mock catalogs and spectroscopic redshifts. In these tests we discovered contamination from galaxies in projection in the outskirts of groups, but selection in the central regions is relatively clean. We have also studied the prospects for applying this selection algorithm to future multi-wavelength data sets, estimating the purity and completeness of the member selection as a function of redshift and centering uncertainties.

Analyzing this sample of group members, we have shown that both stellar mass and environment play a role in determining galaxy colors at $z \sim 1$. We emphasize that there are many ways to smear out environmental correlations and that these factors must be properly controlled in order to detect environmental trends. The X-ray groups studied here provide a clean sample of dense environments for which we can determine halo masses and centers.

Following our finding of suppressed star formation in group environments at all redshifts sampled, we investigated the possibility that clustered dusty star-forming galaxies could reduce the detected power in the high-ℓ CMB power spectrum by filling in SZ decrements in groups, and found that the effect must be quite small in this group sample. In contrast with the results relating to the suppression of star formation in groups, we have identified several blue central galaxies, which warrant further study.

In Chapter 3, we will describe weak lensing tests used to optimize the centering by finding tracers that best locate the center of mass. Chapter 4 will analyze galaxy properties in groups with respect to the distance from these centers, providing constraints on models describing the evolution of galaxies in dense environments. With a carefully selected sample of member galaxies in groups with well-constrained masses and centers, we can hope to map the course by which galaxies transform.

Chapter 3

A Weak Lensing Study of Halo Centering

Locating the centers of dark matter halos is critical for understanding the mass profiles of halos as well as the formation and evolution of the massive galaxies that they host. The task is observationally challenging because we cannot observe halos directly, and tracers such as bright galaxies or X-ray emission from hot plasma are imperfect. In this chapter we quantify the consequences of miscentering on the weak lensing signal from a sample of 129 X-ray selected galaxy groups in the COSMOS field with redshifts $0 < z < 1$ and halo masses in the range $10^{13} - 10^{14}$ $M_{\odot}$. By measuring the stacked lensing signal around eight different candidate centers (such as the brightest member galaxy, the mean position of all member galaxies, or the X-ray centroid), we determine which candidates best trace the center of mass in halos. In this sample of groups, we find that massive galaxies near the X-ray centroids trace the center of mass to $\lesssim 75$ kpc, while the X-ray position and centroids based on the mean position of member galaxies have larger offsets primarily due to the statistical uncertainties in their positions (typically $\sim 50 - 150$ kpc). Approximately 30% of groups in our sample have ambiguous centers with multiple bright or massive galaxies, and some of these groups show disturbed mass profiles that are not well fit by standard models, suggesting that they are merging systems. We find that halo mass estimates from stacked weak lensing can be biased low by $5 - 30\%$ if inaccurate centers are used and the issue of miscentering is not addressed.

3.1 Introduction

Galaxy groups and clusters are important sites of galaxy evolution and the abundance of these massive objects provides a sensitive probe of the amplitude of matter fluctuations and other cosmological parameters. Analyses of these structures require some knowledge of the location of the centers of their gravitational potentials. Because the total mass distribution is dominated by dark matter and is not directly observable, halo centers are typically assumed to be traced by a massive galaxy or the density peak of radiating hot gas. Miscentering is a critical issue when estimating the masses of groups and clusters because it adds significant systematic uncertainties (e.g., Johnston et al. 2007a,c; Mandelbaum et al. 2010; Rozo et al.

2011), and also degrades constraints on the concentration of mass profiles (Mandelbaum et al. 2008). Velocity offsets between observational tracers and halo centers impact studies of satellite kinematics (Skibba et al. 2011; Wojtak et al. 2011) and redshift-space distortions (Hikage et al. 2012). On the other hand, offsets between observational tracers and the true halo centers can provide information about the dynamical state of these systems and about the properties of dark matter (Clowe et al. 2006; Massey et al. 2011).

Finding halo centers is challenging for a number of reasons. Galaxy formation models (as well as halo models for describing the multiplicity of galaxies within halos) typically place the brightest or most massive galaxy at the center of each halo. But the brightest galaxy in a cluster is not always the central galaxy (Skibba et al. 2011, and references therein). Groups and clusters form from mergers of halos where the most massive halo becomes the host halo with its central galaxy, and smaller halos become subhalos with satellite galaxies. Several analyses of data from group catalogs and field surveys have found that there is some intrinsic scatter in stellar mass and luminosity at fixed halo mass (Yang et al. 2009; More et al. 2009; Leauthaud et al. 2012a; Reddick et al. 2012), which implies that halos can end up with satellites that are intrinsically more massive or luminous than the central galaxy. Additionally, there are uncertainties in measuring any observable quantity such as stellar mass that can cause a satellite to be misidentified as the most massive central galaxy, and structure projected along the line of sight can confuse the identification of member galaxies. Another difficulty is that merging systems are dynamically unrelaxed, which can produce offsets between the central galaxy and the halo center or other tracers such as the X-ray center. The systematics introduced by picking centers that do not coincide with the "true" center of mass are important and need to be quantified.

Gravitational lensing is a powerful tool for finding the centers of mass of halos since it is sensitive to the total mass distribution along a line of sight. Mass maps can be constructed for individual systems with strong lensing or for massive clusters with weak lensing (e.g., Smith et al. 2005a; Oguri et al. 2010; Shan et al. 2010). Such studies often find reasonable agreement between the positions of bright massive galaxies, X-ray emission, and lensing mass peaks, with a handful of interesting examples that illustrate how dark matter peaks can be offset from hot gas in merging galaxy clusters (e.g., Clowe et al. 2004; Bradač et al. 2008).

In this thesis, however, we are concerned with a large statistical sample of groups with lower masses and higher redshifts, a regime of interest for many current and future weak lensing surveys. The typical signal-to-noise ratio for the weak lensing signal from individual groups is low, so we cannot identify their halo centers individually. By stacking the lensing signal from many groups, we determine the mean mass profile around a given center. We repeat this process for different candidate centers and compare the resulting profiles to find the best tracer of the center of mass. The center of a smooth halo can be identified as the position where the lensing signal is maximized on small scales. Other components such as a massive galaxy or subhalo that is offset from the halo center could produce an additional peak in the lensing signal, so we must account for that when modeling the signal.

We analyze a sample of 129 X-ray selected galaxy groups at redshifts $0 < z < 1$ from the COSMOS field (Scoville et al. 2007), described in George et al. (2011). With COSMOS data, we have X-ray luminosities and centroids for each group, with member galaxies identified using photometric redshifts derived from over thirty ultraviolet, optical, and infrared bands, and a subsample with spectroscopic redshifts. We use weak lensing measurements from high resolution *Hubble* imaging to study the accuracy with which tracers such as bright galaxies and X-ray emission identify the centers of dark matter halos.

This work is part of a series studying the galaxy content of X-ray groups. Chapter 2 (George et al. 2011) presented a catalog of group membership assignments from a Bayesian treatment of photometric redshifts, along with extensive tests of the selection algorithm using mock catalogs and subsamples with spectroscopic redshifts. Initial analyses of group members were used to demonstrate an environmental influence on galaxy colors out to $z = 1$. A previous weak lensing study of this group sample was used to constrain the mean relation between X-ray luminosity and halo mass (Leauthaud et al. 2010).

In this chapter we study the centers of groups in detail to optimize observational choices for centering, to study the impact of miscentering on measurements of halo properties, and to explore the effects of merging and substructure on lensing measurements. The outline of the chapter is as follows. Section 3.2 describes the data used in our analysis, including the X-ray group catalog, assignment of member galaxies, and lensing shape measurements. We define eight candidate group centers in Section 3.3, and describe our procedure for testing different choices of centers in Section 3.4. Section 3.5 presents the results of our analysis, and Sections 3.6 and 3.7 provide discussion and conclusions of our work.

We adopt a WMAP5 ΛCDM cosmology with $\Omega_{\rm m} = 0.258$, $\Omega_\Lambda = 0.742$, $H_0 = 72\ h_{72}$ km s^{-1} Mpc^{-1} (Dunkley et al. 2009) following the initial lensing analysis of these groups by Leauthaud et al. (2010). All distances are expressed in physical units with $h = 0.72$. X-ray luminosities are expressed in the 0.1-2.4 keV band, rest-frame. All magnitudes are given on the AB system. To approximate the virial radii of halos, we use $R_{\rm 200c}$ which is the radius within which the mean mass density equals 200 times the critical density of the Universe at the halo redshift, $\rho_{\rm c}(z)$. The corresponding mass enclosed within this radius is $M_{\rm 200c} = 200\rho_{\rm c}(4\pi/3)R^3_{\rm 200c}$. We also assume halos follow a Navarro-Frenk-White (NFW, Navarro et al. 1996) density profile, with a concentration parameter $c_{\rm 200c}$ and a scale radius $R_s = R_{\rm 200c}/c_{\rm 200c}$. We use the term “group” to denote a set of galaxies occupying a common halo, and the halo masses of these groups is in the range $10^{13} - 10^{14}$ M$_\odot$ as estimated with weak lensing (Leauthaud et al. 2010). We will generally refer to more massive structures as clusters following convention, but make no other physical distinction between groups and clusters.

3.2 Data

To study how the constituents of galaxy groups trace the centers of mass of dark matter halos, we use an X-ray selected sample of galaxy groups from the COSMOS field (Scoville et al. 2007). We refer the reader to Chapter 2 for details of the data and methods used to construct the group catalog as well as tests of its properties with simulations and spectroscopic data. In this section, we briefly describe aspects of the catalog that are relevant for centering including the assignment of member galaxies to groups. We also introduce the galaxy shear catalog used in our weak lensing analysis.

3.2.1 X-ray Group Catalog

Our sample of galaxy groups has been selected from an X-ray mosaic combining images from the *XMM-Newton* (Hasinger et al. 2007) and *Chandra* (Elvis et al. 2009) observatories following the procedure of Finoguenov et al. (2009, 2010). A wavelet filtering of the X-ray mosaic is used to distinguish extended structures on scales of $32''$ and $64''$ from contaminants on smaller scales like active galactic nuclei (AGN). Once extended X-ray sources are detected, a red sequence finder is employed on galaxies with a projected distance less than 0.5 Mpc from the centers to identify an optical counterpart and determine the redshift of the group, which is then refined with spectroscopic redshifts when available.

A quality flag (hereafter XFLAG) has been assigned to each group based on the reliability of the optical counterpart identification. We study groups with XFLAG=1 or 2, indicating a confident spectroscopic association, while higher values indicate uncertain counterparts which could be due to projection effects or photometry contaminated by bright foreground stars. Sources with XFLAG=1 also have clear X-ray centroids, with an uncertainty in each position coordinate, σ_X, equal to the wavelet scale of $32''$ divided by the signal-to-noise of the flux measurement, while sources with XFLAG=2 have less certain X-ray centroids for which we have $\sigma_X = 32''$ set by the wavelet scale of the flux measurement.

To ensure a clean sample of groups with robust membership assignment, we employ the additional quality cuts suggested in Chapter 2, excluding groups that are near field edges or have significantly masked areas, potentially merging groups identified as distinct X-ray sources but with significantly overlapping volumes, and poor groups with fewer than four members identified. After these quality cuts, we have 129 groups in our sample ranging from redshift $0 < z < 1$.

3.2.2 Galaxy Membership

To determine how well galaxies trace the matter distribution in groups, we must first identify the galaxies that reside in them. The COSMOS field has extensive imaging in over thirty ultraviolet, optical, and infrared bands (Capak et al. 2007b), enabling the determination of stellar masses (see Chapter 2 for details) and precise photometric redshifts (Ilbert et al. 2009, and Chapter 2 for further tests). In Chapter 2, we presented a catalog of member galaxies for these X-ray groups, selected according to their photometric redshifts and proximity to X-ray centroids. Briefly, a Bayesian membership probability, $P_{\rm mem}$, is assigned to each galaxy by comparing the photometric redshift probability distribution function to the expected redshift distribution of group and field galaxies near each group. From the list of members with $P_{\rm mem} = 1 - P_{\rm field} > 0.5$, the galaxy with the highest stellar mass within an NFW scale radius of the X-ray centroid (including the positional uncertainty, σ_X) is selected as the group center. We call this object the $\mathrm{MMGG_{scale}}$, for "most massive group galaxy within a scale radius". A final membership probability is assigned by repeating the selection process within a new cylinder re-centered on this galaxy.

We have extensively tested this selection algorithm using mock catalogs and with sub-samples of galaxies for which we have spectroscopic redshifts, and found it to be both pure and complete near group centers; within $0.5R_{200c}$ and down to our limiting selection magnitude (F814W=24.2), 84% of galaxies selected as group members truly belong in groups, and 92% of true group members are selected as such. In this chapter we use the member catalog derived from photometric redshifts, which has an average of 26 members per group. From that list, there are an average of 6 members per group with spectroscopic redshifts for calibration and determining group redshifts.

3.2.3 Weak Lensing Data

The galaxy shape measurements used for our weak lensing analysis are described in Leauthaud et al. (2007). These are derived from high-resolution imaging over 1.64 degrees^2 of the COSMOS field with the Advanced Camera for Surveys (ACS) on the *Hubble Space Telescope* (*HST*; Koekemoer et al. 2007) to a limiting magnitude of F814W=26.4. Variations in the point-spread function (PSF) with position and time are modeled following Rhodes et al. (2007), and galaxy shapes are derived using the RRG method (Rhodes et al. 2000). The PSF-corrected shapes are converted to estimators of shear, γ, using a shear susceptibility factor calculated from moments of the global distribution of shapes and a calibration factor determined from simulated images. Updates to the procedure and the shear catalog are described in detail elsewhere, in Leauthaud et al. (2012a). These improvements include a more detailed correction of charge transfer inefficiency from Massey et al. (2010), and an empirical derivation of the dispersion in shear measurements in bins of magnitude and detection significance. This estimate of the shear dispersion includes contributions from intrinsic shape noise and shape measurement uncertainties, and varies from $\sigma_\gamma \approx 0.25$ for bright galaxies to $\sigma_\gamma \approx 0.40$ for faint objects.

The stacked weak lensing signal is derived from the average tangential shear, $\gamma_t(R)$, of background source galaxies at a projected distance R from the center of each group. The shear is related to the excess surface mass density $\Delta\Sigma(R)$ (Miralda-Escude 1991)

$$\Delta\Sigma(R) \equiv \overline{\Sigma}(<R) - \overline{\Sigma}(R) = \gamma_t(R)\Sigma_{\mathrm{crit}}, \tag{3.1}$$

where $\overline{\Sigma}(<R)$ is the mean surface density within radius R and $\overline{\Sigma}(R)$ is the azimuthally averaged surface density at R. The critical surface density Σ_{crit} is a function of the angular diameter distances between the observer (O), lens (L), and source (S),

$$\Sigma_{\mathrm{crit}} = \frac{c^2}{4\pi G}\frac{D_{OS}}{D_{OL}D_{LS}}, \tag{3.2}$$

where c is the speed of light and G is the gravitational constant.

In order to compute $\Sigma_{\rm crit}$ from Equation (3.2), we need to know the distances to both the sources and lenses. The group catalog provides lens redshifts which come primarily from spectroscopic data including zCOSMOS (Lilly et al. 2009, and in prep.). For background sources, we use photometric redshifts from Ilbert et al. (2009). To avoid contamination due to uncertainties in photometric redshifts, we use only sources with $z_S - z_L > \max[0.1, \sigma_{\rm z}]$ where σ_z is the 68% uncertainty in the source redshift. We also exclude sources with a secondary peak in their redshift density function (i.e. $\textsc{zp}_2 \neq 0$ in the Ilbert et al. 2009 catalog) which have a significant fraction of catastrophic redshift errors. With these cuts, the source catalog contains $210,015$ galaxies with well-measured shapes and redshifts, providing a source density of 36 galaxies per arcmin^2.

To obtain a significant measurement of $\Delta\Sigma$, we must combine the signal from many lenses and background sources. The combined measurement is a weighted sum over pairs of lenses i and sources j,

$$\Delta\Sigma = \frac{\sum_i \sum_j \mathcal{W}_{ij} \gamma_{t,ij} \Sigma_{{\rm crit},ij}}{\sum_i \sum_j \mathcal{W}_{ij}} \tag{3.3}$$

where the weight $\mathcal{W}_{ij} = (\Sigma_{\rm crit} \sigma_{\gamma,ij})^{-2}$ is the inverse variance of the measurement. We measure $\Delta\Sigma$ in annular bins from 20 kpc to 1 Mpc. Covariance between measurements becomes an issue on larger scales where background sources can be paired with multiple lenses, but this is not significant over the scales we measure. Uncertainties in $\Delta\Sigma$ are determined from the inverse square root of the sum of the weights of lens-source pairs.

3.3 Defining Candidate Centers

The "center" of a galaxy group requires some definition. There is ambiguity in centering even when considering simulated dark matter halos; the mass centroid, most bound particle, and density peak can all be different because of asphericity and substructure. The choice of group and cluster centers in observational data sets is further limited by the available measurements. Here we review a variety of definitions of group centers and their relative advantages. Our aim is to use weak lensing to determine which candidates most accurately trace (on average) the centers of mass of dark matter halos. We will consider a variety of candidate centers and begin by studying the level of agreement between them. Our choice of candidate centers is meant to explore the range of options available for multi-wavelength data sets while using a simple set of rules for identification; however it is not an exhaustive list of possible centers.

It is useful to separate these definitions into two broad categories. We call the first set "galaxy candidates" since they are centered on a single galaxy, and the second set "centroid candidates" which are defined for a spatially extended quantity like the galaxy density field or X-ray emission and are in general not centered on an individual galaxy. Some centering algorithms take a hybrid approach, using the proximity of neighboring members to ultimately select a luminous galaxy (e.g., Robotham et al. 2011), but we do not test those methods here.

When identifying centers based on the galaxy content of groups, we select from galaxies with membership probability $P_{\mathrm{mem}} > 0.5$, as described in Section 3.2.2 and Chapter 2. Though the list of members is defined around one of the candidate centers (the $\mathrm{MMGG}_{\mathrm{scale}}$), the radius ($R_{200\mathrm{c}}$) used to select members is large enough that the initial choice of center should not impact our results. Each of the centers based on galaxy fluxes (e.g., brightest group galaxy) use the observed magnitude in the F814W band, taken with the ACS on *HST*, with no corrections for dust or evolution. Since these measurements do not account for the change in rest-frame wavelength probed, they will be more sensitive to recent star formation at higher redshifts. Centers based on galaxy masses use the full measured spectral energy distribution (SED) so these effects are diminished.

3.3.1 Galaxy Candidate Centers

Many clusters have a central dominant galaxy with an extended stellar envelope, often located near the density peak of hot intracluster gas as seen in X-rays and the peak of the matter density probed by lensing or kinematics (e.g., Lin & Mohr 2004, and references therein). This motivates the choice of a single galaxy to trace the centers of groups and clusters. The general picture is further supported by numerical simulations of dark matter halos and subhalos, and has been encapsulated in the halo model which successfully describes many aspects of large-scale structure including measurements of galaxy clustering and lensing (e.g., Cooray & Sheth 2002; Zehavi et al. 2005; Mandelbaum et al. 2006b; Leauthaud et al. 2012a).

Thus a popular choice when defining cluster centers in optical catalogs is the Brightest Cluster Galaxy (BCG; or BGG in groups), since the selection is relatively simple (e.g., Koester et al. 2007b; Hao et al. 2010). But the choice of filter and aperture used for the flux measurement has an impact on which galaxies are selected; differences in redshift, star formation history, and dust content affect the flux observed in a given band, so a single flux measurement cannot reflect the complicated physical processes occurring in group centers. Color cuts can be used to isolate a few of these effects (e.g., Gladders & Yee 2000), though they often come with assumptions about the properties of central galaxies. For example some group catalogs use the brightest red sequence galaxy to identify group centers, avoiding galaxies that are bright due to recent star formation in favor of massive galaxies with old stellar populations.

Stellar masses are a promising alternative to observed or rest-frame luminosities since they correlate more directly with the masses of halos in which galaxies reside. However, stellar mass estimates require more detailed measurements of the SEDs of galaxies and are fraught with larger uncertainties than simple fluxes or luminosities.

We consider four galaxy candidates, selected based on flux or stellar mass and distance to the X-ray position:

- $\mathrm{MMGG}_{\mathrm{scale}}$: the galaxy within $R_s + \sigma_{\mathrm{X}}$ of the X-ray centroid having the greatest stellar mass.

- $\text{MMGG}_{\text{R200}}$: the galaxy having the greatest stellar mass of all group members within R_{200c}.
- $\text{BGG}_{\text{scale}}$: the brightest galaxy within $R_s + \sigma_X$ of the X-ray centroid.
- BGG_{R200}: the brightest galaxy of all group members within R_{200c}.

The X-ray centroid (with uncertainty σ_X) is used as the starting point for selecting these galaxies because it should roughly trace the halo center and we do not have lensing centers for individual groups. Note that there is not necessarily a galaxy within the NFW scale radius R_s of the X-ray centroid, so $\text{MMGG}_{\text{scale}}$ and $\text{BGG}_{\text{scale}}$ are not necessarily defined for all galaxy groups. However, in the case of our clean sample, each group has at least one member within this radius so we do not have to deal with undefined centers. Uncertainties in the galaxy positions are much smaller than the sizes of the galaxies, and are therefore negligible compared to the offsets from halo centers that we are capable of measuring with weak lensing.

3.3.2 Centroid Candidate Centers

The central galaxy is not always observationally obvious, and selection of an incorrect galaxy can produce statistically undesirable results when studying a sample of groups or clusters. This problem has motivated the use of centroids based on the positions of some or all group members, which can be weighted by their properties such as flux or stellar mass, with the hope that a robust statistic can be less prone to large errors than the choice of a single galaxy (e.g., White et al. 1999; Carlberg et al. 2001; Berlind et al. 2006; Jee et al. 2011).

Additionally, other probes of groups and clusters such as X-ray and SZ (Sunyaev & Zeldovich 1972) observations of hot gas, and gravitational lensing can be used to find halo centers. Deep pointed observations can map the gas distribution in great detail for bright systems that are nearby or massive, but centering uncertainties can be significant for fainter systems (see Section 3.2.1). Similarly, only very massive systems produce a large enough lensing signal to study their spatial mass distribution individually, and lower mass systems (like the groups studied here) require stacking, such that centroids cannot be determined for each individual group from lensing alone.

Here we consider four centroid candidates:

- CN: the centroid of member galaxies.
- CM: the centroid of member galaxies weighted by stellar mass.
- CF: the centroid of member galaxies weighted by flux
- X-ray: the X-ray centroid.

Uncertainties on the X-ray positions were discussed in Section 3.2.1 and have a mean value of 22″ or 134 kpc. For the other centroid candidates (CN, CM, CF), the coordinates are computed using a weighted mean,

$$\mathbf{x}_{\rm cen} = \frac{\sum_{i=1}^{N} w_i \mathbf{x_i}}{\sum_{i=1}^{N} w_i}, \tag{3.4}$$

where $\mathbf{x_i}$ is the pair of coordinates $(\text{R.A., Dec.})_i$ for each galaxy i, N is the number of group members, and w_i is the appropriate galaxy weight for each center definition; $w_i = 1, M_{\star,i}, f_i$ for CN, CM, CF, respectively, where $M_{\star,i}$ is the stellar mass and $f_i \propto 10^{-0.4m_i}$ with f_i and m_i the flux and apparent F814W magnitude for each galaxy. We estimate the errors for these weighted means using bootstrap resampling from the list of member galaxies. With an average of 26 member galaxies per group, the mean statistical uncertainties on the projected galaxy centroid positions are $45, 52$, and 50 kpc for candidates CN, CM, and CF, respectively, where we have taken the geometric mean of the uncertainties in two dimensions and converted the angular uncertainty to a projected physical distance at the redshift of each group. Groups with a higher projected density of member galaxies tend to have smaller centroid uncertainties, but improvements appear to be limited by contamination in the outskirts from correlated structure (see Chapter 2 for tests of purity and completeness). We have tested different centroiding schemes including iterating until the centroid and member list converge or restricting to red galaxies, but achieved qualitatively similar results as with the centroids presented.

3.3.3 Offsets Between Candidate Centers

Our first test of these various centers is to see how well they agree with one another. Figure 3.1 shows the distribution over all groups of the angular and physical distance offsets between pairs of candidate centers, along with the distribution of uncertainties in centroid positions. Immediately we see that candidate centers do not always agree. For example, in 22% of groups the brightest galaxy within R_{200c} is not the most massive galaxy and the candidates are separated by up to several hundred kpc. The agreement level among pairs of galaxy candidates is typically $70-80\%$ with a long tail in the distribution extending out roughly to the virial radius for these groups. The galaxy candidates are typically offset from the centroid candidates by $50-100$ kpc, again with tails of a few hundred kpc, and the centroid candidates are in slightly better agreement among themselves. The offsets between the X-ray centroid and other candidate centers are generally consistent with the statistical uncertainties on the X-ray centroid. When comparing galaxy centroids (CN, CM, and CF) to other candidate centers, the typical offsets are roughly consistent with the mean uncertainty on the centroid position, but there are long tails in the offset distribution that exceed typical uncertainties.

These results are generally consistent with offsets found in other groups and cluster samples, though direct comparison is difficult given the variety of methods and data used for identifying objects and their centers. For $\sim 30\%$ of optically-selected groups in a similar mass range as our sample, Skibba et al. (2011) found that the brightest galaxy was not the central one, based on the relative positions and velocities of other member galaxies. This is comparable to the level of disagreement we find between our galaxy candidates, for which choosing a central galaxy is ambiguous. Comparing the positions of BCGs to X-ray centroids in 42 optically-selected clusters, Sheldon et al. (2001) noted a mean offset of 85 kpc. With an expanded sample of 94 clusters with matching X-ray detections, Koester et al. (2007a) found a very similar median BCG-X-ray offset of 81 kpc, and noted $\sim 20\%$ of systems with offsets of several hundred kpc which were mostly due to confusion in identifying the X-ray position or BCG. In a study of 65 massive clusters with higher quality X-ray data, Sanderson et al. (2009) found BCG-X-ray offsets of typically less than a few tens of kpc, with a few outliers that were merging systems. Our X-ray offsets are somewhat larger due to the statistical uncertainties in the centroid positions, with a mean (median) offset of 104 kpc (78 kpc) between the $\mathrm{MMGG}_{\mathrm{scale}}$ and X-ray centroid.

3.4 Weak Lensing Methodology

3.4.1 The Approach

Our stacked weak lensing approach to test candidate centers is sketched in Figure 3.2. The left column shows two separate galaxy groups (red ellipses) and their corresponding shear maps measured from the shapes of background galaxies (gray sticks). For each group, two candidate centers are defined (blue triangle and purple diamond), and the shear maps are stacked around these positions in the middle column. The rightmost panels show the resulting lensing signal $\Delta\Sigma$ as measured radially from the candidate center. We emphasize that the lensing signal for individual groups is noisy (signal-to-noise ~ 1; see Figure 1 of Leauthaud et al. 2010), so we cannot directly identify the centers of weak lensing maps for individual groups and must stack many groups; in this sense Figure 3.2 is exaggerated.

Qualitatively, the amplitude of the lensing signal is maximized when the lens position used for stacking coincides with the true center of mass in each system, and the signal is suppressed when the nominal position deviates from the true center of mass. The two curves agree at radii much larger than the typical centering offset. More formally, the lensing signal around miscentered halos was first studied in the context of satellite galaxies (Natarajan & Kneib 1997; Hudson et al. 1998; Guzik & Seljak 2002; Yang et al. 2003, 2006), and later applied to the problem of uncertain group centers (Johnston et al. 2007a,c).

Observationally, our aim is to find the candidate center that maximizes the lensing signal on small scales, indicating that it best traces the center of mass. Furthermore, we would like to model the signal to infer the underlying mass profile and the typical offsets between our tracers and the true center of mass in halos. Interpreting the signal is complicated by

Table 3.1: Model Parameters for $\Delta\Sigma(R)$

Parameter	Description	Centered	Offset	Full	Prior mean	Prior σ	Restrictions
$\log(M_{200c}/M_\odot)$	halo mass	free	free	free	13.5	0.8	-
c_{200c}	halo conc.	tied	tied	free	4.0	3.0	$1 < c_{200c} < 10$
$\sigma_{\rm off}$ (kpc)	offset dist. scale	fixed	free	free	0	200	$\sigma_{\rm off} > 0$
$\log(M_{\rm gal}/M_\odot)$	stellar mass	fixed	fixed	fixed	$\langle\log(M_{\star,\rm gal}/M_\odot)\rangle$	-	-
$\log(M_{\rm sub}/M_\odot)$	subhalo mass	omitted	omitted	free	$\langle\log(M_{\star,\rm gal}/M_\odot)\rangle$	1.0	$\log(M_{\rm sub}/M_\odot) > 10$

Note. — For each model, $M_{\star,\rm gal}$ is fixed to the mean photometrically-estimated stellar mass of the central galaxy (for galaxy candidates) and zero otherwise. For the centered and offset models, halo concentration is set by the relation of Zhao et al. (2009).

a number of effects including the shapes of halo profiles and the properties of galaxies and subhalos which will be discussed further in Section 3.6.

3.4.2 Models

To interpret the mean lensing signal $\Delta\Sigma$ defined in Equations (3.1) and (3.3), we construct a model for the surface mass density $\Sigma(R)$ of a typical lens. Contributions to $\Sigma(R)$ in our group sample come primarily from the dark matter halo and the central galaxy (if the center is defined to be at the position of a galaxy). The parameters of the model are introduced in Table 3.1. We include three variants of the model: a *centered* version where the halo center is fixed at the position of the candidate center, an *offset* model which allows a distribution of offsets between the candidate and true halo center, and the *full* model which adds freedom to the halo profile and allows for excess mass in the form of a subhalo around the candidate center.

We model the average mass density in halos with a spherical NFW profile, for which the projected surface density $\Sigma_{\rm halo}(R) = \Sigma_{\rm NFW}(R)$ is given in e.g. Wright & Brainerd (2000), with halo mass and concentration as two free parameters. For the centered and offset models we will assume a mass-concentration relation from Zhao et al. (2009), leaving mass as a single free parameter for the halo component, while both mass and concentration are free parameters in the full model.

When the surface density of a spherically symmetric halo is measured around the correct center of mass, we have $\overline{\Sigma}(R) = \Sigma_{\rm halo}(R)$. If there is an offset $R_{\rm off}$ in the lens plane between the true center and the position used for measurement, the surface density measured at the coordinates (R, θ) relative to the offset position is (Yang et al. 2003, Appendix B)

$$\Sigma^{\rm off}_{\rm halo}(R, \theta | R_{\rm off}) = \Sigma_{\rm halo}\left(\sqrt{R^2 + R^2_{\rm off} - 2RR_{\rm off}\cos\theta}\right). \tag{3.5}$$

The azimuthally-averaged surface density around the offset position is

$$\overline{\Sigma}^{\rm off}_{\rm halo}(R|R_{\rm off}) = \frac{1}{2\pi}\int_0^{2\pi} {\rm d}\theta\, \Sigma^{\rm off}_{\rm halo}(R, \theta|R_{\rm off}). \tag{3.6}$$

For an ensemble of halos with a distribution of offsets $P(R_{\rm off})$, Johnston et al. (2007a,c) generalized Equation (3.6) to give the mean azimuthally-averaged surface mass profile stacked around the offset positions

$$\overline{\Sigma}^{\rm off}_{\rm halo}(R|P(R_{\rm off})) = \int_0^\infty P(R_{\rm off})\,\overline{\Sigma}^{\rm off}_{\rm halo}(R|R_{\rm off})\,{\rm d}R_{\rm off}. \tag{3.7}$$

The mean surface density inside a radius R is

$$\begin{aligned}\overline{\Sigma}^{\rm off}_{\rm halo}(< R|P(R_{\rm off})) &= \frac{1}{\pi R^2}\int_0^R\int_0^{2\pi}\int_0^\infty P(R_{\rm off})\,\Sigma^{\rm off}_{\rm halo}(R',\theta|R_{\rm off}) \\ &\qquad\qquad\times\; R'{\rm d}R'{\rm d}\theta{\rm d}R_{\rm off} \\ &= \frac{2}{R^2}\int_0^R \overline{\Sigma}^{\rm off}_{\rm halo}(R'|P(R_{\rm off}))\,R'{\rm d}R'.\end{aligned} \tag{3.8}$$

To model the lensing signal from a large sample of galaxy clusters centered around BCGs, Johnston et al. (2007c) used a distribution of offsets $P(R_{\rm off})$ estimated from mock catalogs. In their model a fraction of BCGs correctly identified the centers of halos ($R_{\rm off} = 0$), while the remaining clusters had a distribution of offsets given by

$$P(R_{\rm off}) = \frac{R_{\rm off}}{\sigma_{\rm off}}\exp\left(-\frac{R^2_{\rm off}}{2\sigma^2_{\rm off}}\right). \tag{3.9}$$

This model, called a two-dimensional Gaussian or a Rayleigh distribution, was chosen based on mock catalogs to which their cluster-finding algorithm had been applied. The mocks suggested that the fraction of correctly-centered clusters depended on richness, with higher richness clusters more likely to be centered correctly. In other clusters, the central galaxy was not correctly identified as the BCG, and the distribution of offsets between the BCG and true halo center could be described by Equation (3.9) with the parameter $\sigma_{\rm off} = 420\ h^{-1}$ kpc describing the typical offset scale, independent of cluster richness.

We can think of the offset more generally in three dimensions, where we assume the offset in each dimension is normally distributed with mean zero. The observed offset in the line-of-sight dimension might not have the same variance as the dimensions in the lens plane because of redshift-space distortions, but as long as the distribution in three dimensions is joint-normal and the variance in the two dimensions of the lens plane is equal, the projected offset distribution will take the form of Equation (3.9) after marginalizing over the line of sight.

The miscentering component employed by Johnston et al. (2007c) added two free parameters to their model: the fraction of miscentered groups, and the scale length of the offset distribution. These additional parameters could not be well-constrained by the data, and had to be constrained using strong priors from mock catalogs.

Our approach is to use an offset model with a single free parameter to constrain the scale of the miscentering distribution empirically. We do not include separate components for centered and miscentered groups as Johnston et al. (2007c) did, as the single parameter model generally provides sufficient fits to the current data. Also, correctly chosen central galaxies may still be offset from their halo centers, an effect that was not included in the mocks of Johnston et al. (2007c) but has been tentatively seen in lensing maps of individual clusters (Oguri et al. 2010).

The second component of the model is the surface density contributed by the central galaxy, $\Sigma_{\rm gal}(R)$. The shape of this mass profile is uncertain, but its contribution is subdominant even at the smallest radii that we probe ($R \sim 50$ kpc). For the centered and offset models, we simply model the galaxy component as a point source, $\Sigma_{\rm gal}(R) = M_{\rm gal}/(\pi R^2)$, with $M_{\rm gal}$ fixed to the average stellar mass $M_{\star,{\rm gal}}$ of the central galaxies in the ensemble as estimated from their SEDs. The centroid candidates (CN, CM, CF, and X-ray) typically do not have a galaxy very near the center, so we do not include a contribution from $\Sigma_{\rm gal}$ when modeling the signal from these candidates.

We can write the centered and offset models as the sum of the halo and galaxy components:

$$\Delta\Sigma^{\rm cen}(R) = \Delta\Sigma_{\rm NFW}(R) + \Delta\Sigma_{\rm gal}(R) \tag{3.10}$$

$$\Delta\Sigma^{\rm off}(R) = \Delta\Sigma^{\rm off}_{\rm NFW}(R|P(R_{\rm off})) + \Delta\Sigma_{\rm gal}(R). \tag{3.11}$$

Note that $\Delta\Sigma^{\rm cen}(R) = \Delta\Sigma^{\rm off}(R|R_{\rm off} = 0)$. We later test a scenario with the full model in which the candidate center has an additional mass component in the form of a dark matter subhalo that is more extended than the stellar profile which will be described further in Section 3.5.3.

Though the measured signal is an ensemble average coming from halos with a range of masses and mass profiles, our model consists of a single profile for simplicity and because the range of halo masses inferred from group X-ray luminosities is relatively small. We restrict our analysis of the lensing signal to $R < 1$ Mpc, where the effects of halo truncation and correlated structure should be unimportant to the lensing signal, and note that this adequately covers the range of centering offsets shown in Figure 3.1. At small scales, the assumption of weak shear becomes less accurate. Mandelbaum et al. (2006a) derive a correction term to the surface density contrast that depends on $\Sigma_{\rm crit}$ and $\Sigma(R)$ for the sample. These correction factors have been computed for this sample by Leauthaud et al. (2010) and shown to be fairly small on the scales we probe (of order 10% of the measured signal in our innermost bin for a good center), so we do not include them in our analysis.

To fit the models to the data, we attempt to find the parameters that minimize

$$\chi^2 = \sum_i \frac{(\Delta\Sigma_{\rm data}(R_i) - \Delta\Sigma_{\rm model}(R_i))^2}{\sigma_i^2} \tag{3.12}$$

where σ_i is the measurement uncertainty on $\Delta\Sigma_{\rm data}(R_i)$. In practice, we use a Markov Chain Monte Carlo (MCMC) approach to efficiently explore the multi-dimensional parameter space maximizing the logarithm of the likelihood, $L \propto \exp(-\chi^2/2)$. We employ Gaussian or lognormal priors for each parameter, with means and standard deviations given in Table 3.1.

The data are unable to constrain a lower limit to the subhalo mass or an upper limit to the concentration, so we restrict these parameters to $\log(M_{\rm sub}/M_{\odot}) > 10$ and $c_{200c} < 10$ when they are free. We also require $c_{200c} > 1$ and $\sigma_{\rm off} > 0$.

3.5 Results

3.5.1 Weak Lensing on the Full Sample

Given that Figure 3.1 shows a wide range of offsets between different choices of group centers, we proceed to test how well the candidate centers trace the underlying matter distribution. We begin by studying the full sample of groups in this section, and in the next section we focus on the subset of groups with significant offsets between candidates.

For each center candidate, we measure the lensing signal $\Delta\Sigma(R)$ from all groups in annular bins around the center. The results are shown for the eight candidate centers in Figure 3.3. Each panel represents a different candidate center from Section 3.3, for which we plot the measured $\Delta\Sigma(R)$ (black points) along with models $\Delta\Sigma^{\rm cen}(R)$ (thick blue) and $\Delta\Sigma^{\rm off}(R)$ (thin magenta). For illustration, we show the halo and galaxy components of the models for MMGG$_{\rm scale}$: $\Delta\Sigma_{\rm NFW}(R)$ (green dashed), $\Delta\Sigma^{\rm off}_{\rm NFW}(R|R_{\rm off})$ (orange dot-dashed), and $\Delta\Sigma_{\rm gal}(R)$ (red dotted).

The mean and standard deviation (1σ) of the posterior distribution for each parameter, along with the mean central galaxy masses and χ^2 values for the fits, are shown in Table 3.2. The χ^2 values have not been normalized by the number of degrees of freedom ν. Each model is fit to 6 data points with 1 and 2 free parameters for the centered and offset models, respectively, so $\nu = 5$ for the centered model and $\nu = 4$ for the offset model. When $\chi^2 \approx \nu$, the model is consistent with the data given the uncertainties. A high value of χ^2 indicates that the model does not fit the data; for example, the data are inconsistent with the model at a 95% confidence level when $\chi^2 \geq 11.07$ (9.49) for $\nu = 5$ (4).

There are clear differences among the lensing signals for the eight candidate centers. The signal generally rises toward small scales for the galaxy candidates, while there is a turnover for the centroid candidates indicating that they are poorer at tracing the center of mass in these groups. The stellar mass in the candidate central galaxies produces some of the difference in the signal, but the best-fit models show that the galaxy candidates have smaller offsets from the halo centers when compared with the centroid candidates even when accounting for the stellar mass. We will explore the possibility of additional mass in the central galaxy candidates in Section 3.5.3. It is important to note that the offsets measured from the lensing signals for the X-ray position and other centroid candidates are primarily due to the large statistical uncertainties in the centroid positions, shown in Figure 3.1. Figure 3.3 shows the impact of these centroid uncertainties on the lensing signal, but we cannot infer from this data that there are significant intrinsic offsets between the true centroid positions and the center of the dark matter halo.

For each of the galaxy candidates, the χ^2 value in Table 3.2 indicates that the centered

Table 3.2: Parameters Constraints for $\Delta\Sigma(R)$

Candidate	$\langle\log(M_\star/M_\odot)\rangle$	Centered Model $\log(M_{200c}/M_\odot)$	c_{200c}	χ^2	Offset Model $\log(M_{200c}/M_\odot)$	c_{200c}	$\sigma_{\rm off}$ (kpc)	χ^2
Galaxy candidates								
$\mathrm{MMGG_{scale}}$	11.3	13.43 ± 0.07	4.0	4.2	13.45 ± 0.07	3.9	18.2 ± 11.3	4.2
$\mathrm{MMGG_{R200}}$	11.4	13.43 ± 0.06	4.0	5.3	13.47 ± 0.07	3.9	28.3 ± 15.2	4.4
$\mathrm{BGG_{scale}}$	11.2	13.40 ± 0.06	4.0	2.9	13.43 ± 0.07	4.0	16.8 ± 10.0	2.8
$\mathrm{BGG_{R200}}$	11.3	13.42 ± 0.07	4.0	4.4	13.45 ± 0.06	3.9	24.8 ± 12.0	3.0
Centroid candidates								
CN	-	13.35 ± 0.07	4.0	21.0	13.51 ± 0.07	3.9	65.0 ± 18.0	2.8
CM	-	13.39 ± 0.07	4.0	10.5	13.45 ± 0.08	3.9	34.5 ± 21.6	9.3
CF	-	13.38 ± 0.07	4.0	14.0	13.51 ± 0.09	3.9	66.9 ± 29.9	9.5
X-ray	-	13.30 ± 0.08	4.1	15.2	13.42 ± 0.08	4.0	57.1 ± 16.9	3.5

Note. — For both models, $M_\star$ is fixed to the stellar mass of the central galaxy (for galaxy candidates) and zero otherwise, and the halo concentration is fixed by the relation of Zhao et al. (2009). The number of degrees of freedom, ν, is 5 for the centered model and 4 for the offset model.

model provides a good description of the data given the error bars. The extra degree of freedom in the offset model does not significantly improve the fit, and the constraints on $\sigma_{\rm off}$ are consistent with zero at the 2σ level. The best-fit values for $\sigma_{\rm off}$ and the quality of the fits are statistically consistent for each of the galaxy candidates, so we do not strongly favor one candidate over another, though there is marginal evidence that the candidates defined within an NFW scale radius of the X-ray position ($\mathrm{MMGG_{scale}}$ and $\mathrm{BGG_{scale}}$) trace the halo center slightly better than candidates defined over the larger area within R_{200c}.

On the other hand, the centered model generally does not provide good fits to the data for the centroid candidates, and the offset models do improve the fits. The best-fit offset parameter $\sigma_{\rm off}$ is significantly larger for the centroid candidates than for the galaxy candidates and deviates from zero by more than 2σ for three of the centroid candidates. The offset model fits two centroid candidates (CM and CF) only marginally well so these would perhaps be better fit by a more complicated offset distribution.

The effect of miscentering on the halo mass constraints is comparable to the statistical uncertainty for this sample. The best-fit halo masses assuming a centered model for the centroid candidates tend to be $\sim 1\sigma$ lower than for galaxy candidates. Halo masses increase slightly when offsets are allowed in the model, and candidates with larger offsets are more affected. When miscentering is not accounted for in the model, halo masses are underestimated by $5 - 30\%$ compared to when we include the effect, depending on the choice of center.

We have also tested the effect of fixing the concentration parameter with our assumed mass-concentration relation, and freeing this parameter does not qualitatively change the results. We do not obtain a good constraint on the concentration, but the best-fit value for the galaxy candidates is consistent with our assumed value. The centroid candidates prefer somewhat lower concentrations, but the values are still consistent within the large error bars.

3.5.2 Groups with Discrepant Candidate Centers

While the stacked lensing signal for the full sample of groups shown in Figure 3.3 exposes differences between candidate centers, Figure 3.1 shows that the candidate centers are identical in many groups. In order to more directly compare different centering schemes, we now select only the groups in which candidate centers disagree by a measurable amount. Figures 3.4 and 3.5 present this analysis, with each row showing the lensing signal centered on the $\mathrm{MMGG_{scale}}$ (left column) and a different candidate (middle column) for the subset of groups where the two candidate centers are separated by more than 50 kpc. The rightmost column shows the histogram of offsets between the two centers repeating Figure 3.1 on logarithmic axes. The number of groups and the mean redshift of each subset are shown at the top right. We have chosen the $\mathrm{MMGG_{scale}}$ as a fiducial center here since Table 3.2 suggests that it is among the best candidates, but using the $\mathrm{BGG_{scale}}$ gives a consistent picture.

In each row of the figure, we first model the lensing signal in the lefthand panel assuming that the $\mathrm{MMGG_{scale}}$ correctly traces the halo center, fitting for the halo mass with concentration fixed. Next, we take that best-fit centered model and convolve it with the distribution of offsets in the righthand panel to model the signal in the middle panel. This is equivalent to replacing the offset distribution of Equation (3.9) with the empirical distribution of offsets between two candidates, leaving no free parameters for the models shown in the middle panels. We again add a central point mass fixed to the mean photometric stellar mass of the candidate galaxies for each of the galaxy centers. Though we expect that galaxies offset from the halo center have subhalos, the lensing data are currently insufficient to constrain such an additional contribution. The halo mass is fitted using only the lensing data centered on the $\mathrm{MMGG_{scale}}$, so the level of agreement between the offset model and the data in the middle panel can be read as a consistency test.

Looking first at the comparisons between the $\mathrm{MMGG_{scale}}$ and the centroid candidates in Figure 3.4, we see that the lensing signal is reasonably well-described with an NFW halo centered on the $\mathrm{MMGG_{scale}}$, with a mean halo mass consistent with that measured for the full sample in Table 3.2. Additionally, the offset model gives a decent representation of the lensing signal measured around the centroid candidates shown in the middle panels. We interpret these results as indicating that centroid candidates do not trace halo centers as well as galaxy candidates.

In the samples where the $\mathrm{MMGG_{scale}}$ disagrees with other galaxy candidates (Figure 3.5), the lensing signal is different than in the centroid comparison. The best-fit halo masses are significantly lower than in the full sample measured earlier. The lensing signals are noisier, in part because of the smaller sample sizes, and one case deviates significantly from the offset model. Though it appears that the $\mathrm{BGG_{scale}}$ produces a higher lensing signal than the $\mathrm{MMGG_{scale}}$ at small radii in this direct comparison, that profile is not well-fit by a centered NFW model and the fitted mass is similarly low.

Figure 3.6 shows how two samples of groups with differing galaxy candidates are distributed in redshift and X-ray luminosity relative to the full sample of groups. Cases where the most massive group member lies in the outskirts ($\mathrm{MMGG_{scale}} \neq \mathrm{MMGG_{R200}}$) appear to be evenly distributed throughout the sample. Groups where the brightest galaxy near the X-ray position is not the most massive ($\mathrm{MMGG_{scale}} \neq \mathrm{BGG_{scale}}$) tend to be at higher redshifts, which can also be seen in the mean redshifts for the samples in Figure 3.5. This illustrates how an observed-frame selection of BCGs, like that used for $\mathrm{BGG_{scale}}$ here, tends to pick up bluer star-forming galaxies at higher redshifts.

The low masses shown in Figure 3.5 could be attributed to statistical fluctuations with the small sample size ($24-40$ groups, as compared with $91-98$ groups in Figure 3.4). To test this idea, we performed jackknife tests using randomly selected samples of the same number of groups without replacement. In each of 1000 random samples we measured the lensing signal around $\mathrm{MMGG_{scale}}$ and fit a model with a central point mass equal to the average stellar mass and a centered NFW with halo mass as a free parameter and concentration fixed. Of the 1000 random samples of 24 groups, 19% had a best-fit halo mass lower than that found for the sample of 24 groups where $\mathrm{MMGG_{scale}} \neq \mathrm{MMGG_{R200}}$. In samples of 25 groups, none had a lower best-fit halo mass than $\log(M_{200c}/M_{\odot}) = 12.57$, the value found for the sample with $\mathrm{MMGG_{scale}} \neq \mathrm{BGG_{scale}}$. And in samples of 40 groups, only 1% had a best-fit mass lower than the sample where $\mathrm{MMGG_{scale}} \neq \mathrm{BGG_{R200}}$. For a given X-ray luminosity, groups with discrepant galaxy candidate centers appear to have lower masses than the rest of the sample and in some cases more disturbed mass profiles.

Figure 3.6 shows a redshift dependence in the fraction of groups where the brightest galaxy (measured from the observer-frame F814W flux) does not have the highest stellar mass. High redshift groups may have more disturbed lensing profiles for different reasons than having ambiguous galaxy center candidates, so we have repeated the jackknife tests restricting to groups at $z > 0.7$. Even among high redshift systems, the groups with a brighter galaxy than $\mathrm{MMGG_{scale}}$ are outliers; less than 1% of random samples of groups produce a best-fit mass lower than the samples where $\mathrm{MMGG_{scale}} \neq \mathrm{BGG_{scale}}$ or $\mathrm{MMGG_{scale}} \neq \mathrm{BGG_{R200}}$, while just 17% of random samples are fit by lower masses than the groups with $\mathrm{MMGG_{scale}} \neq \mathrm{MMGG_{R200}}$.

Visual inspections of the groups with discrepant galaxy candidates have not revealed obvious differences from the rest of the sample. Given the noisy lensing signal measured around such groups, one might worry that they are not real associations but chance projections. However, these groups are not preferentially found near the X-ray flux limit shown in Figure 3.6 and they do not have unusually low numbers of member galaxies associated with them, so they are unlikely to be impurities in the group sample.

Groups with multiple massive galaxies and disturbed density profiles are likely to have merged recently, a point we discuss further in Section 3.6.

3.5.3 Model Uncertainties

Having established that the lensing data can be used to constrain the choice of a tracer for the centers of mass of halos, we would like to know how well a given candidate actually traces halo centers. In this section we explore a more general model to see how certain assumptions, namely the mass-concentration relation and the form of the central mass component, affect our results.

The results shown in the previous section suggest that galaxy candidates trace the halo centers better than centroid candidates, because the stacked lensing signal on small scales is greater when centered on a galaxy. While the model used to fit the signal for galaxy candidates includes a component to account for the stellar mass that exists in galaxy candidates but not in centroid candidates, it is plausible that we have underestimated the amount of mass in the central galaxies, either in stars and baryons or in a dark matter subhalo. In a typical halo model the central galaxy has no subhalo, so in the latter scenario the galaxy candidate could actually be a satellite or the system may be unrelaxed. Detailed modeling of strong and weak lensing observations of individual clusters has found evidence for subhalos around member galaxies even near cluster centers (Natarajan et al. 2007, 2009). Additional mass in the central term $\Sigma_{\rm gal}(R)$ could hide significant offsets between the galaxy candidates and host halos, effectively filling in the decrement at small radii in the halo term $\Sigma_{\rm halo}(R)$.

To address this degeneracy, we apply our full model with an additional mass component around the galaxy candidate, in addition to the point source representing the stellar mass. We use the functional form of a truncated non-singular isothermal sphere (Pastor Mira et al. 2011)

$$\rho(r) = \frac{\rho_0}{(1 + r^2/r_{\rm core}^2)(1 + r^2/r_{\rm cut}^2)}. \tag{3.13}$$

We fix the core radius $r_{\rm core} = 0.1$ kpc and set the truncation radius $r_{\rm cut}$ to the distance at which the local mass densities of the subhalo and halo components are equal, as measured along the line connecting their centers assuming an offset distance $\sigma_{\rm off}$. To facilitate comparisons with the stellar mass, we cast the normalization of the model in terms of a free parameter $M_{\rm sub}$ (instead of ρ_0) which we will refer to as the subhalo mass, defined as the mass enclosed within 5 kpc, the mean half-light radius for our sample. Since the core radius is much smaller than our innermost lensing measurement, the exact value chosen does not influence our results. The choice of truncation radius and functional form of the subhalo mass profile does affect the mass normalization, but the qualitative shapes of the parameter degeneracies are consistent for a variety of truncation schemes and for mass profiles that are isothermal, or nearly so, across the inner few tens of kpc. However if the subhalo component is not truncated at all, or if it is modeled instead as an NFW profile as Pastor Mira et al. find in simulations with subhalos, its mass can become degenerate with the full halo mass.

For a given lensing signal, a larger halo concentration can also compensate for some miscentering effects, so we free the $c_{\rm 200c}$ parameter to study the degeneracy with $\sigma_{\rm off}$ without the restrictions of the model for concentration used before. In practice, concentration is not well-constrained by this data set, so a prior is still needed to restrict the range of values when fitting.

An additional model uncertainty comes from the form of the distribution of offsets $P(R_{\rm off})$ that is used. The offsets between galaxy candidates in Figure 3.1 appear to support the models used by Johnston et al. (2007c) and Oguri et al. (2010), with a significant fraction of agreement between candidates along with a wide tail in the distribution. To avoid the need for additional free parameters describing both well-centered and miscentered populations in the offset distribution, we attempt to select a clean sample of groups and constrain the scale of offsets between the candidate galaxy center and the halo center assuming the single distribution given in Equation (3.9). We test this model on the sample of groups for which the four galaxy candidates agree, i.e. where the brightest and most massive group members are one and the same, and where this galaxy lies within an NFW scale radius of the X-ray centroid. There are 85 groups with such unambiguous galaxy centers.

The lensing signal for these groups stacked around the galaxy candidate is shown in Figure 3.7. To summarize our model, we fit the signal with an NFW halo and a truncated isothermal subhalo of the form in Equation (3.13) in addition to a point mass fixed by the photometric stellar mass. The point mass is fixed at the center of the subhalo, which is allowed to be offset from the center of the halo. This leaves four free parameters: the halo mass M_{200c} and concentration c_{200c}, the offset scale $\sigma_{\rm off}$ between the galaxy and halo, and the subhalo mass normalization $M_{\rm sub}$.

Figure 3.8 shows the results of the MCMC analysis exploring this parameter space. Each panel with blue contours shows the 68% and 95% regions of the joint posterior probabilities for a pair of parameters, marginalizing over the other parameters. The top panel in each column shows for each parameter the arbitrarily normalized prior from Table 3.1 (dashed green curves) and the one-dimensional posterior probabilities (black histograms) while marginalizing over the other parameters. Note that the data are unable to constrain a lower limit on the subhalo mass or an upper limit to the concentration, so the posterior distributions are sensitive to our priors in those regions.

The data are consistent with a model in which there are no subhalos around the candidate central galaxies, though a value comparable to the average stellar mass of the galaxies is preferred, and significantly more massive subhalos are ruled out. We emphasize the stellar mass is already included in the model as a point source, so the subhalo component represents mass in excess of the stellar mass that was estimated from the photometry. Recall that the $M_{\rm sub}$ is defined as the subhalo mass within the typical half-light radius of 5 kpc; integration of Equation (3.13) out to large radii for the maximum likelihood parameters gives a *total* subhalo mass of roughly five times the observed stellar mass component. The truncation radius for this model is 21 kpc. The preference for a nonzero subhalo mass may simply indicate that the photometric stellar mass is underestimated[1], or that the point source model for the stellar term is insufficient. A subset of correctly-centered groups (or an excess at small scales in the offset distribution relative to the model) could also explain the signal which we have fitted as a subhalo component. The halo mass is well-constrained and consistent with the values measured for the full group sample with the simpler model in Section 3.5.1. The data prefer a higher value of c_{200c} than the Zhao et al. (2009) prediction for this halo mass and redshift, but the concentration is not well-constrained. For the offset distribution,

[1]Stellar masses used in this work have been derived assuming a Chabrier (2003) initial mass function (IMF). Recent suggestions of a steeper subsolar IMF for early type galaxies could explain this discrepancy (e.g., Auger et al. 2010; van Dokkum & Conroy 2010).

the data are consistent with no offsets between the central galaxy candidates and the halo centers, though a value of roughly 50 kpc is preferred. Large offsets ($\sigma \gtrsim 100$ kpc) are ruled out for an offset model of a single two-dimensional gaussian distribution, though individual outliers may exist. On average, massive galaxies trace halo centers quite well.

There are degeneracies between the offset distance scale and the subhalo mass as well as the halo concentration. If the subhalo mass within 5 kpc is smaller than $\sim 10^{11} M_{\odot}$, the offset scale must be smaller than 50 kpc, but for larger subhalo masses the offset scale can reach 100 kpc. A constraint on the total mass enclosed within small scales, perhaps from strong lensing or measurements of stellar velocity dispersions for the central galaxies, could improve constraints on $\sigma_{\rm off}$. Similarly, $c_{\rm 200c}$ and $\sigma_{\rm off}$ are correlated, with higher concentrations corresponding to larger offsets. Thus when modeling a given lensing signal, if miscentering is not taken into account it can lead to an underestimate of the concentration.

3.6 Discussion

Finding the centers of mass for dark matter halos presents both an observational challenge and an opportunity to study the interplay between halos and central galaxies. We have presented a method to test different tracers of group and cluster centers by comparing the weak lensing signal stacked around their positions. Our approach can in principle be applied to any analysis that would be affected by miscentering. For instance, centering algorithms can also be tested using satellite kinematics by identifying the candidate that is nearest to the dynamical center when averaging over the ensemble. The spatial clustering of galaxies can also provide centering information; in practice the peaks in the galaxy density field are generally used in defining optical cluster catalogs, but clustering data could also be used to optimize the determination of their centers. Additionally, these approaches to optimizing the centers of a halo catalog can be fed back into algorithms used to find halos and their centers, allowing a more probabilistic approach to deal with cases where centering is uncertain.

With X-ray detected galaxy groups in the COSMOS field, we find that individual bright and massive galaxies trace the centers of halos better than the nominal X-ray centroid or the mean position of group members, even when weighted by luminosity or stellar mass. Offsets between the X-ray centroids and candidate central galaxies are primarily due to the large uncertainties in the X-ray positions, which can reach roughly 200 kpc. Centroids based on the mean positions of galaxies also have significant uncertainties, though some offsets exceed the estimated errors. More stringent constraints on intrinsic offsets between centroid candidates and halo centers could be obtained with deeper, high-resolution X-ray or SZ data, or with a sample of massive clusters and more member galaxies.

For each pair of galaxy candidates defined in Section 3.3, roughly $20-30\%$ of groups have ambiguous centers. Either the most massive galaxy lies far from the X-ray position, or the brightest galaxy is not the most massive. Only two-thirds (85 out of 129) of the groups show complete agreement between all four galaxy candidates, which underlines the importance of testing any choice of center in a group or cluster catalog.

The results of Figure 3.5 and the jackknife tests described in Section 3.5.2 suggest that groups with ambiguous galaxy centers have low masses for their X-ray luminosities or disturbed halo mass profiles. A connection between centering offsets and the dynamical state of halos has been seen in observational studies (e.g., Forman & Jones 1982; Katayama et al. 2003; Sanderson et al. 2009) and simulations (e.g., Cohn & White 2005; Poole et al. 2006; Macciò et al. 2007; Neto et al. 2007; Skibba & Macciò 2011). The ability to identify unusual or unrelaxed groups and clusters with a simple observable such as having different candidate centers could prove useful when trying to select a clean sample of relaxed systems. Further studies connecting lensing measurements with member galaxy properties such as the distribution of colors may provide a clearer picture of the impact of halo mergers on galaxies and star formation. Similarly, a more general analysis of the gaps in stellar mass or luminosity and the spatial separation between massive member galaxies would complement the restricted set of center candidates studied here.

There are several reasons why candidate centers can be offset from halo centers. Interlopers or incompleteness in the group member sample can result in the wrong galaxies being selected. Satellite galaxies can be more massive or luminous than centrals due to scatter in the relation linking the observable property to the mass of a halo or subhalo. In Chapter 2, we presented tests of our group membership and centering algorithm on mock catalogs designed to reflect the real uncertainties in X-ray positions and photometric redshifts. In that analysis, 77% of central galaxies were correctly identified as the $\mathrm{MMGG}_{\mathrm{scale}}$. The most common failure mode was the selection of satellites as $\mathrm{MMGG}_{\mathrm{scale}}$ because they had higher stellar masses than the true centrals, which happened in 12% of cases. The frequency of this occurrence depends on the way we populate halos with mock galaxies following the stellar mass-halo mass relation of Leauthaud et al. (2012a), but we note that scatter in this relation is consistent with that found in other analyses (Yang et al. 2009; More et al. 2009; Reddick et al. 2012). The remaining centering failures were evenly split between cases where X-ray errors misplaced the search region and photometric redshift errors scattered centrals out of their groups.

Observational uncertainties, such as scatter in stellar mass estimates (~ 0.2 dex) and catastrophic errors in photometric redshifts (for $\lesssim$ a few percent of objects in our COSMOS sample), add to this scatter and increase the chances that a satellite is incorrectly identified as the central galaxy. Furthermore, merging activity is not modeled in the mocks catalogs, so these effects together can account for the $\sim 30\%$ of observed groups where galaxy candidates disagree. The offsets seen between centroid candidates (CN, CM, CF, and X-ray) are consistent with being due primarily to the large observational uncertainties in their positions.

The offsets measured here are significantly smaller than the distribution measured from mock catalogs by Johnston et al. (2007c). This could be due in part to our choice of offset model; in Sections 3.5.1 and 3.5.3 we assumed a single Rayleigh distribution of offsets, whereas Johnston et al. separated groups that were correctly centered from those that were miscentered. Our aim in Section 3.5.1 was simply to estimate a typical offset scale for comparing candidate centers, and in Section 3.5.3 we selected a sample where centering seemed unambiguous to study up close the offsets of massive galaxies which could be sloshing around halo centers. The offsets found in Section 3.5.3 are comparable to the smaller component of the offset distribution measured by Oguri et al. (2010). While they are fairly small, modeling degeneracies with the subhalo mass and halo concentration increase their uncertainty. Future analyses of halo properties may benefit from including a range of models for the distribution of offsets, if the data can constrain a larger number of parameters.

Another important difference between our analysis and that of Johnston et al. is that the maxBCG clusters are detected as optical galaxy overdensities, whereas the COSMOS groups studied here are detected in X-ray emission, which traces the dense regions near the centers of halos, offering a better starting point for finding the centers of halos. When comparing the effects of miscentering for different cluster catalogs, it is also worth noting that more massive clusters are larger, so offsets of a given distance can be more easily detected than in less massive systems.

Further investigations with simulations could improve our understanding of some issues with centering (e.g., Macciò et al. 2007; Neto et al. 2007; Hilbert & White 2010; Behroozi et al. 2011; Dietrich et al. 2012; Power et al. 2012). There is a similar ambiguity when defining the center of a simulated dark matter halo, since there can be offsets between the position of the most bound particle, the mass density peak, and the centroid of mass with a given smoothing scale. Offsets between these positions in simulations have been shown to correlate with the dynamical state of a halo, with larger offsets seen in less relaxed halos that have experienced a recent merger. Projecting the matter density in simulated halos to compare with the observed lensing signals could help explain the poor fits to NFW profiles and unusually low masses we obtain from samples with ambiguous centers. Similarly, a better understanding of the form and evolution of halo and subhalo mass profiles, due to effects like gas cooling or heating and tidal stripping, could improve our modeling.

Finally, we consider the implications of miscentering for cosmological analyses. The abundance of massive halos is sensitive to the amplitude of matter fluctuations and the growth history of the Universe, and the precise determination of group and cluster masses is a critical aspect of this probe. Mandelbaum et al. (2010) have studied the effects of miscentering on mass estimates for massive halos using simulated data and analytical profiles, assuming the distribution of offsets from the mock catalogs of Johnston et al. (2007c). For clusters at the upper end of our mass range ($\sim 10^{14}$ $M_{\odot}$), they find that the weak lensing mass is underestimated by $25 - 30\%$ if miscentering is ignored, and that this effect is stronger for less massive halos (see their Figure 3). They also show that the accuracy of mass estimates depends on the assumed concentration as well as the inner and outer radius measured, and suggest excising the inner regions from the analysis because of these uncertainties. In a separate study, Mandelbaum et al. (2008) measured the mass-concentration relation for several samples of galaxies and clusters, including the maxBCG sample. Miscentering of clusters is also a concern for measuring concentrations, producing values that are biased low if the effect is ignored. Mandelbaum et al. (2008) argued that the miscentering distribution from Johnston et al. (2007c) may be overestimated, based on the concentrations they derived from lensing and by comparison with the distribution of offsets between BCGs and X-ray peaks in a subsample of clusters (Koester et al. 2007a). Still, they had to trade off statistical power by excluding data at small radii to reduce systematic uncertainties from modeling the distribution of offsets.

We have endeavored to improve the accuracy of finding halo centers and to provide constraints on the distribution of offsets between observational tracers and underlying mass centers. With more accurate centers (and uncertainties on those positions), we can more reliably use data at small radii and improve statistical constraints from group and cluster surveys. Table 3.2 suggests that the halo mass inferred from the lensing signal stacked around our galaxy candidates is affected at the $5 - 10\%$ level if miscentering is ignored. This is significantly smaller than the bias seen by Mandelbaum et al. (2010) despite the trend that masses are increasingly underestimated for lower mass halos. We attribute the difference to the smaller offsets seen in this sample compared to the miscentering distribution used by Johnston et al. (2007c) where a fraction of groups had a distribution of offsets with $\sigma_{\rm off} = 420h^{-1}$ kpc. However, we also use a different model for the offset distribution and can see in Table 3.2 that the masses estimated from centroid candidates are more biased $(15 - 30\%)$ when miscentering is not addressed in the model. The statistical uncertainties on our halo mass estimates are still comparable to the centering bias, and with this sample we are currently unable to put a significant constraint on the halo concentration. But with larger group and cluster samples, our approaches to optimizing the choice of halo centers and modeling the distribution of offsets will enable better constraints on halo mass profiles for both astrophysical and cosmological applications.

3.7 Summary and Conclusions

We summarize the main results of this work as follows:

1. In our data set, different definitions of group centers do not always agree and occasionally show large offsets from one another. Candidate centers based on the locations of the brightest or most massive galaxy differ in 20-30% of cases with a wide range of offsets. Centroids based on the mean position of member galaxies or X-ray flux have offsets from other center definitions that are roughly consistent with their larger statistical uncertainties ($\sim 50 - 150$ kpc).

2. The offsets between centers produce a measurable signal in the lensing profile. Stacking the signal around a bright or massive galaxy tends to produce a larger signal at small scales than any centroid not located on a galaxy, and the difference in these signals is greater than expected from the stellar mass of the galaxy.

3. Among the candidate centers we have tested, the brightest or the most massive galaxy near the X-ray centroid appear to be the best tracers of the center of mass of halos. Centering definitions based on the centroid of member galaxies have larger offsets and uncertainties.

4. Groups that have ambiguous centers because of multiple bright or massive galaxies have lensing signals that suggest a lower mass than expected given their X-ray luminosity and in some cases appear disturbed. These are possibly merging systems, and the property of having discrepant candidate centers gives a simple observational indicator to identify them.

5. In groups with a clear central galaxy, offsets between the galaxy and the halo center are fairly small ($\lesssim$ 75 kpc). The offset is somewhat degenerate with the amount of substructure around the galaxy and with the concentration of the group halo.

These findings apply to our group sample but our approach can readily be applied to other group and cluster data sets, and to different analyses such as satellite dynamics and richness-based mass estimators. Given the level of disagreement among our candidate centers, we advise testing different centers to determine the degree to which centering choices affect a given analysis. Our finding that groups with ambiguous centers are less massive for their X-ray luminosity or have disturbed mass profiles suggests that these groups could be identified and excluded if an analysis calls for a clean sample of halos. Additionally, a probabilistic approach to centering algorithms could provide information about the confidence in a given center allowing for appropriate weighting of different systems.

Much larger samples of groups and clusters are being constructed with ongoing and upcoming surveys such as the South Pole Telescope and Atacama Cosmology Telescope, the Dark Energy Survey, and eROSITA. This initial study with a modestly-sized sample of groups benefits from high-resolution X-ray selection which provides a good starting point for finding centers, but a similar approach can be applied to optical or SZ-selected catalogs. With larger samples, we can hope to improve constraints on the density profiles of dark matter halos including their concentration and inner slope, as well as the mass distribution in subhalos and the effects of mergers. Additional constraints on the mass distribution from strong lensing or stellar kinematics can provide interesting constraints on a range of scales and improve models for the distribution of offsets between galaxies and halo centers.

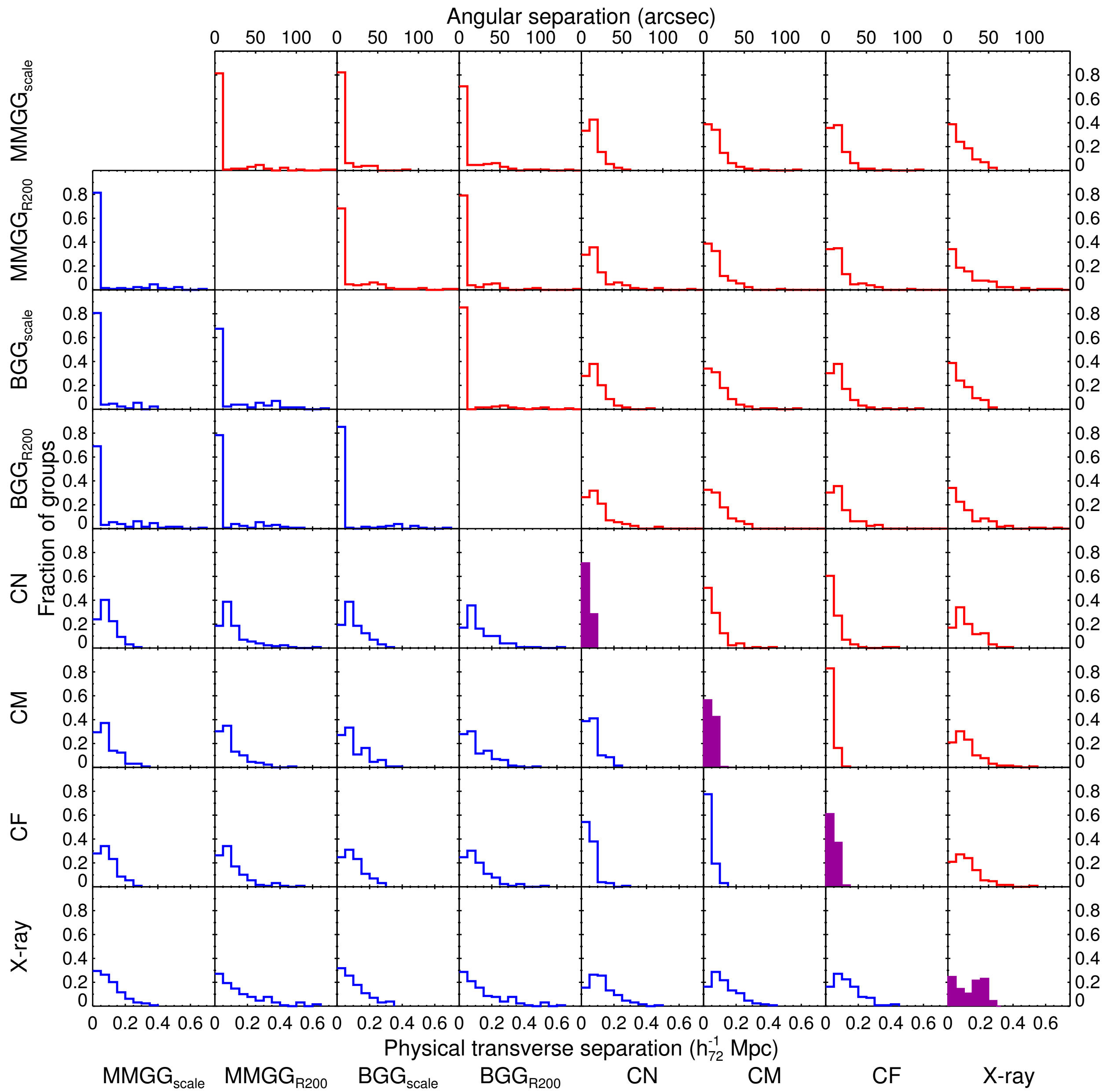

Figure 3.1: Distribution of projected offsets between pairs of candidate centers in our group sample, measured in arcseconds (upper right; red) and Mpc(lower left; blue). The angular and physical offset distributions are not identical because the groups span a range of redshifts. The filled purple histograms on the diagonal panels show the distribution of statistical uncertainties for each centroid position, described in Section 3.2.1 for the X-ray centroid and Section 3.3.1 for the others. The y-axis gives the fraction of groups in each bin; bin sizes are 50 Mpc (bottom left and diagonal) and 10″(upper right).

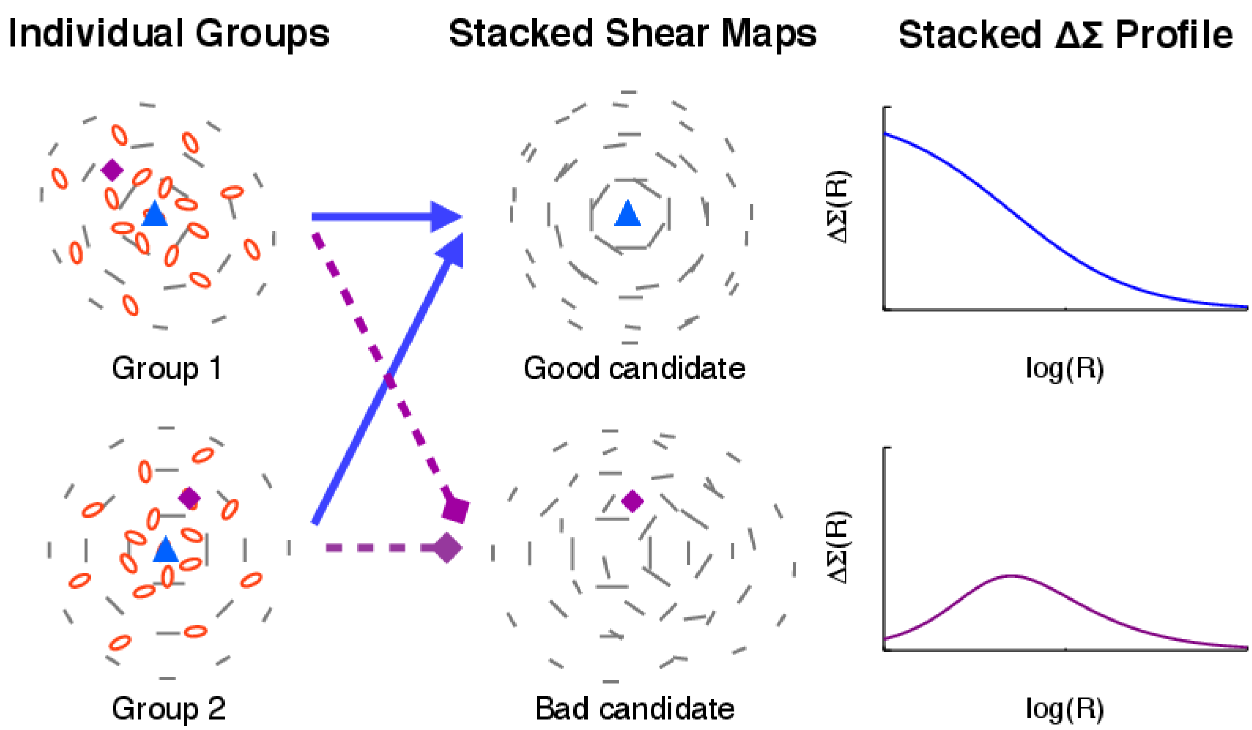

Figure 3.2: Schematic illustration of stacked lensing around different candidate centers. Candidate centers are defined in each group (left), then shear maps are stacked around each position (middle), and azimuthally averaged to compute $\Delta\Sigma$ profiles (right).

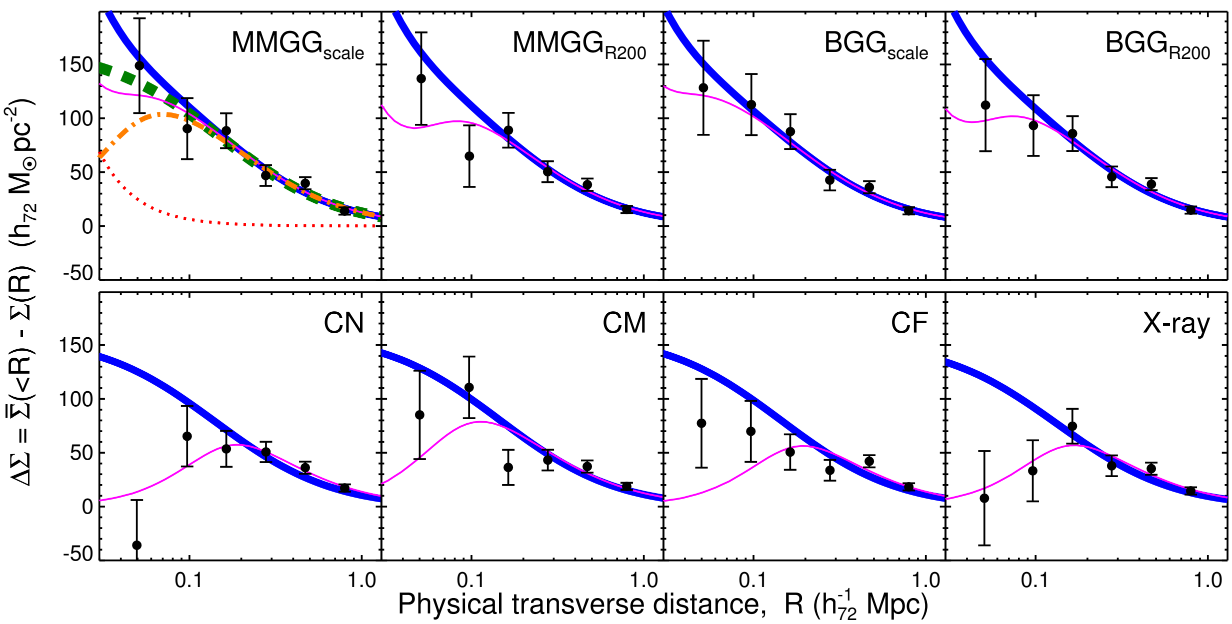

Figure 3.3: Weak lensing signal stacked on the full sample of groups around different centers, along with centered (thick blue, $\Delta\Sigma^{\rm cen}$) and offset (thin magenta, $\Delta\Sigma^{\rm off}$) models. Halo and central components of these models are shown for $\rm MMGG_{scale}$ (green dashed for $\Delta\Sigma^{\rm cen}_{\rm NFW}$, orange dot-dashed for $\Delta\Sigma^{\rm off}_{\rm NFW}$, red dotted for $\Delta\Sigma_{\rm gal}$). The top row shows the signal around galaxy candidates, while the bottom row shows centroid candidates. The signal (black points) is measured in radial bins with the first spanning $20-70$ kpc for sufficient signal-to-noise, then logarithmically spaced from 70 kpc to 1 Mpc.

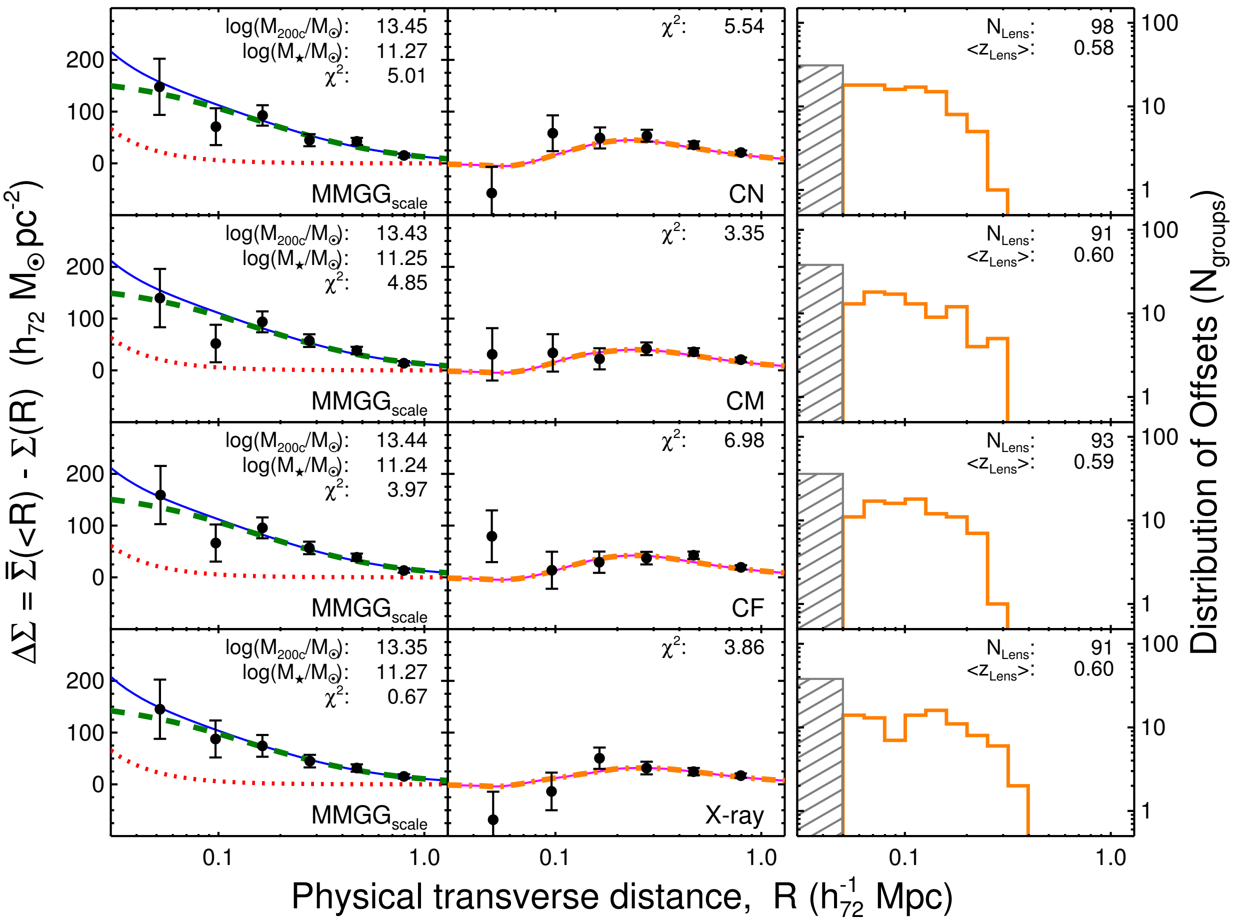

Figure 3.4: Lensing signal for subsets of groups where *centroid candidates* are offset from $\mathrm{MMGG_{scale}}$ by > 50 kpc. The left column shows the signal stacked around $\mathrm{MMGG_{scale}}$, the middle column shows the signal stacked around an alternate candidate, and the right column shows the projected distribution of offsets between the two candidate positions. Models are discussed in the text with line styles and colors as in Figure 3.3 and fit parameters stated within the left column. The number of groups with large offsets used in each row is stated in the right column, and the gray hashed boxes indicate the number of groups excluded from this analysis because the two candidates agree to within 50 kpc.

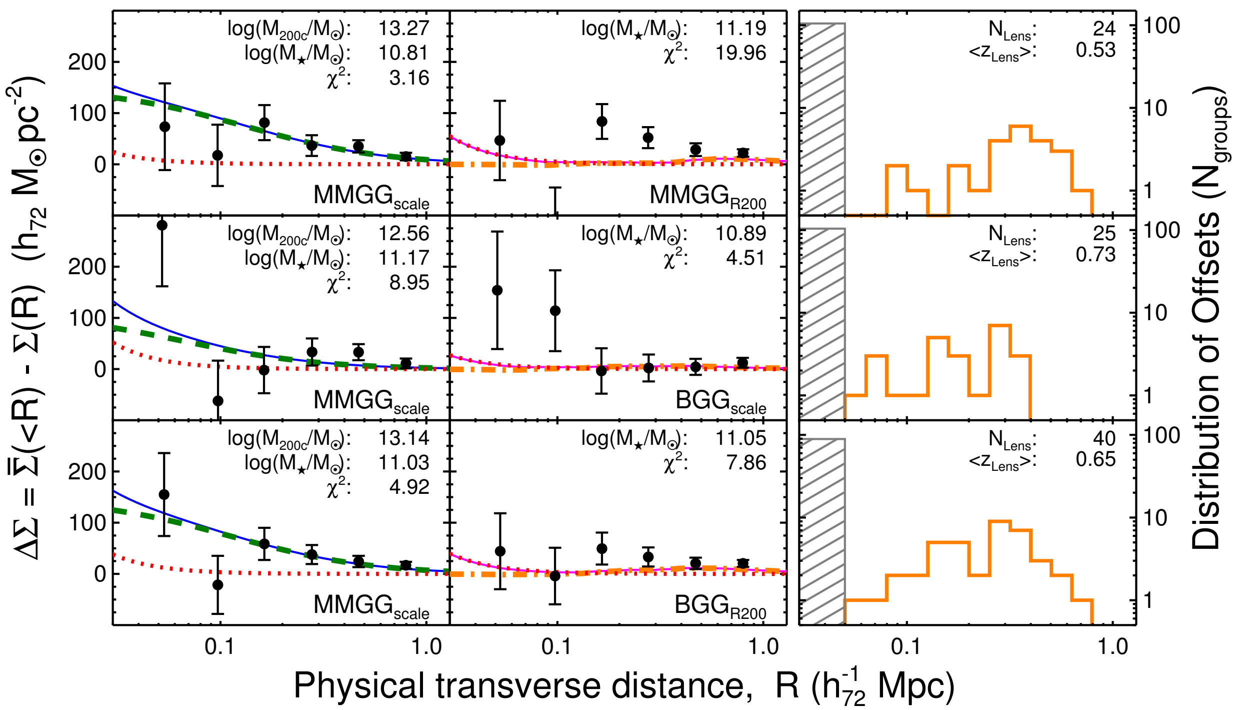

Figure 3.5: Lensing signal for subsets of groups where *galaxy candidates* are offset from $\mathrm{MMGG_{scale}}$ by > 50 kpc. Plot columns and style are the same as in Figure 3.4.

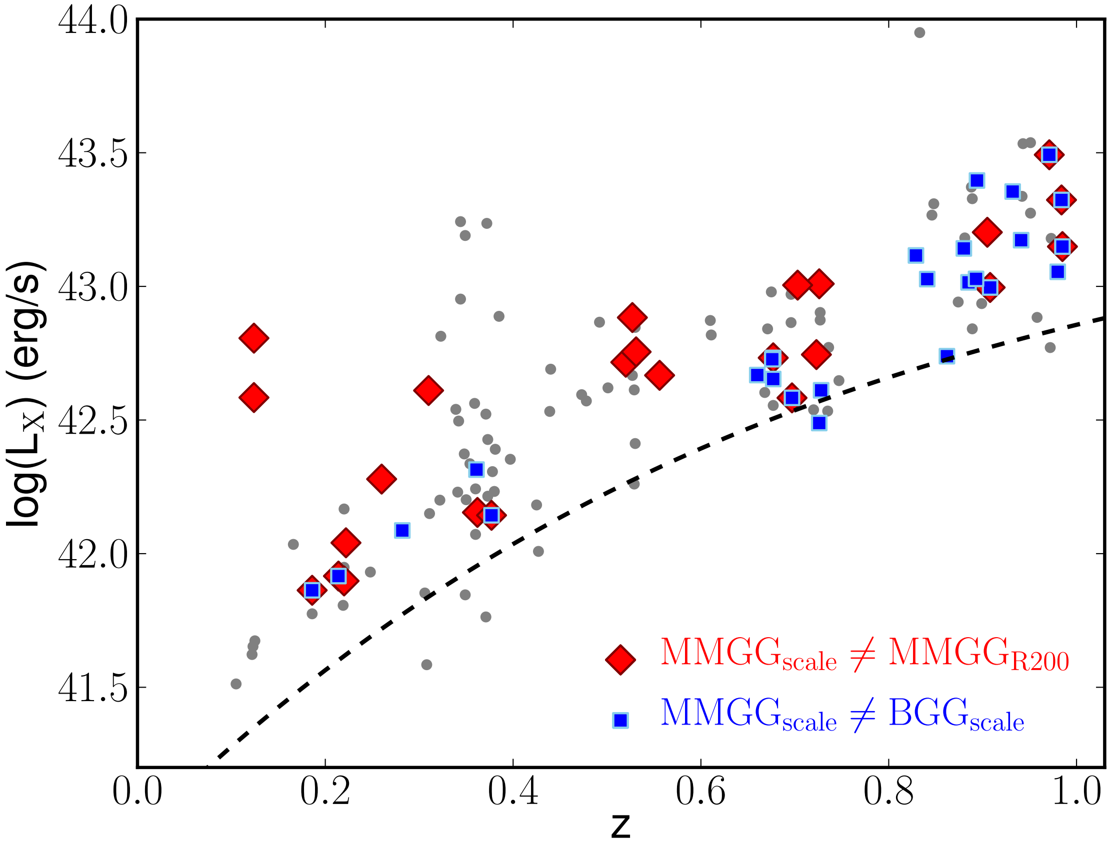

Figure 3.6: Distribution of redshifts and X-ray luminosities for the group sample. Cases where different galaxy candidates disagree are identified according to the legend. The dashed curve shows the 4σ X-ray flux limit of 1.0×10^{-15} ergcm^{-2}s^{-1} reached in 96% of the field converted to a limiting luminosity.

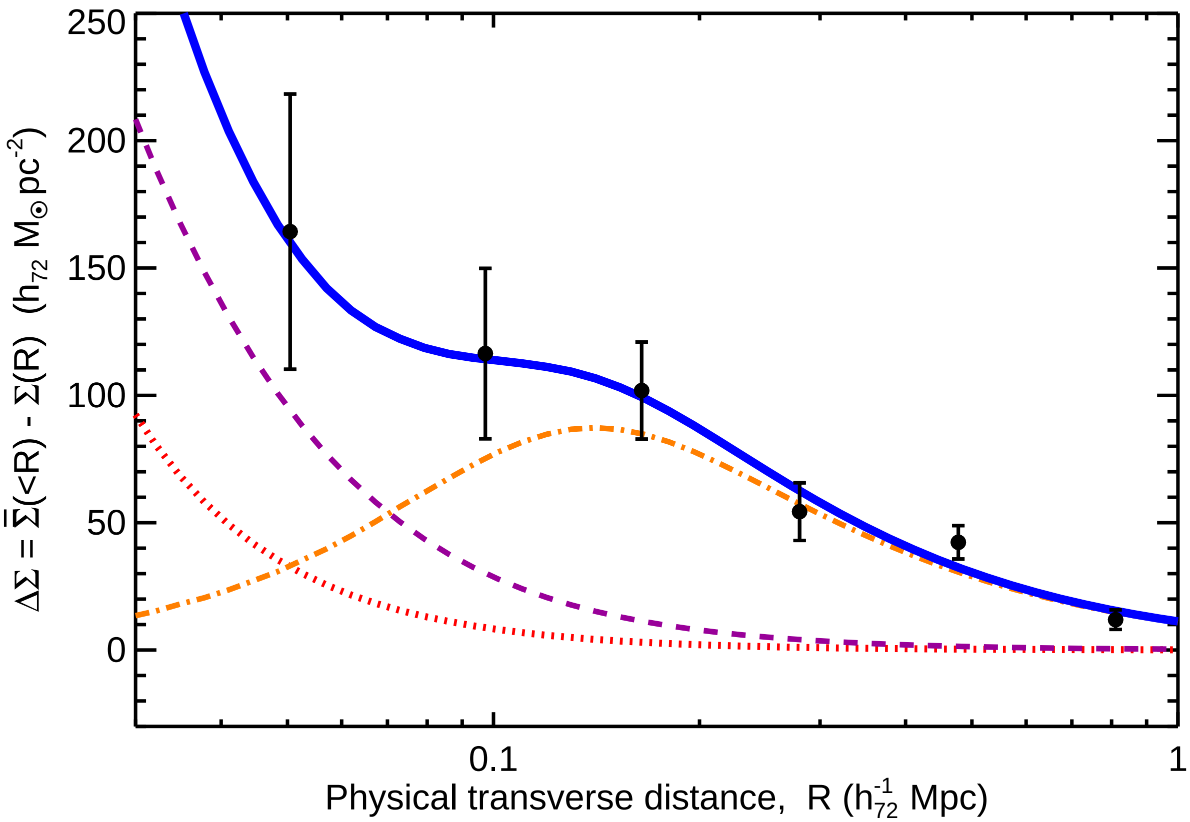

Figure 3.7: Stacked lensing signal for 85 groups where galaxy candidates agree. Model curves show the maximum likelihood solution for an offset NFW halo (orange dot-dashed), subhalo (purple dashed), and a point source for the stellar mass (red dotted), along with the sum (thick solid blue). There are degeneracies among some fit parameters; for example, a model with smaller centering offsets and a less massive subhalo also fits the data.

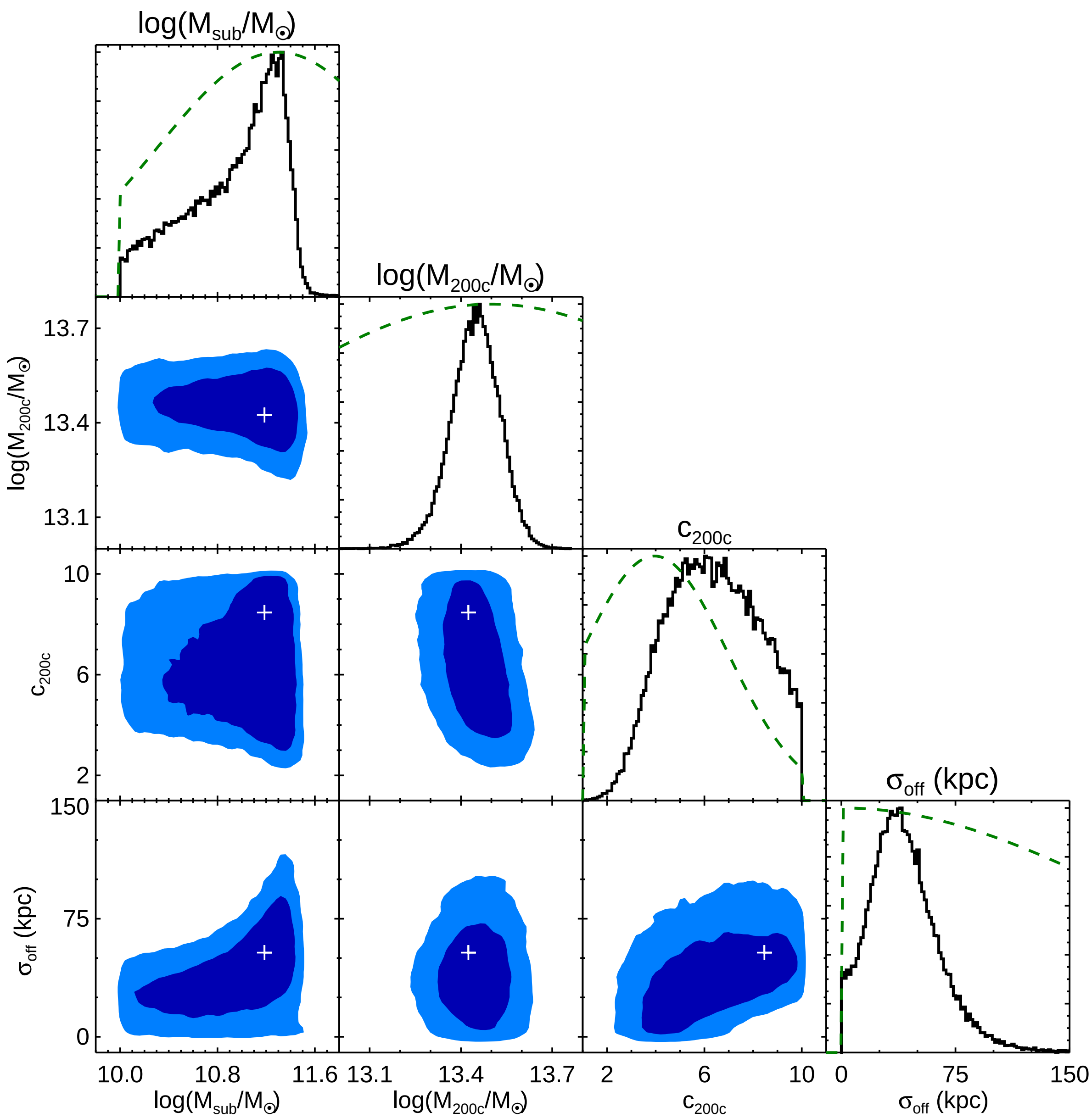

Figure 3.8: Posteriors for the four parameters of a general offset model discussed in the text, applied to the lensing signal from Figure 3.7. Blue contours show 68% and 95% regions for the pair of parameters noted along the axes, marginalized over the other parameters. White crosses mark the maximum likelihood parameters. Top panels show the posterior distributions for single parameters while marginalizing over the others (black histograms), along with arbitrarily normalized priors (green dashed curves).

Chapter 4

Satellite Color and Morphology Transformations

While the star formation rates and morphologies of galaxies have long been known to correlate with their local environment, the process by which these correlations are generated is not well understood. Galaxy groups are thought to play an important role in shaping the physical properties of galaxies before entering massive clusters at low redshift, and transformations of satellite galaxies likely dominate the buildup of local environmental correlations. To illuminate the physical processes that shape galaxy evolution in dense environments, we study a sample of 116 X-ray selected galaxy groups at $z = 0.2 - 1$ with halo masses of $10^{13} - 10^{14}$ $M_\odot$ and centroids determined with weak lensing. We analyze morphologies based on *HST* imaging and colors determined from 31 photometric bands for a stellar mass-limited population of 923 satellite galaxies and a comparison sample of 16644 field galaxies. Controlling for variations in stellar mass across environments, we find significant trends in the colors and morphologies of satellite galaxies with group-centric distance and across cosmic time. Specifically at low stellar mass ($\log(M_\star/M_\odot) = 9.8 - 10.3$), the fraction of disk-dominated star-forming galaxies declines from $> 50\%$ among field galaxies to $< 20\%$ among satellites near the centers of groups. This decline is accompanied by a rise in quenched galaxies with intermediate bulge+disk morphologies, and only a weak increase in red bulge-dominated systems. These results show that both color and morphology are influenced by a galaxy's location within a group halo. We suggest that strangulation and disk fading alone are insufficient to explain the observed morphological dependence on environment, and that galaxy mergers or close tidal encounters must play a role in building up the population of quenched galaxies with bulges seen in dense environments at low redshift.

4.1 Introduction

Galaxy properties are correlated with their environment. Dense regions host galaxies with greater masses, lower star-formation rates, and morphologies that are more bulge-dominated than in low density regions. Since the early work of Dressler (1980), studies of environmental correlations have expanded to a variety of indicators of star formation, morphology, and environment. See Blanton & Moustakas (2009) for a recent review of these correlations in the local universe.

Numerous processes may be culpable for the dependence of galaxy properties on environment (see Boselli & Gavazzi 2006 for a review). Galaxy interactions through mergers or tides can disrupt stellar kinematics and remove gas. These interactions can also apply torques that drive gas inward, perhaps feeding star formation or a central black hole. Halos can play a role through tidal forces and dynamical friction. Pressure from hot dense gas inside halos may strip gas from infalling galaxies, and shock heating in massive halos can prevent accretion of cold gas that would feed star formation.

Despite extensive observational and theoretical work, the dominant physical mechanisms responsible for the environmental correlations remain unclear. An important clue is that the scale on which these correlations appear is similar to the size of the dark matter halos hosting galaxies (e.g., Kauffmann et al. 2004; Blanton & Berlind 2007). Relatedly, satellite galaxies have a primary role in the buildup of the red sequence in dense environments (e.g., Weinmann et al. 2006; van den Bosch et al. 2008; Wetzel et al. 2012a; Peng et al. 2012).

Since many galaxy characteristics are interrelated, it is important to study the correlations for each property independently while fixing other variables. When constraining environmental effects, one ideally controls for differences in redshift, stellar mass, halo mass, and location within a group. The colors and morphologies of galaxies are also correlated, so it is advantageous to split galaxies simultaneously by color and morphological classes to distinguish between processes that affect star formation rates and structural properties differently. Several studies have suggested that environmental processes affect star formation more significantly than morphology (e.g., Kauffmann et al. 2004; Blanton et al. 2005; Christlein & Zabludoff 2005; Weinmann et al. 2009; Kovač et al. 2010), suggesting that the gas that feeds star formation is depleted or removed without significantly altering galactic structure or stellar kinematics.

While many of the observational studies have focused on large surveys at low redshift or on massive clusters at higher redshifts, less is known about the more common group-scale environments and their evolution over time. In this chapter, we study the colors and morphologies of galaxies in groups spanning the redshift range $z = 0.2 - 1$. We focus in particular on the properties of satellite galaxies as a function of stellar mass, group-centric distance, and redshift. This sample of groups has been identified from the COSMOS field (Scoville et al. 2007) based on their extended X-ray emission and have masses determined with weak lensing in the range $10^{13} - 10^{14} M_{\odot}$ (Leauthaud et al. 2010). Galaxy membership has been assigned using precise photometric redshifts with a Bayesian procedure tested extensively with mock catalogs and a spectroscopic subsample (Chapter 2; George et al. 2011). Furthermore, by finding galaxies that maximize the lensing signal on small scales we have identified central galaxies that accurately trace the center of mass of their halos (Chapter 3; George et al. 2012). Additional studies of these groups with magnification lensing (Ford et al. 2012; Schmidt et al. 2012) and clustering (Allevato et al. 2012) have confirmed the halo mass estimates. These ingredients make for a robust characterization of group environments with which to study satellite properties and their evolution over time.

We describe the data used in this analysis in Section 4.2 along with mock catalogs used to estimate the purity of the satellite population analyzed. Section 4.3 presents the results including our primary finding of a declining fraction of blue late disk galaxies and a rise in red early types toward group centers and over cosmic time. In Section 4.4, we discuss the implications of these findings for the physical mechanisms that shape galaxy evolution, and put this work in the context of previous studies and possibilities for the future.

4.2 Data and Mocks

The COSMOS field (Scoville et al. 2007) has been the subject of a broad array of multi-wavelength imaging and spectroscopy campaigns. In this study we make use of several pieces of this data: galaxy colors, photometric redshifts, and stellar masses derived from over thirty bands of ultraviolet, optical, and infrared data (Ilbert et al. 2009, 2010; Bundy et al. 2010); galaxy morphologies determined by Scarlata et al. (2007) from high-resolution imaging taken by the Advanced Camera for Surveys (ACS) aboard the *Hubble Space Telescope* (Koekemoer et al. 2007); and a catalog of massive galaxy groups selected based on their X-ray emission seen with *XMM-Newton* and *Chandra* and for which halo mass profiles have been characterized using weak lensing with *Hubble* imaging (Leauthaud et al. 2010; George et al. 2011, 2012). Most of these data have been compiled in the group member catalog published in George et al. (2011) and we refer the reader to that paper (or Chapter 2) and references therein for further details including the flux and mass limits for galaxies and groups. Here we briefly explain the stellar masses, colors, and morphologies used, as well as the identification of group centers and the mock catalogs used for validating group membership assignment and estimating the effects of contamination from field galaxies.

4.2.1 Group Membership and Mocks

As a measure of galaxy environment, we use a catalog of groups described in George et al. (2011). These groups have been identified through a wavelet detection of extended X-ray emission following Finoguenov et al. (2010) and the sample is an expanded version of an earlier COSMOS catalog (Finoguenov et al. 2007) with deeper X-ray data. A Bayesian membership algorithm is used to associate galaxies with groups based on precise photometric redshifts and proximity to the X-ray position, with a prior accounting for the relative field population as a function of magnitude and redshift. Following George et al. (2011), we select galaxies with membership probability $P_{\rm mem} > 0.5$ among the clean sample of groups, avoiding masked regions, groups with fewer than four members, overlapping groups, and possible projections (FLAG_INCLUDE=1 in the catalog). Halo masses for these groups have been measured with stacked weak lensing to be in the range $M_{200c} \approx 10^{13} - 10^{14} M_\odot$ and are correlated with X-ray luminosity (Leauthaud et al. 2010; George et al. 2012). Over this limited range in halo masses, we have not detected significant trends in galaxy properties with X-ray luminosity, but to avoid the influence of outliers we eliminate a small number of groups with halo masses estimated from their X-ray luminosities following Leauthaud et al. (2010) that are above or below the $10^{13} - 10^{14} M_{\odot}$ range.

We split galaxies into central, satellite, and field populations across several stellar mass and redshift bins to isolate dependences among different properties. For each group, the central galaxy is defined as the most massive group member within a projected distance of the X-ray position equal to the scale radius of a Navarro-Frenk-White (Navarro et al. 1996) profile. George et al. (2012) showed with weak lensing tests that this definition traces the halo center to within roughly 75 kpc, though in roughly 30% of groups the center is still ambiguous. In this chapter we do not specifically study the central galaxies in these X-ray selected halos because their abundance limits statistical constraints on the properties of this population. The remaining group members are called satellites, and are the primary focus of this work. Field galaxies are taken to be those not assigned to any extended X-ray source and are thus expected to reside in halos less massive than the X-ray detection limit ($P_{\rm mem} = 0$ from George et al. 2011; see Figure 1 of that paper for the X-ray flux limit as a function of redshift). Because we do not detect faint X-ray groups at high redshift, the halo mass range occupied by the field population can evolve due to this selection effect. However, at low redshift only $\sim 10\%$ of galaxies in our sample live in X-ray groups, so we expect the evolving halo mass limit to have only a small effect on the statistics of the field population. Table 4.1 gives the size of each of these samples used in our analysis.

Extensive tests of the accuracy of the photometric redshifts and membership assignment algorithm have been carried out using mock catalogs from simulations as well as a subsample of galaxies with spectroscopic redshifts (George et al. 2011). The overall purity and completeness of the member selection within $0.5R_{\rm 200c}$ is 84% and 92%, respectively, down to our flux limit of F814W = 24.2. The accuracy of member selection depends most significantly on distance from the group center and on the flux of a galaxy. The first effect is due to the decreasing density of true members with group-centric distance, which implies that selecting galaxies uniformly with radius (out to $R_{\rm 200c}$) will result in higher contamination from field galaxies in the outskirts. The second effect from galaxy flux arises from the decreasing precision of photometric redshifts for fainter galaxies, ranging from $\sigma_z \lesssim 0.01$ at F814W < 22.5 to $\sigma_z = 0.03$ at F814W = 24. It is notable that with the many filters used in constructing these photometric redshifts, precision does not depend significantly on spectral type, so red and blue galaxies of a given magnitude are selected with similar completeness.

In our analyses of member populations, we correct for contamination from field galaxies using the mock catalogs described in George et al. (2011). A halo catalog is constructed from a LasDamas simulation (C. K. McBride et al., in preparation)[1] and populated with group members following the halo occupation model of Leauthaud et al. (2012a). Mock galaxies are matched to real COSMOS galaxies in narrow bins of stellar mass and redshift to assign magnitudes in the F814W band, which in turn are used to assign mock photometric redshift

[1]Details regarding the LasDamas "Consuelo" simulation can be found at `http://lss.phy.vanderbilt.edu/lasdamas/simulations.html`

Table 4.1: Environmental Census

Type	Stellar Mass $[\log(M_\star/M_\odot)]$ $[9.8, 10.3)$	$[10.3, 10.8)$
$z = 0.2 - 0.5; N_{\rm groups} = 47$		
Satellites	237	218
Field	2455	1993
$z = 0.5 - 0.8; N_{\rm groups} = 40$		
Satellites	122	189
Field	4497	3529
$z = 0.8 - 1.0; N_{\rm groups} = 29$		
Satellites	...	157
Field	...	4170

Note. — No contamination corrections have been applied. Ellipses denote a bin below our stellar mass completeness limit.

errors. We estimate the purity of the member selection algorithm in bins of group-centric distance and magnitude, and assume that the colors and morphologies of contaminating field galaxies are representative of the field population at that magnitude. Contamination corrections are applied to the satellite populations only, since the field population is much larger. These corrections only account for contamination of the member list and not for incompleteness; the latter effect is smaller, does not significantly depend on group-centric distance, and should be fairly uniform across galaxy types since the precision of photometric redshifts is effectively achromatic (see Figures 2 and 5 of George et al. 2011).

4.2.2 Stellar Masses, Colors, and Morphologies

Stellar masses and spectral classes have been determined by fitting stellar population synthesis models to the spectral energy distributions of galaxies, varying the age, amount of dust extinction, and metallicity in the models. We use the stellar masses from Bundy et al. (2010) and color classifications from Ilbert et al. (2010), both of which are based on Bruzual & Charlot (2003) models fit with a Chabrier (2003) initial mass function but take somewhat different approaches to fitting the data. Using the unextincted rest-frame color $(\mathrm{NUV} - \mathrm{r}^+)$ of the best-fitting template for each galaxy, we split them into two color classes:

- *red*: $(\mathrm{NUV} - \mathrm{r}^+) > 3.5$
- *blue*: $(\mathrm{NUV} - \mathrm{r}^+) < 3.5$.

Ilbert et al. (2010) showed that this color cut corresponds with a specific star formation rate of roughly $10^{-11}\mathrm{yr}^{-1}$. It is worth emphasizing that these colors are corrected for dust extinction, so that the red sample selects a population of quiescent galaxies similar to those identified using two color cuts based on near-ultraviolet, optical, and near-infrared measurements, minimizing contamination from dusty star-forming galaxies (e.g., Bundy et al. 2010).

Galaxies are classified morphologically based on automated measurements of several structural parameters from ACS imaging in the F814W band. We use the Zurich Estimator of Structural Types (ZEST; Scarlata et al. 2007) catalog, which is derived from measurements of the asymmetry, concentration, Gini coefficient, second moment of the brightest pixels, and ellipticity. Scarlata et al. (2007) performed a principal component analysis of these measured quantities to identify the most important structural parameters, and divided galaxies into classes (early type, disk, and irregular) based on their location in this principal component space. A further subdivision of the disk category was derived by correlating measurements of the Sérsic index for a bright sample with $I_{AB} < 22.5$ with location in the principal component space. This parametrization provides a rough indication of the bulge-to-disk ratio, with four classes ranging from bulge-dominated to bulgeless disks. For statistical purposes, we consolidate some of these classifications into three morphological categories:

- early type *spheroidals* and bulge-dominated disks including even relatively inclined S0 galaxies (ZEST types 1 and 2.0)

- intermediate *bulge+disk* galaxies (ZEST type 2.1)
- *late disks* with little or no bulge component (ZEST types 2.2 and 2.3).

Irregulars and unclassified galaxies make up a small fraction of the sample, typically not more than a few percent in any stellar mass bin. We note that morphological K-corrections, which have not been applied, should not have a large effect on our sample because the F814W band probes rest-frame optical wavelengths over our entire redshift range (e.g., Lotz et al. 2004; Cassata et al. 2005; Bundy et al. 2010).

4.3 Results

We begin our analysis with a visualization of a few properties of the galaxies in our sample. Figure 4.1 shows the distributions of stellar masses and group-centric distances in different redshift bins for all galaxies selected as group members. Each point represents one object and is displayed using the ACS image of the galaxy (Koekemoer et al. 2007), colored according to the average unextincted rest-frame template ($\mathrm{NUV} - \mathrm{r}^+$) color. Centrals are positioned on the left of each panel with small horizontal offsets, and satellites are plotted at their distance from the corresponding central. Each image is basically the set of adjacent pixels with flux above a noise threshold shown with a logarithmic surface brightness scale that has its maximum set to the peak value for each galaxy. We note that the apparent size of a galaxy on the plot is quite sensitive to its flux since images of brighter galaxies have more pixels above the noise threshold, and this is not a perfect indicator of the physical effective radius of a galaxy. A small fraction of objects have deblending issues or edge effects from the cutout image size, but we note that the images are processed independently for visualization and analysis purposes.

Several trends are evident when visualizing galaxies in this manner. Stellar mass is a strong determinant of galaxy properties; massive galaxies are more likely to be large, red, and spheroidal. Physical properties also depend on the location within a group. Central galaxies are massive (by definition), but also typically red and elliptical. Blue centrals tend to be less massive than red centrals at high redshifts even within the fairly narrow range of halo masses studied here, as discovered by Tinker et al. (2012). Satellites closer to group centers are more likely to be red and show fewer spiral features than in the outskirts, particularly at low stellar masses. There is a relative dearth of low mass satellites near group centers; this could be a hint of satellite depletion due to mergers, but challenges in measuring photometry of faint objects near massive extended central galaxies could be a contributing factor so further investigation is needed. Similar evidence of mass segregation and the influence of mass and environment on star formation has been seen in groups and clusters out to $z \sim 1$ (Muzzin et al. 2012; Presotto et al. 2012). Many of these trends can be seen across the entire redshift range studied here, indicating that both stellar mass and halo environment play a role in determining galaxy properties at least since $z = 1$. Sample variance due to the finite survey volume does affect our ability to measure absolute redshift trends as the number densities vary significantly due to large-scale structures (particularly evident at $z = 0.3 - 0.4$), but the relative fractions of different populations should be less affected.

The central panel of Figure 4.1 shows a few examples of the three morphological classifications from ZEST, chosen randomly to span the range of colors seen from redshifts $z = 0.4 - 0.6$ and with $\log(M_\star/M_\odot) > 10$. While these classifications do not always agree with one's visual impression, there are clear differences in structural parameters among the classes, and correlations between these automated measurements and a galaxy's position in a group can provide an interesting test of the dependence of morphology on environment. We emphasize that the ZEST morphologies are correlated with, but not identical to, traditional visual classification of ellipticals and spirals. We compare results from multiple morphological indicators in Section 4.3.3.

4.3.1 Radial Trends: Blue Late Disks into Red Bulge+disks

We can quantify some of the trends from Figure 4.1 by measuring the fraction of galaxies of a given color and morphology as a function of stellar mass, group-centric distance, and redshift. Figure 4.2 shows the fraction of galaxies in each of the six combinations of color and morphology categories described in Section 4.2.2. For example, the cyan triangles represent the fraction of galaxies in the stellar mass and redshift range shown that are both blue and have late disk morphology. This population makes up the majority among field galaxies (shown at $R > R_{200c}$) but its fraction declines among satellites, contributing less than 20% of the satellite population at $R < R_{200c}/3$. Meanwhile, the proportion of red bulge+disk galaxies rises from 7% in the field to 40% among satellites in the inner radial bin.

Figure 4.2 highlights the most significant environmental trends in our sample by focusing on low mass, low redshift galaxies. We repeat the exercise in Figure 4.3 with higher mass and redshift bins to study how these trends vary. The broad picture is similar; blue late disks dominate in the field while the red bulge+disk population becomes more prominent toward group centers. Among low mass galaxies at $z > 0.5$, the blue late disks dominate everywhere, while more massive galaxies at lower redshift have a substantial population of red spheroidals. Red late disks and blue spheroidals do not make up a large portion of galaxies at any mass or redshift studied. The red fraction can be determined from these plots by summing the three red lines, and similarly the spheroidal fraction is the sum of the solid lines with circular markers. The red fraction rises toward group centers for low mass galaxies, but is relatively flat among massive galaxies. We note that the abscissa for these plots is the projected group-centric distance, and that the true radial trends measured in spherical shells are likely more significant than observed.

4.3.2 Redshift Trends

Since satellites tend to fall toward halo centers, group-centric distance is related to the timescale that galaxies have been inside the group. The range of redshifts sampled with this data set provides another measure of time to study evolution. Figure 4.4 is a transpose of Figure 4.3 to show the redshift trends in the distribution of colors and morphologies. Again, there is a decline in blue late disks among low-mass satellites near the centers of groups, now compensated by a rise in both red spheroidals and red bulge+disks. This trend weakens away from group centers and at higher masses.

4.3.3 Checks for Systematics

Environment

There are several possible biases or other effects in the data to consider in order to ensure the robustness of these results. First, we revisit the contamination of our satellite sample due to interloping field galaxies, discussed in Section 4.2.1. In Figures 4.2, 4.3, and 4.4 we have plotted values of population fractions for satellites corrected for contamination estimated from mock catalogs. Contamination corrections are always smaller than the statistical error bars estimated via bootstrapping, except for low mass blue disk galaxies where it is 10% greater than the error because the field population is so large. Though the sample of satellites near R_{200c} is significantly contaminated by field galaxies, the corrections to the relative fractions of each galaxy type are small because the field populations are not markedly different from the outer satellites.

Color Distribution

When classifying galaxies by their spectral energy distributions (SEDs), our primary aim is to distinguish star-forming galaxies from those that are quenched. Though traditional indicators from emission lines or spectral breaks are not directly available from photometry, the 31-band SEDs used here provide a wealth of information about spectral types, including an estimate of dust extinction that separates star-forming galaxies that appear red due to dust from those that are truly passive. The template-based, extinction-corrected ($\mathrm{NUV} - \mathrm{r}^+$) colors used in this work generally have a bimodal distribution with the color cut from Section 4.2.2 falling on the red end of the "green valley." The color distributions for different morphological types are shown in Figure 4.5. Shifting the cut slightly in either direction shifts the amplitude of the red fraction in Figures 4.2, 4.3, and 4.4 up or down, but the trends with group-centric distance and redshift do not vary significantly. We have tested an alternative "red sequence" selection suggested by Ilbert et al. (2010), $\mathrm{NUV} - \mathrm{r}^+ > 0.5\log(M_\star/M_\odot) - 0.8z - 0.5$, using rest-frame absolute magnitudes but applying no extinction correction. The transformation of blue late disks into red bulge+disks among low mass satellites is still evident. Similarly, applying the two-color cut in the $\mathrm{NUV} - \mathrm{r}^+$, $\mathrm{r}^+ - \mathrm{J}$ plane used by Bundy et al. (2010) does not qualitatively change our results.

Morphologies

Morphological classification is a challenging problem and significant scatter exists between the types assigned to galaxies in both visual and automated analyses. In general, visual analyses emphasize the presence or absence of spiral features, categorizing objects as spirals or ellipticals, often with an intermediate class of S0s grouped with ellipticals. Automated analyses measure structural parameters such as concentration and asymmetry which are then generally tied to a training set of visual classifications. The correlation between the properties measured is imperfect, so we test the impact on our results of using a variety of automated morphological classifications, all based on the ACS F814W imaging. The alternative classifications come from Tasca et al. (2009), which presented three separate techniques.

The differences between the results of each catalog and those from the ZEST classification used here are driven by how bulge+disk galaxies are classified, since the other catalogs do not split the spiral/disk category into multiple bins as ZEST does. For instance, among the 237 satellites used for Figure 4.2, the ZEST classifications are 22% spheroidal, 36% bulge+disk, 37% late disk, and 5% irregular or unclassified. The three separate classifications for these galaxies from Tasca et al. (2009) vary between 39 – 59% E/S0s and 59 – 40% spirals. When bulge+disk galaxies are mostly classified as E/S0s, the spheroidal populations (both blue and red) in Figures 4.3 and 4.4 are significantly elevated but show similar trends with group-centric distance and redshift. In the opposite case where bulge+disk galaxies are mostly treated as disks, the spheroidal fraction is essentially unchanged. While the dominant population in each panel of Figure 4.3 and 4.4 can change depending on which category the intermediate bulge+disk galaxies fall into, the radial trend in low mass satellites is unchanged; the blue late type fraction declines toward group centers and is compensated with a rise in red early types. The redshift trend for this transition is strongest for low mass satellites near group centers and weakens toward larger radii and stellar masses. Though the scatter between morphological classifications signals that our results should be interpreted and compared to others with caution, the significant trends with group-centric distance and redshift for the intermediate bulge+disk galaxies suggests that the ZEST classification has identified a population in transition.

A Population of Blue Spheroidals

While the tests described above suggest that our measures of environment, color, and morphology are robust, we do note a puzzling population of massive blue spheroidals that can be seen most clearly in the bottom right panel of Figure 4.4 as well as the right column of Figure 4.5. Those plots suggests that half of all spheroidals in that stellar mass range are blue, exceeding measurements in other studies (e.g. Kaviraj et al. 2007, 2008; Bamford et al. 2009; Schawinski et al. 2009; Ilbert et al. 2010), but see also Cross et al. (2004) who found a large fraction of blue ellipticals in a luminosity-selected sample at moderate redshift. We see a similarly large blue fraction among spheroidals at higher masses ($\log(M_\star/M_\odot) > 10.8$, not plotted) where spheroidals make up a higher proportion of all galaxies, and most prominently at low redshift ($z < 0.5$). Visual inspection of the ACS images of these galaxies suggest that $30-40\%$ show spiral or irregular features, although the structural parameters measured by the automated classifiers are all consistent with the red spheroidal population. We have also investigated the UV-optical and optical-IR colors of these massive blue spheroidals prior to template fitting, in addition to optical spectra for 30 of these objects described in George et al. (2011). These data suggest that blue spheroidals are not typical star-forming galaxies but may have a small amount of recent star formation to which rest-frame UV measurements are particularly sensitive (e.g. Kaviraj et al. 2007, 2008). Another possible explanation is that there are unusual stellar populations that are not represented in the template fits used to derive our ($\mathrm{NUV}-\mathrm{r}^{+}$) colors (see e.g. Smith et al. 2012, for a discussion of galaxy properties contributing to the "UV upturn"). While this population is interesting in its own right, it is most prominent at high stellar masses and does not show a strong dependence on environment, so we do not consider it further here.

4.4 Discussion and Conclusions

Our results indicate a complex relationship between color, morphology, stellar mass, and group-centric distance. Trends in color and morphology are distinct, and the use of a single property as proxy for galaxy type does not capture the whole picture. The most interesting trend seen is the shift in dominance among the low mass population from blue late disk galaxies in the outskirts to red bulge+disk types in group interiors. If part of one population was merely disappearing from the sample, either due to changes in mass or merging with other galaxies, then the other populations would all be expected to grow by an equal factor. The fact that the decline in one population is roughly balanced by the rise of a single other population suggests a transformation process. We now discuss these results in the context of past analyses, the physical implications of the present work, and future avenues to clarify the role of environment in galaxy evolution.

4.4.1 Connection to Previous Observations

There is a long history of research into the covariance between the stellar masses, colors, morphologies, and environments of galaxies and its evolution with time. After controlling for differences in stellar mass or luminosity, numerous studies at low redshift have found that color is more strongly correlated with environment than morphology (e.g., Kauffmann et al. 2004; Blanton et al. 2005; Christlein & Zabludoff 2005; van den Bosch et al. 2008; Bamford et al. 2009; Skibba et al. 2009; Weinmann et al. 2009). The implication of these studies is that the well-known correlation between morphology and environment is secondary to correlations between morphology and stellar mass or color, with the latter properties more physically linked to environment. Still, some of these studies find residual correlations between morphology and environment after controlling for color and stellar mass or luminosity, particularly at low masses and among late to intermediate morphologies (Blanton et al. 2005;

Weinmann et al. 2009; Skibba et al. 2012).

Moving from large low-redshift studies to moderate redshifts ($z \sim 0.4$), Balogh et al. (2009) and McGee et al. (2011) have shown that groups still host a higher fraction of red galaxies than the field, while Wilman et al. (2009) found an elevated S0 fraction in groups with a mildly significant rise with group-centric distance. This radial trend in morphology is the opposite of that seen in Figure 4.3 but may be due to a smaller sample size or the use of luminosity-weighted centroids, which have been shown to be a poorer tracer of halo centers measured by weak lensing when compared with the most massive galaxy used in this catalog (George et al. 2012).

Environmental trends at fixed stellar mass have been seen to weaken at higher redshift (e.g., Poggianti et al. 2008; Tasca et al. 2009; Cucciati et al. 2010; Iovino et al. 2010; Kovač et al. 2010), though recent analyses have shown clear differences between the fraction of star-forming galaxies across environments over a range of stellar masses at least up to $z \sim 1$ (Cooper et al. 2010; Peng et al. 2010; George et al. 2011; Knobel et al. 2012). Tasca et al. (2009) and Kovač et al. (2010) have compared the dependence of colors and morphologies on local density and in groups in the COSMOS field, finding a stronger effect on color than on morphology, similar to the low redshift results and suggesting a longer timescale for structural transformations than for quenching star-formation. Muzzin et al. (2012) and Presotto et al. (2012) have also shown that the quenched fraction among satellites depends significantly on group-centric distance at these redshifts.

The results presented here extend this work to include radial trends in colors and morphologies from $z = 0.2-1$. Our X-ray group catalog gives a large, clean, and fairly representative selection of $10^{13}-10^{14}$ $M_{\odot}$ halos (Finoguenov et al. 2010), and has been well-calibrated based on its weak lensing signal (Leauthaud et al. 2010; George et al. 2012). We detect significant trends in both color and morphology with group-centric distance. Some previous studies measured weak or insignificant gradients in morphology by using a simple dichotomy of spirals and ellipticals, and we can reproduce these results when using a coarse morphological binning (see discussion in Section 4.3.3). But in contrast to those results, we see clear morphological gradients at fixed stellar mass and color once the morphological classification considers differences in the bulge content of disk galaxies.

The importance of this intermediate morphology between pure disks and spheroidals has been noted before in the context of S0 galaxies which have been known to dominate the evolution in the morphology-density relation (Dressler et al. 1997; Postman et al. 2005; Smith et al. 2005b; Boselli et al. 2006; Moran et al. 2007; Oesch et al. 2010; Lackner & Gunn 2013). Smith et al. (2005b) also showed that morphological evolution occurs later in less dense regions than in the densest regions associated with clusters, with little evolution at intermediate densities from $z = 1$ to 0.5 followed by an increase in early types at lower redshift. There is a significant overlap between the intermediate bulge+disk population in our analysis and visually classified S0 galaxies although these bulge+disk galaxies are often classified slightly later along the Hubble sequence (Scarlata et al. 2007). Our results in Figure 4.4 broadly corroborate those of Smith et al. (2005b) and add that color and stellar mass are also important dimensions when studying these trends.

4.4.2 Implications for Physical Mechanisms of Galaxy Transformation

The radial gradients and redshift trends measured in Section 4.3 suggest a transformation among low mass satellites from blue late disks into red bulge+disks and spheroidals. The mechanism for this transformation must affect both color and morphology, or more physically, the star formation rate and stellar kinematics. Some processes (see e.g. Boselli & Gavazzi 2006, for a review) halt star formation without significantly altering stellar structure, such as gas removal via ram pressure stripping or weak tidal interactions, suppression of gas accretion within dense shock-heated environments, or quasar feedback. On the other hand, galaxy mergers and strong tidal interactions can affect both the distribution of gas needed to form stars as well as the stellar morphology. A third possibility is that color and morphology changes are physically coupled; bulge growth could stabilize a galaxy against disk fragmentation and suppress star formation (Martig et al. 2009), or gas loss may leave a disk unable to dissipate energy from tidal interactions or may drive instabilities leading to bulge growth. Yet another scenario is that a bulge only appears more prominent after a galaxy is quenched because the previously star-forming disk has faded.

We can test these models by studying the morphological dependence on environment among quenched galaxies. Mechanisms like gas stripping or disk fading that do not directly affect morphology should produce a higher fraction of quenched galaxies in dense environments, but among quenched galaxies the morphological distribution should be constant across environments. On the other hand, if quenched galaxies in dense environments have more bulge-dominated morphologies than quenched field galaxies, it would suggest that mergers or strong tidal interactions altering the structure of galaxies occur in addition to, or in conjunction with, the suppression of star formation. The results of this test are plotted in Figure 4.6, where we show the fractions of red galaxies that are early and late type as a function of environment. We have used a broad redshift range and combined the spheroidal and bulge+disk categories to reduce statistical errors for this smaller population of red galaxies. Figure 4.6 demonstrates that quenched satellites, particularly those in the inner regions of groups, are more likely to be bulge-dominated than their field counterparts.

We interpret this to mean that some physical process in dense environments is driving bulge growth. Though some field studies (Bundy et al. 2010; Masters et al. 2010) have already noted a tendency of passive disks to be more concentrated than star-forming disks, we find that the morphological evolution of quenched galaxies is even stronger in groups. Our result is consistent with previous arguments favoring bulge growth over disk fading based on the higher typical luminosities of galaxies with intermediate morphologies compared to late types (Christlein & Zabludoff 2004; Burstein et al. 2005). The data presented here show that even at fixed mass there must be bulge enhancement that accompanies quenching in groups.

The results of Figure 4.3 suggest that the timescale for the morphological transition from late disk to bulge+disk must be comparable to the timescale for quenching in order to turn blue late disks directly into red bulge+disk galaxies. For example, if quenching occurred via gas stripping or removal at a rate faster than any structural changes, we would expect to see blue late disks turning into red late disks. Instead we observe a growth in red galaxies with earlier morphologies whenever blue late disks decline. The fraction of blue late disks plummets by more than a factor of two in ~ 2 Gyr among inner satellites (top left panel of Figure 4.4), while the fraction of red late disks is nearly constant and the fraction of red bulge+disks grows. Similarly, we do not detect a large population of blue bulge+disk galaxies which might be expected if bulge growth happened faster than quenching. These observations suggest that some morphological evolution occurs on a similar timescale as quenching.

At the same time, the morphological transformation observed at low stellar masses has not fully turned many disks into spheroidals. The bulge+disk galaxies are still categorized as disks in the top level ZEST classification. This echoes earlier results finding a buildup of S0s in clusters but weaker evolution in the relative abundance of ellipticals (e.g., Dressler et al. 1997). Though the fraction of red spheroidals does not correlate significantly with group-centric distance (Figure 4.3), it does grow globally with time (Figure 4.4). This may indicate that different processes are responsible for producing bulge+disks and spheroidals.

The discreteness of morphological classification makes detailed comparison of transformations in morphology and color somewhat difficult, but the structural evolution appears to contrast with that in color, where a clear bimodality separates red and blue states and the relatively low intermediate population suggests a fast quenching timescale once it begins (e.g., Wetzel et al. 2012a, though see Balogh et al. 2011). One could test the hypothesis that galaxies pass through an intermediate state between blue late disk and red bulge+disk by measuring the time since quenching based on the SEDs of galaxies in these intermediate states. Is there a difference in the mean color of blue bulge+disks and blue late disks, or between red bulge+disks and red late disks? Figure 4.5 does not show conclusive differences in the colors of these populations, and the satellite sample size is too small to constrain differences in the distribution of colors within the red and blue populations. More detailed analysis with spectroscopic data could better constrain such evolutionary models.

The group environment can play an important role in building up the well-studied color-morphology-density relations in nearby clusters. A group of mass $10^{13.5} M_\odot$ at $z = 1$ should grow through mergers by an average of 0.3 dex to $z = 0$ (Fakhouri et al. 2010), so some of our high redshift groups will be the progenitors of massive clusters and others may accrete onto them. For comparison, a typical star-forming galaxy should grow by 0.2 dex in stellar mass between each of our three redshift bins and by 0.7 dex from $z = 1$ to 0 (Elbaz et al. 2011). Wetzel et al. (2012b) show that the dominant population of satellites in the most massive halos at $z = 0$ were already satellites in groups when accreted. Our results demonstrate that both the color and morphology of these satellites are influenced in the group environment, showing the importance of "preprocessing" of galaxies prior to entering massive clusters. The bulge+disk population we see here is not quite as morphologically evolved as the growing S0 population seen at low redshift and in massive clusters, but likely precedes it.

We summarize our main results and interpretation in Figure 4.7. The left panel shows the positions of satellites for a stacked group and highlights the trend in Figure 4.2 with blue late disks dominating the outskirts and red bulge+disk galaxies making up most of the inner satellite population. This combination of color and morphology transformations suggests some combination of gas removal and bulge growth, shown in the right panel. While the diagram is a simplification of a wide variety of model predictions, the primary point is that *both* color and morphology are affected in group satellites, so physical mechanisms that explain environmental correlations should reflect this.

4.4.3 Future Prospects

While these measurements add insight to the transformation of galaxy properties, much work remains to be done to constrain the variety of physical mechanisms that may be responsible. A cleaner bulge-disk decomposition would be useful to track the growth of bulges and the importance of disk fading (e.g., Lackner & Gunn 2012, 2013). Incorporating the physical sizes of each component would also help to link these transformations with the significant growth seen in early types since $z \sim 2$ (e.g., Bruce et al. 2012). With deep high-resolution imaging from *HST*, the CANDELS survey (Grogin et al. 2011; Koekemoer et al. 2011) is pushing these studies to higher redshift and should also allow bulge-disk decomposition to be studied at multiple wavelengths, identifying when and where star formation is happening or stopping. Alternatively, visual classifications from an ongoing Galaxy Zoo project in the CANDELS fields will track the evolution of spiral features and bars which are challenging for automated techniques. Impending wide field imaging surveys will add greatly to the statistics of these analyses.

Different measures of environment may also help disentangle the relevant physical mechanisms. While we have argued in favor of halo-based indicators (see George et al. 2011 for a discussion), the local galaxy density *within a halo*, in addition to group-centric distance, may shed light on galaxy-galaxy interactions and infalling substructure (e.g., Blanton & Berlind 2007; Cibinel et al. 2012; Woo et al. 2012). However, this indicator is a noisy quantity affected by shot noise, redshift errors, and peculiar velocities, likely requiring deep and complete spectroscopic data for clean results. Larger surveys will also enable a wider range of halo masses to be probed at higher redshift. Comparison of different halo mass proxies can provide a test of environmental mechanisms, for example if X-ray bright groups are more efficient at ram pressure stripping satellites than groups with less hot gas.

These studies can also be extended to the interplay of environmental mechanisms with non-stellar components of galaxies, namely the gas content and central black holes in galaxies. Current and planned radio arrays will extend the study of neutral and molecular gas beyond the local Universe allowing a clearer picture of how star-formation is fed and quenched. And the growth of bulges seen in this work should be connected with accretion onto the central black hole in order to explain the tight correlation seen locally between these components.

Finally, while we have simply presented an empirical description of the data here, we can extend this work by modeling the evolution of color and morphology with environment. Peng et al. (2010) and Wetzel et al. (2012b) present simple empirical descriptions of the fraction of quenched galaxies as a function of stellar mass and environment. Incorporating morphologies into this framework will further illuminate the physical processes at work that build up the environmental correlations we observe.

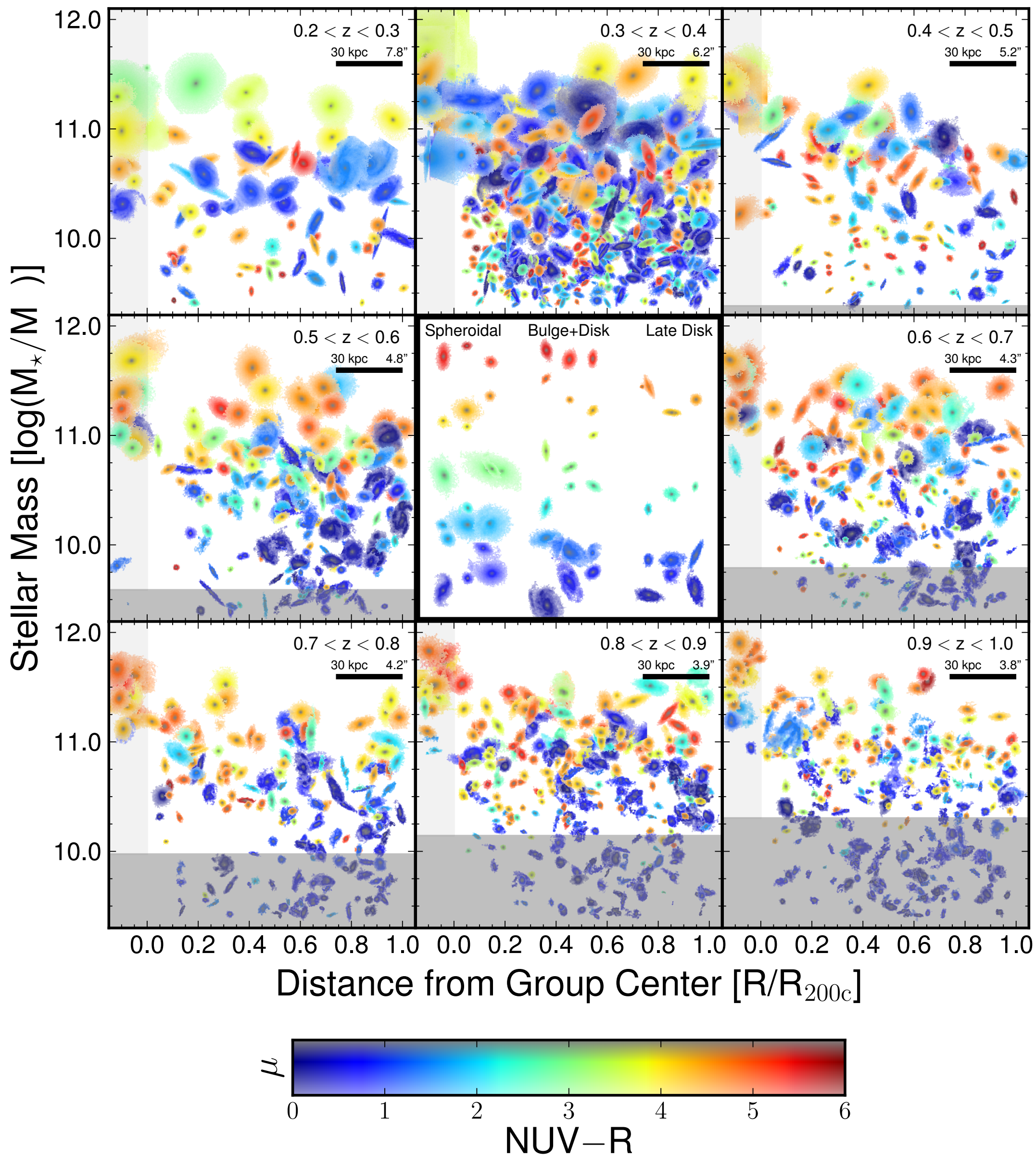

Figure 4.1: Group members as a function of stellar mass and distance from the group center. Colors for each galaxy represent the average unextincted rest-frame template (NUV − r^+) color, with shading proportional to the logarithmic surface brightness μ. The gray band at the bottom of the high-redshift panels shows the stellar mass completeness limit for a passive population calculated with our flux limits F814W = 24.2 and $K_s = 24$ following the approach of Bundy et al. (2010) (see also Figure 1 of George et al. 2011). Central galaxies in these groups are shown in the light gray band on the left side of each of the outer panels. The middle frame shows morphological classifications for a random sample of galaxies chosen to span the range of colors observed; objects in this panel are sorted vertically by color and horizontal offsets within each classification are arbitrary.

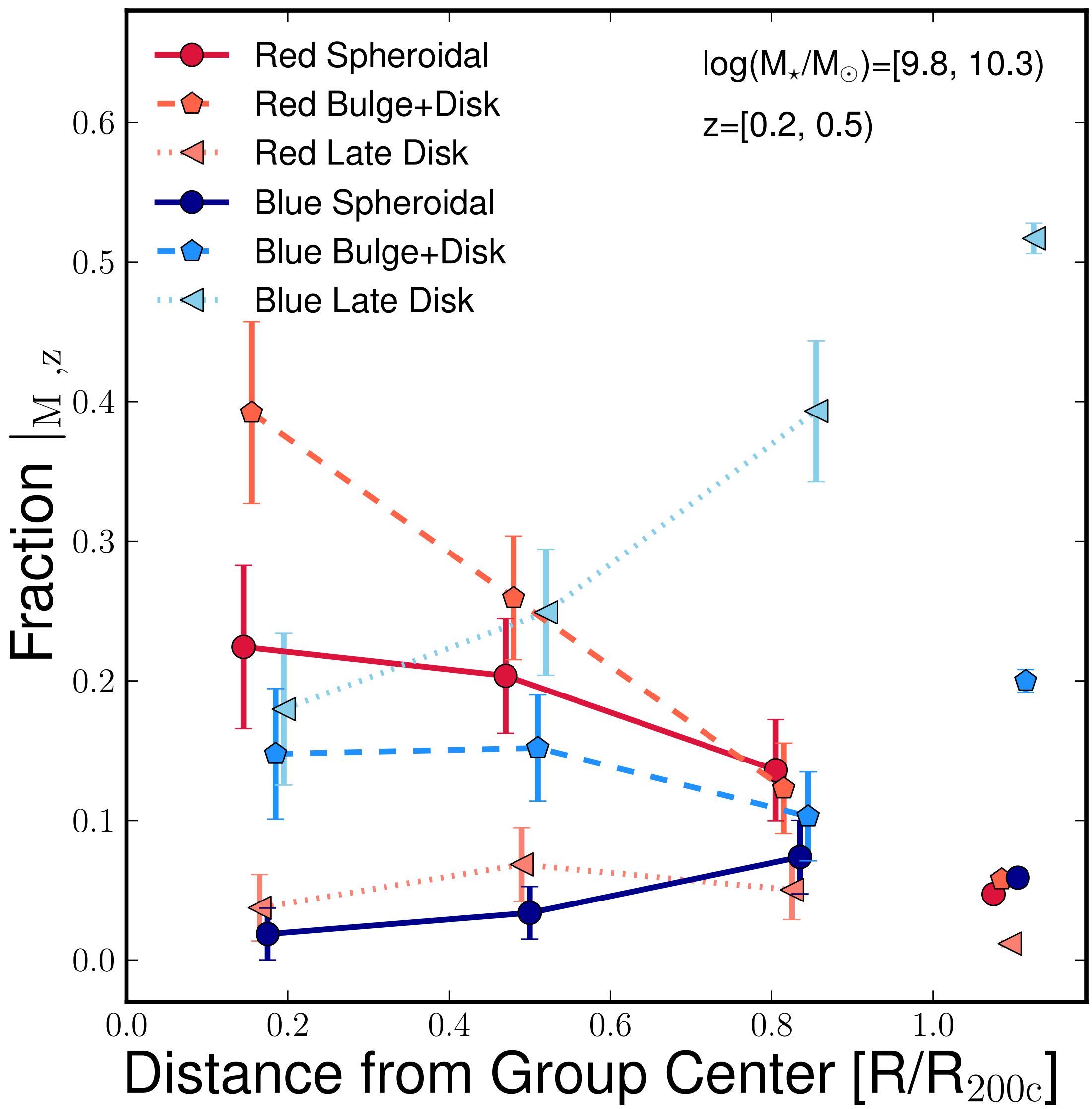

Figure 4.2: Color and morphological fractions as a function of group-centric distance. These fractions are calculated for satellites in three equally-spaced bins out to R_{200c} after applying contamination corrections. The field population is plotted to the right. Points are assigned small horizontal offsets for clarity. Error bars are the 1σ standard deviation of 500 bootstrap samples. There is a clear transition from blue late disks dominating among field galaxies and outer satellites to red bulge+disks among inner satellites.

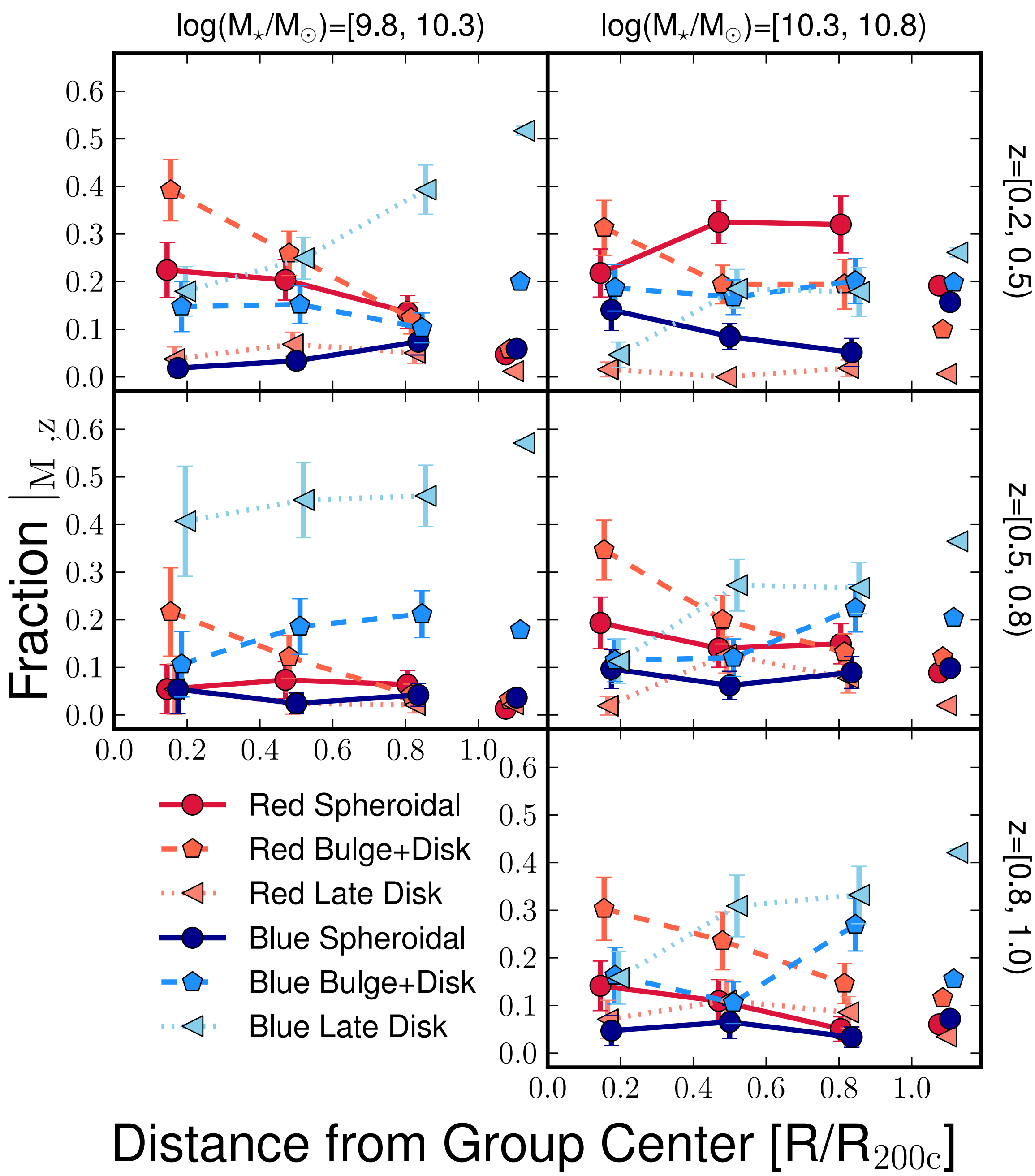

Figure 4.3: Color and morphological fractions of group members as a function of distance from the group center, for different bins of stellar mass (columns) and redshift (rows). Line styles and error bars are as defined in Figure 4.2. Figure 4.2 is repeated in the top left panel, for comparison with weakening environmental trends at higher mass and redshift.

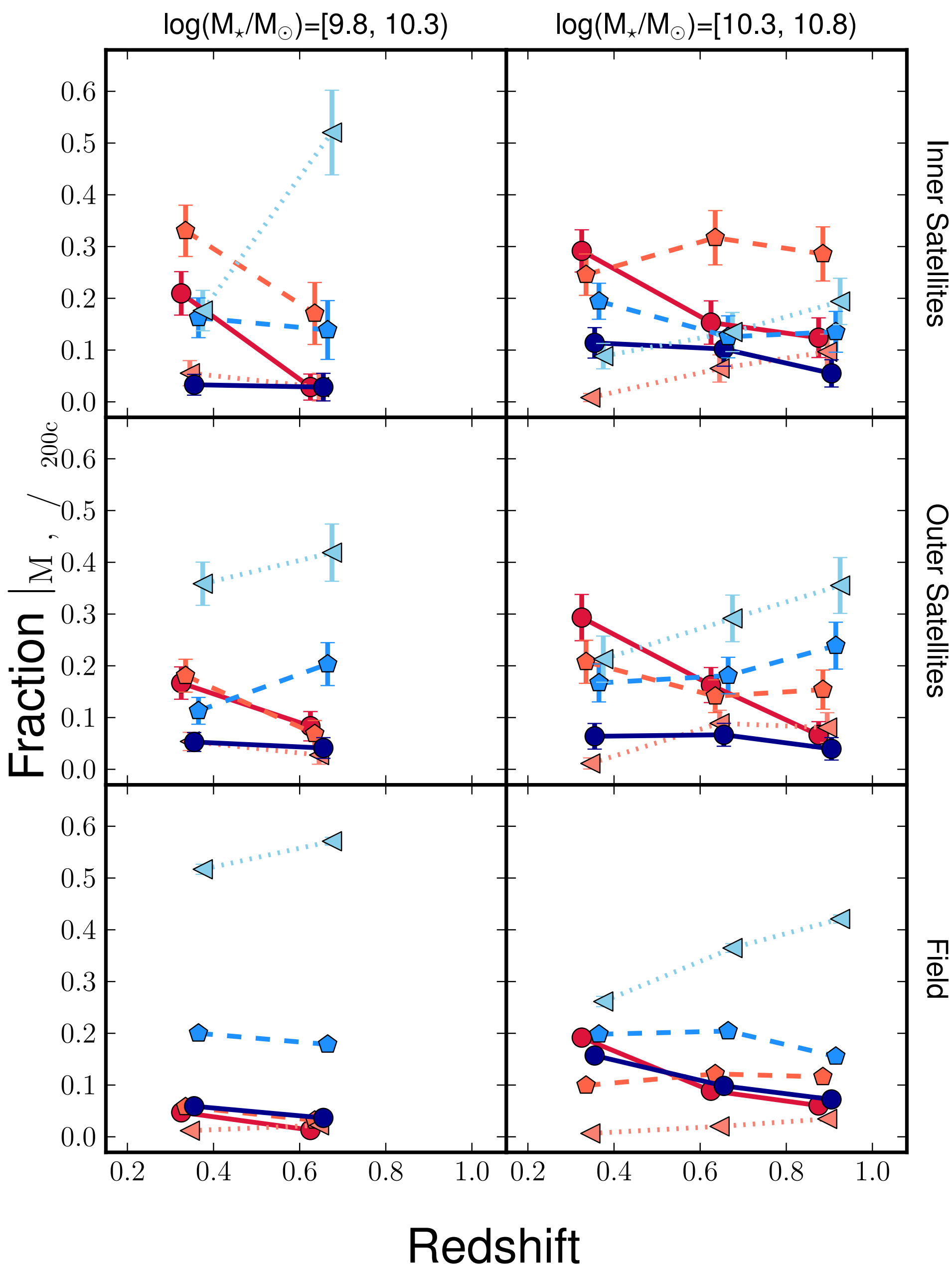

Figure 4.4: Color and morphological fractions as a function of redshift, for different bins of stellar mass (columns) and environment (rows). Inner and outer satellites are separated at a projected group-centric distance of $0.5R_{200c}$. Line styles and error bars are as defined in Figure 4.2.

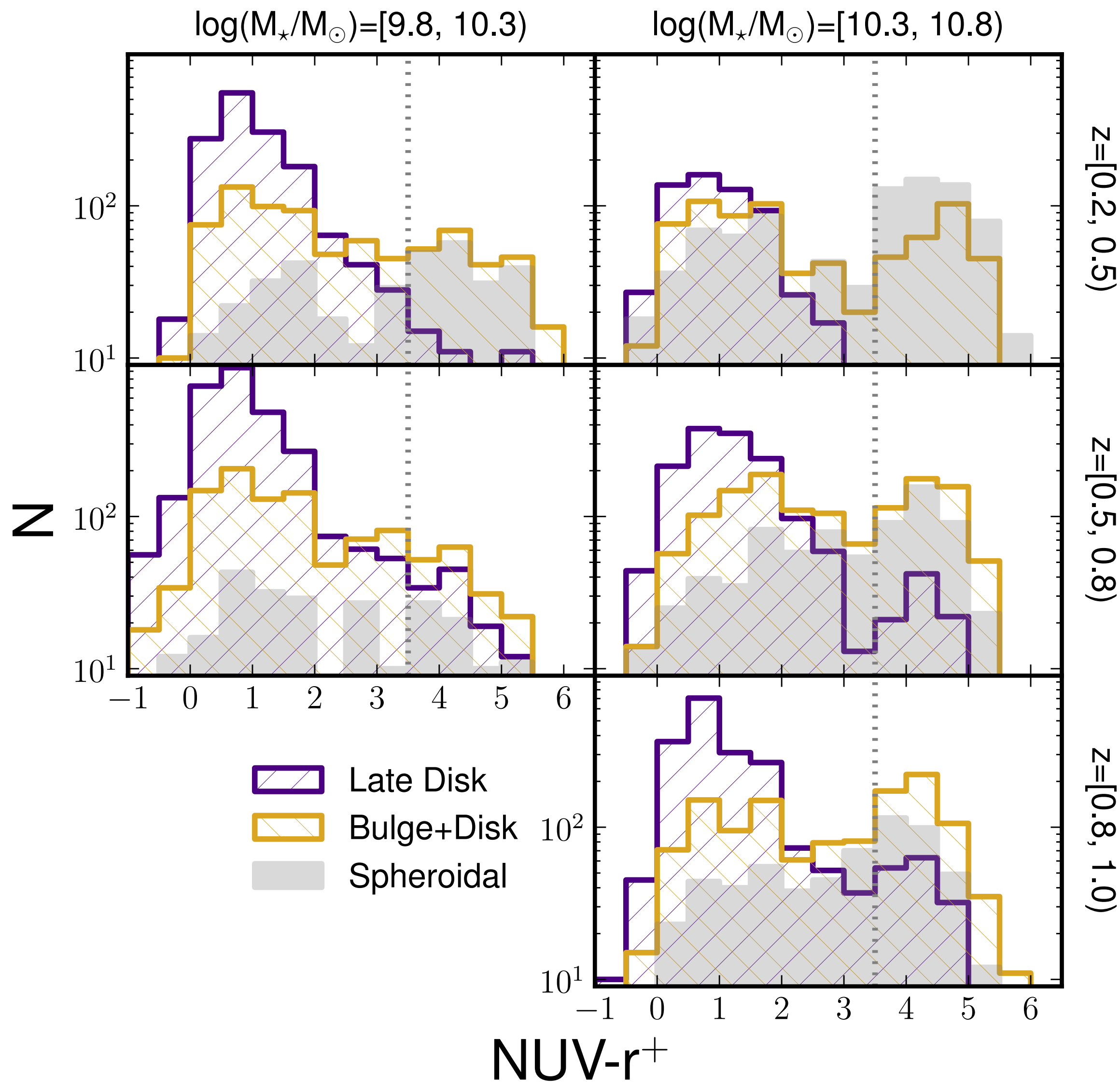

Figure 4.5: Distribution of rest-frame, extinction-corrected, template colors by morphological type. Galaxies from all environments are included. Vertical dotted lines show the cut used to segregate red and blue galaxies.

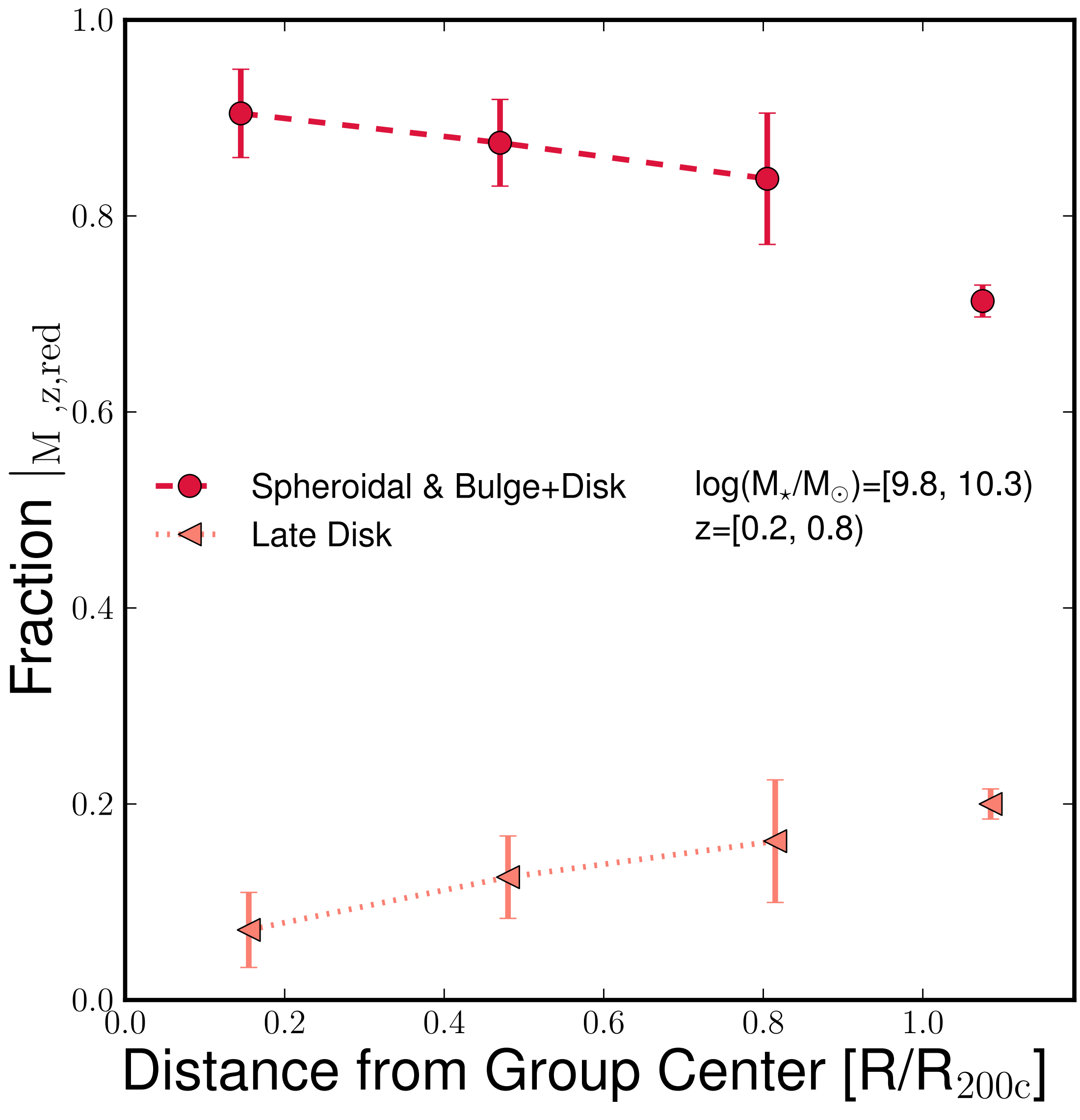

Figure 4.6: Morphological fractions *among red galaxies* as a function of distance from the group center. The small but significant excess in early-type morphologies among inner satellites relative to field galaxies suggests that mergers or tidal interactions cause more significant bulge growth among satellites.

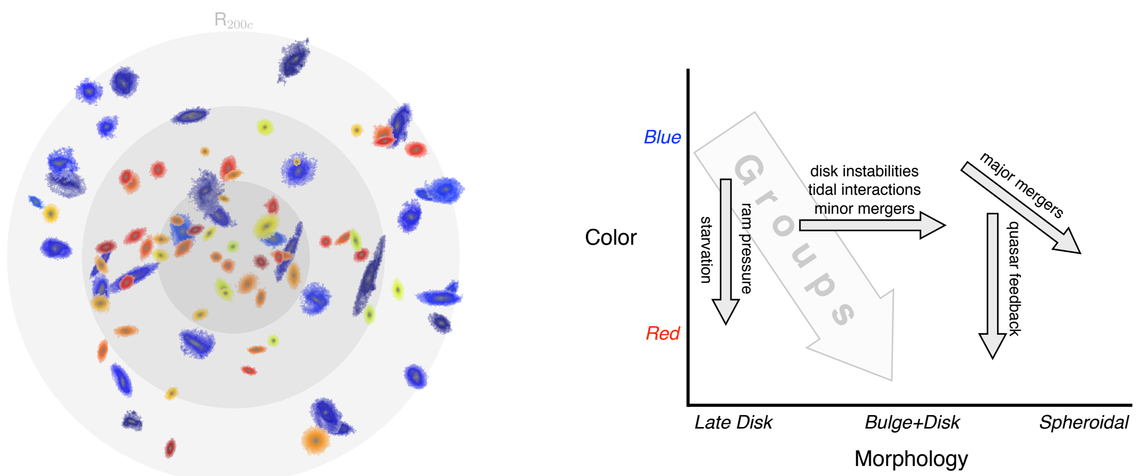

Figure 4.7: Illustrations of our main results and interpretation. Left panel shows the projected positions of satellites in an ensemble group with the same stellar mass and redshift range as Figure 4.2 with only the blue late disks (which dominate the outskirts) and red bulge+disks (which dominate the interior) displayed. The schematic diagram at right shows the effects of various physical mechanisms on color and morphology; the large arrow indicates the observed transformation from blue late disks to red bulge+disks, suggesting a combination of processes.

Bibliography

Adami, C., Mazure, A., Pierre, M., et al. 2010, arxiv:1010.6195

Allevato, V., Finoguenov, A., Hasinger, G., et al. 2012, ApJ, 758, 47

Auger, M. W., Treu, T., Gavazzi, R., et al. 2010, ApJ, 721, L163

Baldry, I. K., Balogh, M. L., Bower, R. G., et al. 2006, MNRAS, 373, 469

Balogh, M., Eke, V., Miller, C., et al. 2004, MNRAS, 348, 1355

Balogh, M. L., McGee, S. L., Wilman, D., et al. 2009, MNRAS, 398, 754

Balogh, M. L., McGee, S. L., Wilman, D. J., et al. 2011, MNRAS, 412, 2303

Bamford, S. P., Nichol, R. C., Baldry, I. K., et al. 2009, MNRAS, 393, 1324

Banerji, M., Abdalla, F. B., Lahav, O., & Lin, H. 2008, MNRAS, 386, 1219

Behroozi, P. S., Wechsler, R. H., & Wu, H.-Y. 2011, ArXiv e-prints, arXiv:1110.4372 [astro-ph.CO]

Bellagamba, F., Maturi, M., Hamana, T., et al. 2011, MNRAS, 217

Berlind, A. A., Frieman, J., Weinberg, D. H., et al. 2006, ApJS, 167, 1

Blanton, M. R., & Berlind, A. A. 2007, ApJ, 664, 791

Blanton, M. R., Eisenstein, D., Hogg, D. W., Schlegel, D. J., & Brinkmann, J. 2005, ApJ, 629, 143

Blanton, M. R., & Moustakas, J. 2009, ARA&A, 47, 159

Boselli, A., Boissier, S., Cortese, L., et al. 2006, ApJ, 651, 811

Boselli, A., & Gavazzi, G. 2006, PASP, 118, 517

Bradač, M., Allen, S. W., Treu, T., et al. 2008, ApJ, 687, 959

Bruce, V. A., Dunlop, J. S., Cirasuolo, M., et al. 2012, ArXiv e-prints, arXiv:1206.4322 [astro-ph.CO]

Brunner, R. J., & Lubin, L. M. 2000, AJ, 120, 2851

Bruzual, G., & Charlot, S. 2003, MNRAS, 344, 1000

Bundy, K., Ellis, R. S., Conselice, C. J., et al. 2006, ApJ, 651, 120

Bundy, K., Scarlata, C., Carollo, C. M., et al. 2010, ApJ, 719, 1969

Burstein, D., Ho, L. C., Huchra, J. P., & Macri, L. M. 2005, ApJ, 621, 246

Butcher, H., & Oemler, A. 1984, ApJ, 285, 426

Capak, P., Abraham, R. G., Ellis, R. S., et al. 2007a, ApJS, 172, 284

Capak, P., Aussel, H., Ajiki, M., et al. 2007b, ApJS, 172, 99

Capak, P. L., Scoville, N. Z., Sanders, D. B., et al. 2010, in Bulletin of the American Astronomical Society, Vol. 42, American Astronomical Society Meeting Abstracts 215,

410.05
Cappelluti, N., Brusa, M., Hasinger, G., et al. 2009, A&A, 497, 635
Carlberg, R. G., Yee, H. K. C., Morris, S. L., et al. 2001, ApJ, 552, 427
Cassata, P., Cimatti, A., Franceschini, A., et al. 2005, MNRAS, 357, 903
Chabrier, G. 2003, PASP, 115, 763
Chary, R., & Elbaz, D. 2001, ApJ, 556, 562
Christlein, D., & Zabludoff, A. I. 2004, ApJ, 616, 192
—. 2005, ApJ, 621, 201
Cibinel, A., Carollo, C. M., Lilly, S. J., et al. 2012, ArXiv e-prints, arXiv:1206.6496 [astro-ph.CO]
Clowe, D., Bradač, M., Gonzalez, A. H., et al. 2006, ApJ, 648, L109
Clowe, D., Gonzalez, A., & Markevitch, M. 2004, ApJ, 604, 596
Cohn, J. D., & White, M. 2005, Astroparticle Physics, 24, 316
—. 2009, MNRAS, 393, 393
Coil, A. L., Blanton, M. R., Burles, S. M., et al. 2010, ArXiv e-prints, arXiv:1011.4307 [astro-ph.CO]
Cooper, M. C., Newman, J. A., Croton, D. J., et al. 2006, MNRAS, 370, 198
Cooper, M. C., Newman, J. A., Coil, A. L., et al. 2007, MNRAS, 376, 1445
Cooper, M. C., Coil, A. L., Gerke, B. F., et al. 2010, MNRAS, 409, 337
Cooray, A., & Sheth, R. 2002, Phys. Rep., 372, 1
Cortese, L., Marcillac, D., Richard, J., et al. 2007, MNRAS, 376, 157
Cross, N. J. G., Bouwens, R. J., Benítez, N., et al. 2004, AJ, 128, 1990
Csabai, I., Budavári, T., Connolly, A. J., et al. 2003, AJ, 125, 580
Cucciati, O., Iovino, A., Marinoni, C., et al. 2006, A&A, 458, 39
Cucciati, O., Iovino, A., Kovač, K., et al. 2010, A&A, 524, A2
Dale, D. A., & Helou, G. 2002, ApJ, 576, 159
Das, S., Marriage, T. A., Ade, P. A. R., et al. 2011, ApJ, 729, 62
Davis, M., Efstathiou, G., Frenk, C. S., & White, S. D. M. 1985, ApJ, 292, 371
De Propris, R., Colless, M., Peacock, J. A., et al. 2004, MNRAS, 351, 125
Dietrich, J. P., Böhnert, A., Lombardi, M., Hilbert, S., & Hartlap, J. 2012, MNRAS, 419, 3547
Dressler, A. 1980, ApJ, 236, 351
Dressler, A., Oemler, Jr., A., Couch, W. J., et al. 1997, ApJ, 490, 577
Driver, S. P., Norberg, P., Baldry, I. K., et al. 2009, Astronomy and Geophysics, 50, 12
Drory, N., Bundy, K., Leauthaud, a., et al. 2009, ApJ, 707, 1595
Dunkley, J., Komatsu, E., Nolta, M. R., et al. 2009, ApJS, 180, 306
Dunkley, J., Hlozek, R., Sievers, J., et al. 2010, ArXiv e-prints, arXiv:1009.0866 [astro-ph.CO]
Eke, V. R., Baugh, C. M., Cole, S., et al. 2004, MNRAS, 348, 866
Elbaz, D., Dickinson, M., Hwang, H. S., et al. 2011, A&A, 533, A119
Elvis, M., Civano, F., Vignali, C., et al. 2009, ApJS, 184, 158
Evrard, A. E., Bialek, J., Busha, M., et al. 2008, ApJ, 672, 122
Fakhouri, O., Ma, C.-P., & Boylan-Kolchin, M. 2010, MNRAS, 406, 2267

Feruglio, C., Aussel, H., Le Floc'h, E., et al. 2010, ApJ, 721, 607
Finoguenov, A., Guzzo, L., Hasinger, G., et al. 2007, ApJS, 172, 182
Finoguenov, A., Connelly, J. L., Parker, L. C., et al. 2009, ApJ, 704, 564
Finoguenov, A., Watson, M. G., Tanaka, M., et al. 2010, MNRAS, 403, 2063
Ford, J., Hildebrandt, H., Van Waerbeke, L., et al. 2012, ApJ, 754, 143
Forman, W., & Jones, C. 1982, ARA&A, 20, 547
Fowler, J. W., Acquaviva, V., Ade, P. A. R., et al. 2010, ApJ, 722, 1148
Gavazzi, G., Boselli, A., Mayer, L., et al. 2001, ApJ, 563, L23
George, M. R., Ma, C.-P., Bundy, K., et al. 2013, ApJ, 770, 113
George, M. R., Leauthaud, A., Bundy, K., et al. 2011, ApJ, 742, 125
—. 2012, ApJ, 757, 2
Gerke, B. F., Newman, J. A., Davis, M., et al. 2005, ApJ, 625, 6
Gerke, B. F., Newman, J. a., Faber, S. M., et al. 2007, MNRAS, 376, 1425
Gillis, B. R., & Hudson, M. J. 2011, MNRAS, 410, 13
Giodini, S., Pierini, D., Finoguenov, A., et al. 2009, ApJ, 703, 982
Gladders, M. D., & Yee, H. K. C. 2000, AJ, 120, 2148
Gladders, M. D., & Yee, H. K. C. 2005, ApJS, 157, 1
Goto, T., Okamura, S., Sekiguchi, M., et al. 2003, PASJ, 55, 757
Grogin, N. A., Kocevski, D. D., Faber, S. M., et al. 2011, ApJS, 197, 35
Grove, L. F., Benoist, C., & Martel, F. 2009, A&A, 494, 845
Guzik, J., & Seljak, U. 2002, MNRAS, 335, 311
Haas, M. R., Schaye, J., & Jeeson-Daniel, A. 2011, ArXiv e-prints, arXiv:1103.0547 [astro-ph.CO]
Hall, N. R., Keisler, R., Knox, L., et al. 2010, ApJ, 718, 632
Hansen, S. M., McKay, T. A., Wechsler, R. H., et al. 2005, ApJ, 633, 122
Hansen, S. M., Sheldon, E. S., Wechsler, R. H., & Koester, B. P. 2009, ApJ, 699, 1333
Hao, J., McKay, T. A., Koester, B. P., et al. 2010, ApJS, 191, 254
Hasinger, G., Cappelluti, N., Brunner, H., et al. 2007, ApJS, 172, 29
Hikage, C., Takada, M., & Spergel, D. N. 2012, MNRAS, 419, 3457
Hilbert, S., & White, S. D. M. 2010, MNRAS, 404, 486
Hilton, M., Lloyd-Davies, E., Stanford, S. A., et al. 2010, ApJ, 718, 133
Hoaglin, D. C., Mosteller, F., & Tukey, J. W. 1983, Understanding robust and exploratory data anlysis, ed. Hoaglin, D. C., Mosteller, F., & Tukey, J. W.
Hudson, M. J., Gwyn, S. D. J., Dahle, H., & Kaiser, N. 1998, ApJ, 503, 531
Ilbert, O., Capak, P., Salvato, M., et al. 2009, ApJ, 690, 1236
Ilbert, O., Salvato, M., Le Floc'h, E., et al. 2010, ApJ, 709, 644
Iovino, A., Cucciati, O., Scodeggio, M., et al. 2010, A&A, 509, A40
Jee, M. J., Dawson, K. S., Hoekstra, H., et al. 2011, ApJ, 737, 59
Johnston, D. E., Sheldon, E. S., Tasitsiomi, A., et al. 2007a, ApJ, 656, 27
Johnston, D. E., Sheldon, E. S., Wechsler, R. H., et al. 2007b, ArXiv e-prints, arXiv:0709.1159
—. 2007c, ArXiv e-prints, arXiv:0709.1159
Katayama, H., Hayashida, K., Takahara, F., & Fujita, Y. 2003, ApJ, 585, 687

Kauffmann, G., White, S. D. M., Heckman, T. M., et al. 2004, MNRAS, 353, 713
Kaviraj, S., Schawinski, K., Devriendt, J. E. G., et al. 2007, ApJS, 173, 619
Kaviraj, S., Khochfar, S., Schawinski, K., et al. 2008, MNRAS, 388, 67
Kenney, J. D. P., Rubin, V. C., Planesas, P., & Young, J. S. 1995, ApJ, 438, 135
Knobel, C., Lilly, S. J., Iovino, a., et al. 2009, ApJ, 697, 1842
Knobel, C., Lilly, S. J., Kovac, K., et al. 2012, ArXiv e-prints, arXiv:1211.5607 [astro-ph.CO]
Koekemoer, A. M., Aussel, H., Calzetti, D., et al. 2007, ApJS, 172, 196
Koekemoer, A. M., Faber, S. M., Ferguson, H. C., et al. 2011, ApJS, 197, 36
Koester, B. P., McKay, T. A., Annis, J., et al. 2007a, ApJ, 660, 239
—. 2007b, ApJ, 660, 221
Komatsu, E., & Seljak, U. 2002, MNRAS, 336, 1256
Kovač, K., Lilly, S. J., Knobel, C., et al. 2010, ApJ, 718, 86
Kovač, K., Lilly, S. J., Cucciati, O., et al. 2010, ApJ, 708, 505
Lackner, C. N., & Gunn, J. E. 2012, MNRAS, 421, 2277
—. 2013, MNRAS, 428, 2141
Lagache, G., Dole, H., & Puget, J.-L. 2003, MNRAS, 338, 555
Le Floc'h, E., Aussel, H., Ilbert, O., et al. 2009, ApJ, 703, 222
Leauthaud, A., Tinker, J., Behroozi, P. S., Busha, M. T., & Wechsler, R. 2011a, arxiv:1103.2077
Leauthaud, A., Massey, R., Kneib, J.-P., et al. 2007, ApJS, 172, 219
Leauthaud, A., Finoguenov, A., Kneib, J.-P., et al. 2010, ApJ, 709, 97
Leauthaud, A., Tinker, J., Bundy, K., et al. 2011b, arxiv:1104.0928
Leauthaud, A., Tinker, J., Bundy, K., et al. 2012a, ApJ, 744, 159
Leauthaud, A., George, M. R., Behroozi, P. S., et al. 2012b, ApJ, 746, 95
Lee, N., Le Floc'h, E., Sanders, D. B., et al. 2010, ApJ, 717, 175
Lewis, I., Balogh, M., De Propris, R., et al. 2002, MNRAS, 334, 673
Lilly, S. J., Le Fèvre, O., Renzini, A., et al. 2007, ApJS, 172, 70
Lilly, S. J., Le Brun, V., Maier, C., et al. 2009, ApJS, 184, 218
Lin, Y.-T., & Mohr, J. J. 2004, ApJ, 617, 879
Lin, Y.-T., Mohr, J. J., & Stanford, S. A. 2004, ApJ, 610, 745
Lotz, J. M., Primack, J., & Madau, P. 2004, AJ, 128, 163
Lueker, M., Reichardt, C. L., Schaffer, K. K., et al. 2010, ApJ, 719, 1045
Macciò, A. V., Dutton, A. A., van den Bosch, F. C., et al. 2007, MNRAS, 378, 55
Majumdar, S., & Mohr, J. J. 2004, ApJ, 613, 41
Mandelbaum, R., Seljak, U., Baldauf, T., & Smith, R. E. 2010, MNRAS, 405, 2078
Mandelbaum, R., Seljak, U., Cool, R. J., et al. 2006a, MNRAS, 372, 758
Mandelbaum, R., Seljak, U., & Hirata, C. M. 2008, J. Cosmology Astropart. Phys., 8, 6
Mandelbaum, R., Seljak, U., Kauffmann, G., Hirata, C. M., & Brinkmann, J. 2006b, MNRAS, 368, 715
Marinoni, C., Davis, M., Newman, J. A., & Coil, A. L. 2002, ApJ, 580, 122
Martig, M., Bournaud, F., Teyssier, R., & Dekel, A. 2009, ApJ, 707, 250
Massey, R., Kitching, T., & Nagai, D. 2011, MNRAS, 413, 1709

Massey, R., Stoughton, C., Leauthaud, A., et al. 2010, MNRAS, 401, 371
Masters, K. L., Mosleh, M., Romer, A. K., et al. 2010, MNRAS, 405, 783
McCracken, H. J., Capak, P., Salvato, M., et al. 2010, ApJ, 708, 202
McGee, S. L., Balogh, M. L., Wilman, D. J., et al. 2011, MNRAS, 413, 996
Mei, S., Holden, B. P., Blakeslee, J. P., et al. 2009, ApJ, 690, 42
Milkeraitis, M., van Waerbeke, L., Heymans, C., et al. 2010, MNRAS, 406, 673
Miller, C. J., Nichol, R. C., Reichart, D., et al. 2005, AJ, 130, 968
Miralda-Escude, J. 1991, ApJ, 370, 1
Moran, S. M., Ellis, R. S., Treu, T., et al. 2007, ApJ, 671, 1503
More, S., van den Bosch, F. C., Cacciato, M., et al. 2009, MNRAS, 392, 801
Mulchaey, J. S., Davis, D. S., Mushotzky, R. F., & Burstein, D. 2003, ApJS, 145, 39
Mulchaey, J. S., & Zabludoff, A. I. 1998, ApJ, 496, 73
Muzzin, A., Wilson, G., Yee, H. K. C., et al. 2012, ApJ, 746, 188
Natarajan, P., De Lucia, G., & Springel, V. 2007, MNRAS, 376, 180
Natarajan, P., & Kneib, J.-P. 1997, MNRAS, 287, 833
Natarajan, P., Kneib, J.-P., Smail, I., et al. 2009, ApJ, 693, 970
Navarro, J. F., Frenk, C. S., & White, S. D. M. 1996, ApJ, 462, 563
Neto, A. F., Gao, L., Bett, P., et al. 2007, MNRAS, 381, 1450
Oemler, A. 1974, ApJ, 194, 1
Oesch, P. A., Carollo, C. M., Feldmann, R., et al. 2010, ApJ, 714, L47
Oguri, M., Takada, M., Okabe, N., & Smith, G. P. 2010, MNRAS, 405, 2215
Olsen, L. F., Benoist, C., Cappi, A., et al. 2007, A&A, 461, 81
Osmond, J. P. F., & Ponman, T. J. 2004, MNRAS, 350, 1511
Pastor Mira, E., Hilbert, S., Hartlap, J., & Schneider, P. 2011, A&A, 531, A169
Peng, Y.-j., Lilly, S. J., Renzini, A., & Carollo, M. 2012, ApJ, 757, 4
Peng, Y.-j., Lilly, S. J., Kovač, K., et al. 2010, ApJ, 721, 193
Poggianti, B. M., Smail, I., Dressler, A., et al. 1999, ApJ, 518, 576
Poggianti, B. M., Desai, V., Finn, R., et al. 2008, ApJ, 684, 888
Poole, G. B., Fardal, M. A., Babul, A., et al. 2006, MNRAS, 373, 881
Postman, M., Lubin, L., Gunn, J., et al. 1996, AJ, 111, 615
Postman, M., Franx, M., Cross, N. J. G., et al. 2005, ApJ, 623, 721
Power, C., Knebe, A., & Knollmann, S. R. 2012, MNRAS, 419, 1576
Prescott, M. K. M., Impey, C. D., Cool, R. J., & Scoville, N. Z. 2006, ApJ, 644, 100
Presotto, V., Iovino, A., Scodeggio, M., et al. 2012, A&A, 539, A55
Reddick, R. M., Wechsler, R. H., Tinker, J. L., & Behroozi, P. S. 2012, ArXiv e-prints, arXiv:1207.2160 [astro-ph.CO]
Rhodes, J., Refregier, A., & Groth, E. J. 2000, ApJ, 536, 79
Rhodes, J. D., Massey, R. J., Albert, J., et al. 2007, ApJS, 172, 203
Robotham, A. S. G., Norberg, P., Driver, S. P., et al. 2011, MNRAS, 416, 2640
Rozo, E., Rykoff, E., Koester, B., et al. 2011, ApJ, 740, 53
Rykoff, E. S., Koester, B. P., Rozo, E., et al. 2011, ArXiv e-prints, arXiv:1104.2089 [astro-ph.CO]

Salvato, M., Hasinger, G., Ilbert, O., et al. 2009, ApJ, 690, 1250
Sanders, D. B., Salvato, M., Aussel, H., et al. 2007, ApJS, 172, 86
Sanderson, A. J. R., Edge, A. C., & Smith, G. P. 2009, MNRAS, 398, 1698
Scarlata, C., Carollo, C. M., Lilly, S., et al. 2007, ApJS, 172, 406
Schawinski, K., Lintott, C., Thomas, D., et al. 2009, MNRAS, 396, 818
Schmidt, F., Leauthaud, A., Massey, R., et al. 2012, ApJ, 744, L22
Scodeggio, M., Vergani, D., Cucciati, O., et al. 2009, A&A, 501, 21
Scoville, N., Aussel, H., Benson, a., et al. 2007, ApJS, 172, 150
Scoville, N., Aussel, H., Brusa, M., et al. 2007, ApJS, 172, 1
Shan, H., Qin, B., Fort, B., et al. 2010, MNRAS, 406, 1134
Shaw, L. D., Nagai, D., Bhattacharya, S., & Lau, E. T. 2010, ApJ, 725, 1452
Sheldon, E. S., Annis, J., Böhringer, H., et al. 2001, ApJ, 554, 881
Shirokoff, E., Reichardt, C. L., Shaw, L., et al. 2010, ArXiv e-prints, arXiv:1012.4788 [astro-ph.CO]
Siebenmorgen, R., & Krügel, E. 2007, A&A, 461, 445
Simionescu, A., Allen, S. W., Mantz, A., et al. 2011, Science, 331, 1576
Skibba, R. A., & Macciò, A. V. 2011, MNRAS, 416, 2388
Skibba, R. A., van den Bosch, F. C., Yang, X., et al. 2011, MNRAS, 410, 417
Skibba, R. A., Bamford, S. P., Nichol, R. C., et al. 2009, MNRAS, 399, 966
Skibba, R. A., Masters, K. L., Nichol, R. C., et al. 2012, MNRAS, 423, 1485
Smith, G. P., Kneib, J.-P., Smail, I., et al. 2005a, MNRAS, 359, 417
Smith, G. P., Treu, T., Ellis, R. S., Moran, S. M., & Dressler, A. 2005b, ApJ, 620, 78
Smith, R. J., Lucey, J. R., & Carter, D. 2012, MNRAS, 421, 2982
Sun, M., Sehgal, N., Voit, G. M., et al. 2011, ApJ, 727, L49
Sun, M., Voit, G. M., Donahue, M., et al. 2009, ApJ, 693, 1142
Sunyaev, R. A., & Zeldovich, Y. B. 1972, Comments on Astrophysics and Space Physics, 4, 173
Tanaka, M., Finoguenov, A., & Ueda, Y. 2010, ApJ, 716, L152
Tanaka, M., Kodama, T., Arimoto, N., et al. 2005, MNRAS, 362, 268
Tasca, L. A. M., Kneib, J.-P., Iovino, A., et al. 2009, A&A, 503, 379
Taylor, J. E., Massey, R. J., Leauthaud, A., et al. 2012, ApJ, 749, 127
Tinker, J., Kravtsov, A. V., Klypin, A., et al. 2008, ApJ, 688, 709
Tinker, J. L., George, M. R., Leauthaud, A., et al. 2012, ApJ, 755, L5
Trac, H., Bode, P., & Ostriker, J. P. 2011, ApJ, 727, 94
Tran, K.-V. H., Simard, L., Zabludoff, A. I., & Mulchaey, J. S. 2001, ApJ, 549, 172
Tran, K.-V. H., Papovich, C., Saintonge, A., et al. 2010, ApJ, 719, L126
van den Bosch, F. C., Aquino, D., Yang, X., et al. 2008, MNRAS, 387, 79
van der Wel, A., Holden, B. P., Franx, M., et al. 2007, ApJ, 670, 206
van Dokkum, P. G., & Conroy, C. 2010, Nature, 468, 940
Vikhlinin, A., McNamara, B. R., Forman, W., et al. 1998, ApJ, 502, 558
Weinmann, S. M., Kauffmann, G., van den Bosch, F. C., et al. 2009, MNRAS, 394, 1213
Weinmann, S. M., van den Bosch, F. C., Yang, X., & Mo, H. J. 2006, MNRAS, 366, 2

Wetzel, A. R., Tinker, J. L., & Conroy, C. 2012a, MNRAS, 424, 232
Wetzel, A. R., Tinker, J. L., Conroy, C., & van den Bosch, F. C. 2012b, ArXiv e-prints, arXiv:1206.3571 [astro-ph.CO]
White, R. A., Bliton, M., Bhavsar, S. P., et al. 1999, AJ, 118, 2014
Wilman, D. J., Oemler, Jr., A., Mulchaey, J. S., et al. 2009, ApJ, 692, 298
Wojtak, R., Hansen, S. H., & Hjorth, J. 2011, Nature, 477, 567
Woo, J., Dekel, A., Faber, S. M., et al. 2012, ArXiv e-prints, arXiv:1203.1625 [astro-ph.CO]
Wright, C. O., & Brainerd, T. G. 2000, ApJ, 534, 34
Yang, X., Mo, H. J., & van den Bosch, F. C. 2009, ApJ, 695, 900
Yang, X., Mo, H. J., van Den Bosch, F. C., & Jing, Y. P. 2005, MNRAS, 356, 1293
Yang, X., Mo, H. J., van den Bosch, F. C., et al. 2006, MNRAS, 373, 1159
Yang, X. H., Mo, H. J., Kauffmann, G., & Chu, Y. Q. 2003, MNRAS, 339, 387
Yip, C., Szalay, A. S., Carliles, S., & Budavári, T. 2011, ApJ, 730, 54
Zabludoff, A. I., & Mulchaey, J. S. 1998, ApJ, 496, 39
Zehavi, I., Zheng, Z., Weinberg, D. H., et al. 2005, ApJ, 630, 1
Zhao, D. H., Jing, Y. P., Mo, H. J., & Börner, G. 2009, ApJ, 707, 354